

Developing an a-/nc-Ge:H

film characterization and single-junction solar cell

by

Ashwath Narayan Ravichandran

in partial fulfillment of the requirements for the degree of

Master of Science

in Electrical Power Engineering

at the Delft University of Technology, to be defended publicly on Thursday May 28, 2020 at 14:00.

Student number: 4731735

Thesis committee: Prof. dr. A. H. M. Smets, TU Delft, ESE - PVMD, Supervisor

Dr. O. Isabella, TU Delft, ESE - PVMD, Professor

Dr. ir. M. Ghaffarian Niasar, TU Delft, ESE - DCES, Assistant Professor Ir. T. de Vrijer, TU Delft, ESE - PVMD, Daily Supervisor

An electronic version of this thesis is available at http://repository.tudelft.nl/.







Acknowledgements

This Master's thesis work concludes my time as a student of Electrical Power Engineering at Delft University of Technology. The last 2 and a half years have brought about many new experiences and I have also been able to gain a lot of knowledge from them. I am pretty sure that this journey that I have gone through would serve me well in tackling and solving new challenges that may arise as I enter into the industry of sustainable energy technology.

I would like to express my sincere gratitude to Prof. dr. Arno Smets for the constant guidance and help he provided throughout the duration of my thesis. His passion, enthusiasm along with his expertise in this field are very much inspiring for students like me who also want to venture into the same field in the future.

I would also like to express my regards to my daily supervisor Ir. Thierry de Vrijer, without whom it would not have been possible for me to complete this thesis on time. Apart from his excellent supervision, I would specifically thank him for all the prompt help he provided, whether it was for a quick chat to explain a specific concept or demonstrating the usage of various equipment or anything in general with regards to the thesis. I would also like to thank Dr. Olindo Isabella and Dr. ir. Mohamad Ghaffarian Niasar for their willingness to spare their time so as to be able to participate as members of my masters thesis committee.

My gratitude to the technicians and process engineers, Martijn Thijssen and Remko Koornneef, who were of great help to me while using the various equipment and were also available whenever any assistance was needed.

I cannot forget to mention my friend Bilal Bouazzata, with whom I shared my entire clean room experience. He was another student who was working on this broad thesis project and was my go-to man throughout the thesis. It would have definitely been much more stressful for me if not for his support.

I would like to specifically thank my friend Ashish Binani, for always being there for me ever since I got to know him during the introduction program. He has seen my highs and lows through the last 2 and a half years and helped me get through the tough times through great moral support. I cannot forget to mention my friend Gettsy Prathiba, who helped me get through the challenge of settling into a new place far away from home during the initial days of masters. Additionally, I would like to thank the members of "Valterri, it's James" for all the great memories we shared during the weekends.

Last but not least I would like to thank my family. I cannot express through words how much they mean to me. Without their constant love and support, none of this would have been possible. I shall always try my best to make you all proud.

Ashwath Narayan Ravichandran Delft, May 2020

Abstract

Single junction solar cells have a theoretical efficiency limit of 33.1% due to spectral mismatch. To overcome this, multi-junction devices are generally fabricated with two or more junctions, so as to achieve better energy conversion efficiency by optimum spectral utilization. The c-Si bottom cell of a thin-film Si triple-/quadruple-junction device does not utilize the low energy photons (below 1.1 eV). The photons in the range of 0.7-1.1 eV, have an available current density of 15.9 mA/cm². A fraction of this current density would be large enough to not limit the output current of these thin-film Si-based multi-junction devices. Ge, belonging to the same group IV as Si and being heavier than it, forms weaker covalent bonds. Hence, it has a lower bandgap energy, making it the preferred choice of material. In this work, a low bandgap material such as a Ge-based absorber layer is fabricated that can be used in the bottom cell of a thin-film Si-based quadruple-junction device.

This thesis will focus on the influence of a set of deposition parameters on the various properties of the Ge:H films. This will result in a set of Ge:H films from which a specific few are used as absorber layers to analyze the performance of a single-junction cell. The fabrication of the Ge:H films is carried out on a CASCADE setup which is based on the RF-PECVD technique.

A processing range is identified to be in the range of 1-5 mbar pressure with RF powers ranging between 5-25 W for a fixed electrode distance of 20mm. nc-Ge:H are processed in the range of 20-25 W for pressures of 2 mbar and higher at a high dilution of 400. A strong correlation is found between the refractive index of the films and the presence of GeO_x . The films with low refractive index possibly indicate a porous network with high void density show substantial oxygen contamination and vice-versa. Water vapour in the ambient is responsible for the oxidation. The oxygen contamination significantly impacts the properties of the films. The E_{04} optical bandgap increases with oxygen contamination which hinders the development of a low-bandgap absorber layer, while the E_{act} decreases to values as low as around 50 eV . Generally, the pre-exponential factor (σ_o) decreases significantly by 1-5 orders of magnitude which outweighs the decrease in E_{act} , resulting in the decrease in dark conductivity by 1-3 orders of magnitude. Consequently, highest photo/dark conductivity ratios of 5-6 are obtained for these films. Amongst the films without oxygen contamination, the lowest E_{04} optical bandgap reported is 1.2 eV, with a E_{TAUC} bandgap of 0.93 and a photo/dark conductivity ratio around 3.4.

Most of the single-junction cells processed at absorber layer thicknesses of 100nm and above show resistor-like behaviour. The substantially high values of R_s & losses associated to the R_{sh} degrade the cell parameters significantly. Although, for low absorber layer thickness of around 50nm, the closest resemblance to a cell-behaviour is observed. Therefore, there is a scope for improvement with regards to processing of these single-junction cells.

Contents

Abstract	V
Nomenclature	ix
List of Figures	xiii
List of Tables	хv
1 Introduction 1.1 General Introduction. 1.2 Working Principle of a solar cell. 1.3 History of solar cells. 1.3.1 Wafer-based cell technology 1.3.2 Thin-film cell technology 1.3.3 Multi-Junction Devices 1.4 Motivation behind multi-junction device 1.5 Goal and Outline of the Thesis.	3 6 6 6 7
Theoretical Background 2.1 Optical Properties 2.1.1 Optical Reflection and Optical Transmission 2.1.2 Optical Absorption 2.2 Electrical Properties 2.2.1 Conductivity 2.2.2 Activation Energy 2.3 Material Properties 2.3.1 Basic lattice structure 2.3.2 Crystallinity 2.3.3 Defects 2.3.4 Bandgap	9 11 11 12 12 12 13 13
3 Experimental Methodology 3.1 Overview of Process 3.2 Preparation of Sample 3.3 Fabrication techniques 3.3.1 Plasma Enhanced Chemical Vapour Deposition 3.3.2 RF Magnetron Sputtering 3.3.3 Metal Evaporation 3.3.4 Annealing step 3.4 Characterization techniques 3.4.1 Dark Conductivity and Activation Energy 3.4.2 Spectroscopy Ellipsometry 3.4.3 Raman Spectroscopy 3.4.4 Fourier Transform Infrared Spectroscopy 3.4.5 Photo-thermal Deflection Spectroscopy 3.4.6 J-V characteristics	16 17 18 18 19 19 20 21 21 22
4 Processing Range for Successful Film Deposition 4.1 Initial choice of deposition parameters 4.2 Assessment of the type of deposition 4.3 Properties of the successfully deposited films	

viii Contents

5	Characterization of a-/nc-Ge:H films 5.1 Effect of varying F(H ₂)/F(GeH ₄) dilution ratio	. 35 . 40
	and Analysis	
6	Single Junction Solar Cell 6.1 p-n configuration cells	
7	Conclusions and Recommendations	55
Bi	bliography	57
A	Appendix A - Additional Results of film characteristics A.1 Effect of varying H ₂ /GeH ₄ dilution ratio	
	A.3 Effect of varying Deposition Temperature	

Nomenclature

General Abbreviations

CO₂ Carbon Dioxide

GHG Green House Gas

PV Photovoltaic

AMO Air Mass 0

AM1.5 Air Mass 1.5

STC Standard Test Conditions

EM Electromagnetic

SQ Shockley-Queisser

Ar Argon

Si Silicon

Ge Germanium

H Hydrogen

Al Aluminium

Cr Chromium

Ag Silver

c-Si Crystalline Silicon

nc-Si Nano-crystalline Silicon

a-Si:H Hydrogenated Amorphous Silicon

a-SiGe:H Hydrogenated Amorphous Silicon Germanium

a-Ge:H Hydrogenated Amorphous Germanium

nc-Ge:H Hydrogenated Nano-crystalline Germanium

a-Ge Amorphous Germanium

nc-Ge Nano-crystalline Germanium

c-Ge Crystalline Germanium

TCO Transparent Conductive Oxide

ITO Indium-doped Tin Oxide

IPA Isopropanol

RF Radio Frequency

RF-PECVD Radio Frequency- Plasma Enhanced Chemical Vapour Deposition

x Contents

- **PECVD** Plasma Enhanced Chemical Vapour Deposition
- **ETP-CVD** Expanding Thermal Plasma Chemical Vapour Deposition
- FTIR Fourier Transform Infrared Spectroscopy
- **SE** Spectroscopy Ellipsometry

Latin Letters

- **A** Absorptance
- I Current
- **I**_e Irradiance
- J Current Density
- k Extinction Coefficient
- n Refractive Index (real part)
- **R** Reflectance
- **T** Temperature
- T Transmittance
- **V** Voltage

Greek Letters

- α Absorption coefficient
- Δ Phase difference
- κ Refractive Index (imaginary part)
- λ Wavelength
- ν Frequency
- Ψ Amplitude ratio
- ρ Charge Density / Complex Reflectance ratio
- σ Conductivity

Subscripts

- c Conduction band
- **F** Fermi level
- **g** Bandgap
- **oc** Open-circuit
- ph Photon
- **s** Series

Contents xi

- **sc** Short-circuit
- **sh** Shunt
- v Valence band

Constants

- **c** Speed of light in vacuum (3*10⁸ m/s)
- **F** Faraday Constant
- h Plank's Constant
- \mathbf{k}_b Boltzmann Constant
- μ_o Vacuum Permeability
- **q** Elementary Charge (1.602*10⁻¹⁹ C)

List of Figures

	The Worldwide energy consumption from 1990 to 2018 [1] Global energy-related carbon dioxide emissions by source in Giga-tonnes [2] Contribution of various sources towards generation of electricity [3] Contribution of various renewable sources towards generation of electricity [3] The Spectrum of solar radiation [4] Energy band diagram of a semiconductor material [5] Schematic diagram of the working of a solar cell Representation of (a) non-absorption loss and (b) thermalization loss [5] Shockley-Queisser limit of a single-junction solar cell with various primary losses [5] (a) Direct bandgap semiconductor; (b) Indirect bandgap semiconductor [5]	1 2 3 3 4 5 5 6
1.11	Basic structure of a thin film quadruple junction solar cell	7
2.12.22.3	Behaviour of incident light a the interface off two different mediums [5] Transverse vs lateral conductivity in a cell [6] Variation in crystalline fraction with respect to deposition parameters [5]	9 12 13
3.1 3.2 3.3 3.4 3.5 3.6 3.7 3.8 3.9	A p-i-n superstrate configuration [7] Stages involved in the fabrication of Ge:H layers (left) & the corresponding solar cell (right) Schematic diagram of a RF-PECVD system [8] The CASCADE system (PVMD Group) Schematic representation of RF magnetron sputtering system (PVMD Group) [7] Schematic representation of the metal evaporation chamber [7] The schematic depiction of an ellipsometry setup [9] Schematic representation of the PDS setup (PVMD Group) [10] Schematic representation of an ideal J-V curve for a solar cell [11]	15 16 17 18 18 19 20 23 23
4.1 4.2	Type of deposition obtained for various pressure-power combinations Deposition rate & Electrical parameters for various pressure-power combinations	26 27
5.1 5.2	Fitted FTIR Spectrum for films with varying $F(H_2)/F(GeH_4)$ dilution ratio	30 31
5.9	Effect of varying $F(H_2)/F(GeH_4)$ dilution ratio on the Activation Energy (E_{act}) , Dark Conductivity & the Photo/Dark conductivity ratio	33 33 34 34 36 36
5.11 5.12 5.13 5.14 5.15	Effect of varying pressure-power on the Activation Energy (E_{act}), Dark Conductivity & the Photo/Dark Conductivity ratio Raman Spectrum for 5 W and 10 W films at different pressures Raman Spectrum at 15 W, 20 W & 25 W films at different pressures Crystalline Fraction (X_c) vs Pressure-Power Effect of varying Deposition Temperature on the α_{GeO_x} & the hydrogen concentration (C_H) Effect of varying Deposition Temperature on the n @ 600nm & the E_{04} optical bandgap Effect of varying Deposition Temperature on the Activation Energy (E_{act}), Dark conductivity & the Photo/Dark Conductivity ratio	37 38 39 39 41 41

xiv List of Figures

5.18 5.19 5.20 5.21 5.22 5.23	Crystalline Fraction (X_c) vs Deposition Temperature	43 45 45 46 47 48
6.2	Series and Shunt resistances as a function of n-layer thickness for Film A (top); Film B	52 52 53
A.2 A.3 A.4 A.5 A.6 A.7	Deposition rate vs H ₂ /GeH ₄ dilution ratio Fitted FTIR Spectrum for films with varying pressure-power E ₀₃ optical bandgap vs Pressure-Power Deposition rate vs Pressure-Power Fitted FTIR Spectrum for film with varying Deposition Temperature E ₀₃ optical bandgap vs Deposition Temperature	61 62 63 63 64 64 65

List of Tables

	Raman stretching mode peaks to their corresponding wavenumber for a-/nc-Ge:H FTIR peaks to their corresponding wavenumber for a-/nc-Ge:H	
4.1	Initial deposition parameters for obtaining Ge:H films	25
5.25.35.4	Deposition parameters for varying $F(H_2)/F(GeH_4)$ dilution ratio Deposition parameters for varying pressure-power Deposition parameters for varying deposition temperature Deposition and HPT parameters	35 40 44
6.1	Deposition and HPT parameters for the n-layer	51

Introduction

1.1. General Introduction

In recent years, there has been a substantial increment in the consumption of electrical energy to satisfy the basic needs and necessities of mankind. Figure 1.1 depicts the rate at which electrical energy consumption has been increasing over the past few decades. It can also be observed that the region of Asia accounted for almost 80% of this increase in electrical energy consumption mainly due to its economic growth and rapid industrial expansion. Therefore, it is quite obvious that in order to meet this growing demand, there is a need to generate sufficient electrical energy.

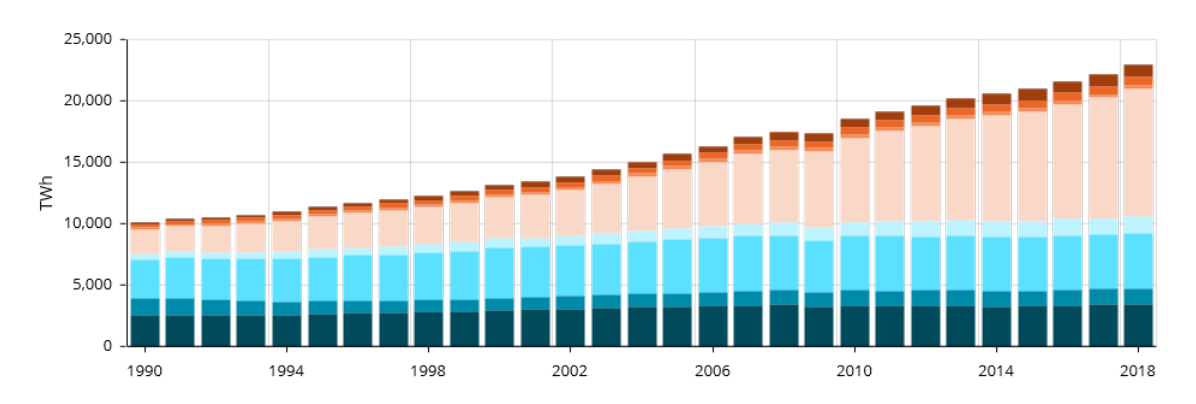


Figure 1.1: The Worldwide energy consumption from 1990 to 2018 [1]

Currently, the electrical energy demand is largely being fulfilled by utilization of conventional non-renewable energy sources such as Oil, Coal, Natural Gas, etc. to name a few. However, there is an over-exploitation of these conventional fossil fuels currently, which could lead to the depletion of its reserves in the near future [12]. Based on wide-spread studies regarding the depletion rate of these fossil fuels, Oil and Natural gas are expected to last only until the year 2042 and Coal until the year 2112 [13]. The conventional fossil fuels not only pose the challenge of going extinct upon over-exploitation but also have significant impact on the environment. These fuels emit large quantities of CO_2 upon being burnt for the purpose of generating electrical energy as shown in Figure 1.2.

1. Introduction

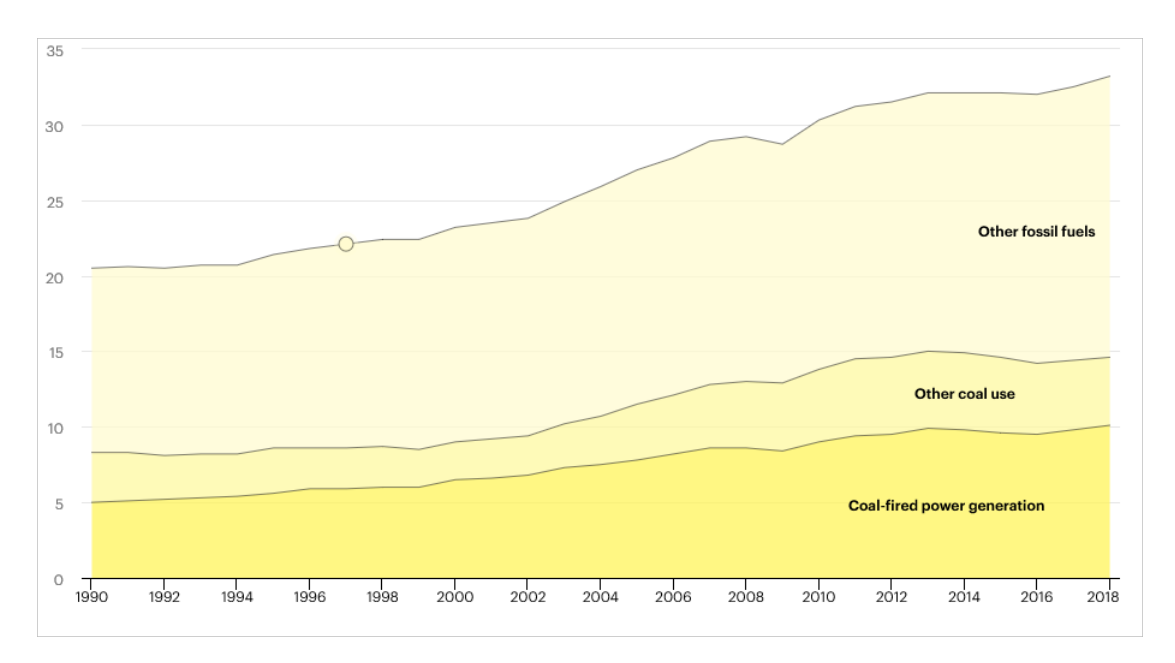


Figure 1.2: Global energy-related carbon dioxide emissions by source in Giga-tonnes [2]

The emitted CO_2 from burning of fossil fuels for electrical energy generation contributes to about 1/3rd of GHG emissions which subsequently leads to depletion of the ozone layer and thereby causes global warming [14]. Therefore, to mitigate such drastic climate change, there is an urgent need to shift to renewable energy sources such as Solar Energy, Wind Energy, Biomass, etc. for electrical energy production despite the fact that they are intermittent in nature.

Currently, the renewable sources contribute to about 19% of the electrical energy generated and is projected to increase to about 38% by the year 2050 as shown in Figure 1.3. There are also detailed studies that classify the various renewable sources and their contribution to energy generation and it can be noted that the usage of Solar Energy is projected to have the highest contribution towards electrical energy generation in the near future as shown in Figure 1.4.

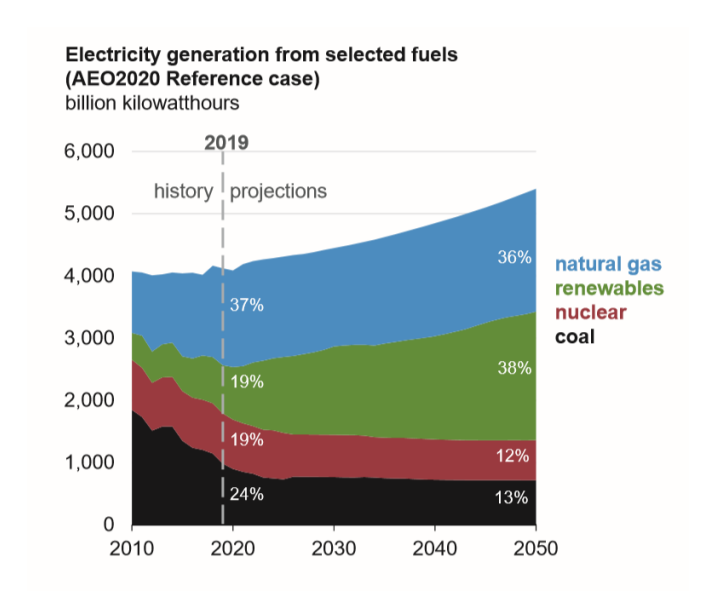


Figure 1.3: Contribution of various sources towards generation of electricity [3]

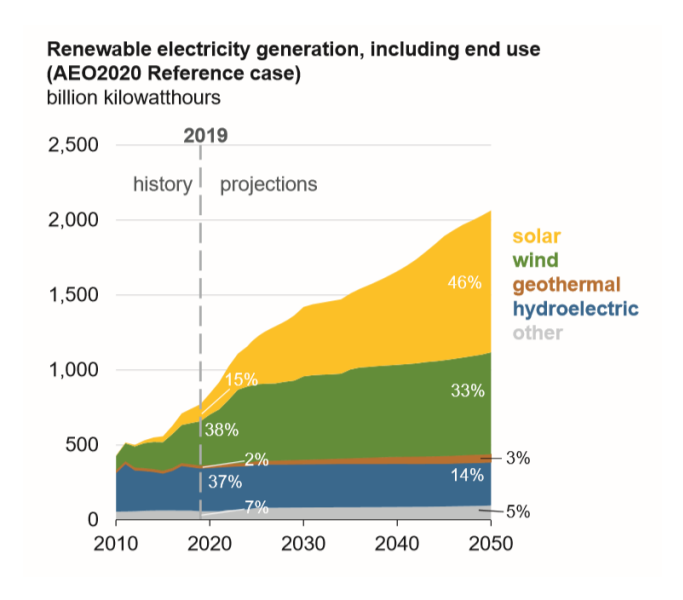


Figure 1.4: Contribution of various renewable sources towards generation of electricity [3]

The conversion of Solar energy into electrical energy is facilitated by Photovoltaic devices, which operate on the principle of Photovoltaic effect. Recently, the PV renewable technology is being used more commonly owing to the fact that its production cost have been reduced significantly. This can be attributed to the upscaling of production line along with the increase in industrial experience [15]. Despite their intermittent nature being a cause of mismatch between energy supply and demand, there are possibilities of using various storage technology for collecting the excess energy through batteries, green hydrogen, chemical fuels, etc. The usage of batteries may not necessarily be a cost-effective option in the long term, hence green hydrogen generation through splitting water molecules is more suitable. The green hydrogen in reaction with ${\rm CO_2}$ can be used to form chemical fuels. Since, a specific potential difference is needed for the aforementioned reaction to occur, this thesis focusses on developing a Germanium (Ge) based bottom cell for a multi-junction solar cell. Such a multi-junction device is needed to obtain the required voltage along with an increase in spectral utilization of the incident solar spectrum so as to be implemented in photo-electrochemical devices.

1.2. Working Principle of a solar cell

Figure 1.5 depicts the Sun's spectral irradiance and how it varies as a function of wavelength. The overall smooth spectral curve highlighted in yellow is the idealized radiation of a blackbody, and the curve highlighted in orange denotes the AMO spectrum which is the irradiance measured immediately outside the earth's atmosphere, while the other curve denotes the AM1.5 spectrum which is the terrestrial irradiance measured at Sea level.

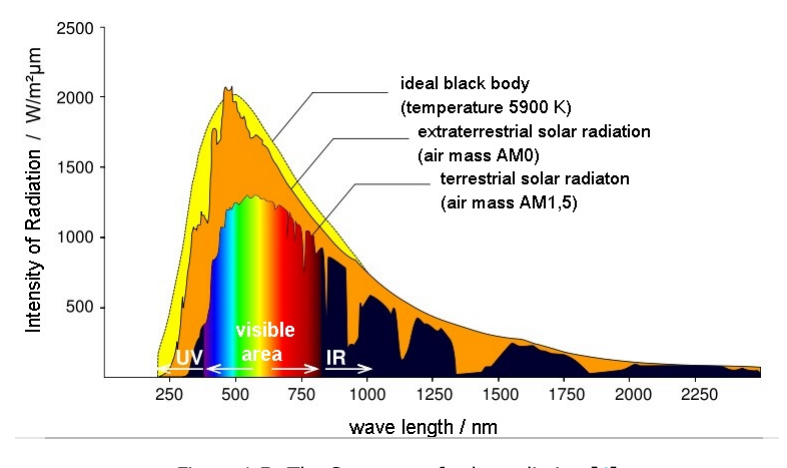


Figure 1.5: The Spectrum of solar radiation [4]

4 1. Introduction

The light source comprises of photons with different energies depending on their wavelengths, which is explained in detail later in this section. The total irradiance value of the AM1.5 spectrum is calculated, using Equation $1.1\,[5]$, taking into account the photon flux at each wavelength. The integral range used for the calculation is the entire spectral range of Sun's spectrum and the irradiance is found to be equal to $1000\,\mathrm{W/m^2}$.

$$I_e = \int \frac{hc}{\lambda} \phi(\lambda) d\lambda \tag{1.1}$$

where, I_e is the Irradiance in W/m^2 , and, $\phi(\lambda)$ is the spectral photon flux at wavelength λ .

The basic principle behind the working of a Solar cell is the Photovoltaic effect and it is defined as the process in which an electrical voltage/potential difference is generated at the junction of two dissimilar materials that are in close contact when struck by incident EM radiation from the Sun [16]. This EM radiation or incident light from the Sun comprises of discrete packets of energy known as photons, where each photon has a specific Energy (E) that depends on its specific wavelength as denoted in Equation 1.2 [5].

$$E = \frac{hc}{\lambda} \tag{1.2}$$

where, h is the Planck's constant, c is the speed of light (EM wave), and, λ is the wavelength of light (EM wave).

The positions occupied by an electron in any ideal semiconductor material are either below the valence band which is denoted by E_v or above the conduction band which is denoted by E_c . The difference between the valence and conduction bands denotes the bandgap of a semiconductor material as seen in the Energy Band diagram shown in Figure 1.6.

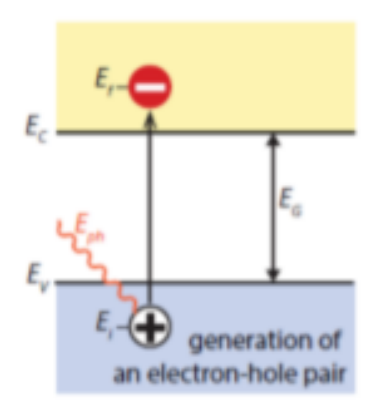


Figure 1.6: Energy band diagram of a semiconductor material [5]

The basic Photovoltaic effect in a Solar cell is described as follows; When the light is incident on the material, it transfers its energy to the electrons in the valence band of the material and they move to a higher level which corresponds to the electron's final energy. If this energy is equal to or higher than the threshold (bandgap) value then the electron gets excited to the conduction band, thereby leaving a "hole" in the valence band. Furthermore, once the charge carriers are generated, there is a good chance that they can recombine and energy is released. To avoid this, the generated charge carriers are to be separated and this is achieved through the creation of an electric field by using doped layers on either side of the semiconductor absorber material. Finally, the charge carriers are collected in an external electric circuit to utilize the energy stored in them after which they are allowed to recombine. This is schematically represented by a simple flowchart as shown in Figure 1.7.

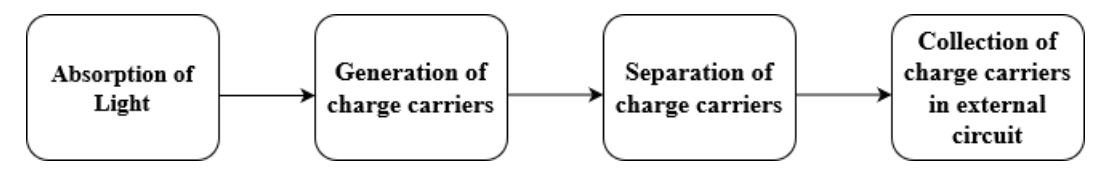


Figure 1.7: Schematic diagram of the working of a solar cell

As discussed earlier, the absorption of incident light is ideal when the incident photon has an energy equal to or higher than the bandgap of the semiconductor material. However, there is a possibility of the occurrence of two other conditions. When the incident photon has an energy that is either less than the bandgap energy or much higher than the bandgap energy of the semiconductor material then these correspond to non-absorption and thermalization, respectively. The two aforementioned terms are basically primary losses in a single-junction solar cell and are depicted schematically in Figure 1.8.

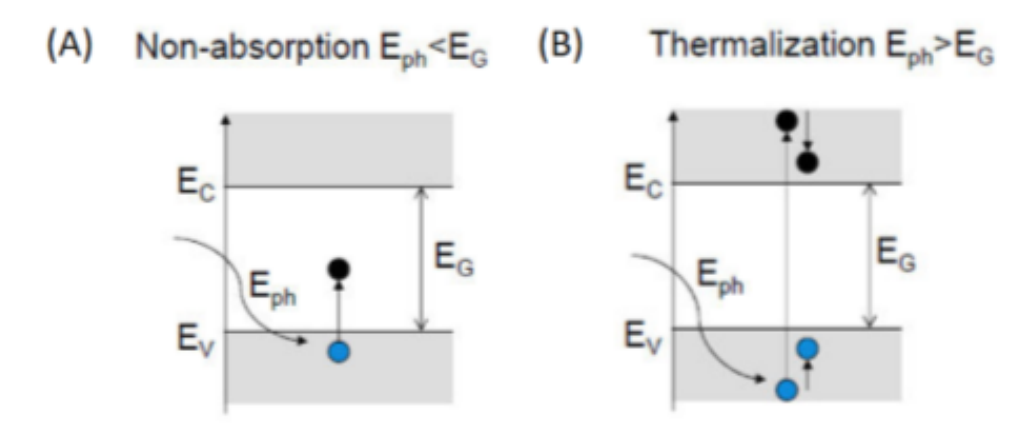


Figure 1.8: Representation of (a) non-absorption loss and (b) thermalization loss [5]

In the case of non-absorption, where $E_{ph} < E_g$, there is no charge carrier generation and in the case of thermalization , where $E_{ph} \gg E_g$, the electrons are excited to a much higher state in the conduction band only to eventually come down to a lower conduction state along with the release of the excess energy as heat. A single–junction solar cell also experience electrical losses along with these spectral mismatch losses and taking all these into account there is a theoretical efficiency limit which is commonly known as the Shockley-Queisser (SQ) limit [17]. Based on this SQ limit, for a single-junction solar cell with a Eg of 1.34 eV, the maximum theoretical efficiency at AM1.5 spectrum is found to be 33.1% [5] as shown in Figure 1.9.

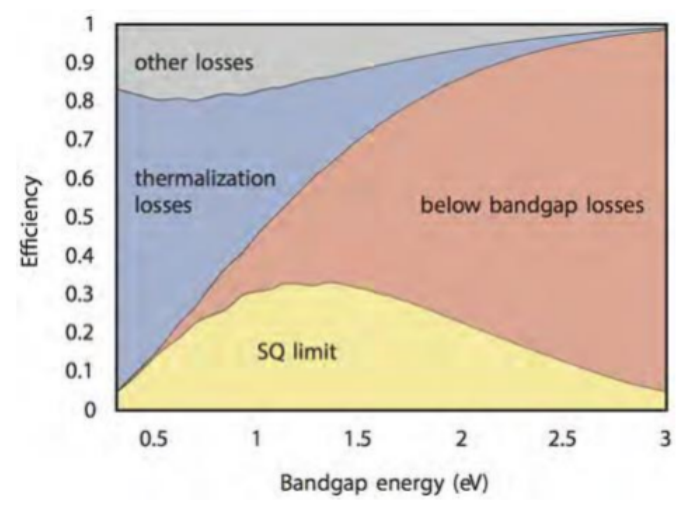


Figure 1.9: Shockley-Queisser limit of a single-junction solar cell with various primary losses [5]

6 1. Introduction

The SQ limit is applicable for the case of a direct bandgap semiconductor material, where the radiative recombination mechanism is the dominant recombination technique. However, if a semiconductor material with an indirect bandgap is considered such as c-Si, where the dominant recombination mechanism is the Auger recombination, then the maximum theoretical efficiency limit is defined by Richter et. al. [18] and it is found to be 29.43%. The difference between a direct and indirect bandgap material can be simplified as follows,

- In a direct bandgap material, the E_{ph} is sufficient to excite and electron the valence band, E_v to the conduction band, E_c .
- Whereas, in an indirect bandgap material, an extra momentum is also required apart from the E_{ph} .

This difference between direct and indirect bandgap semiconductor materials is also graphically depicted in Figure 1.10.

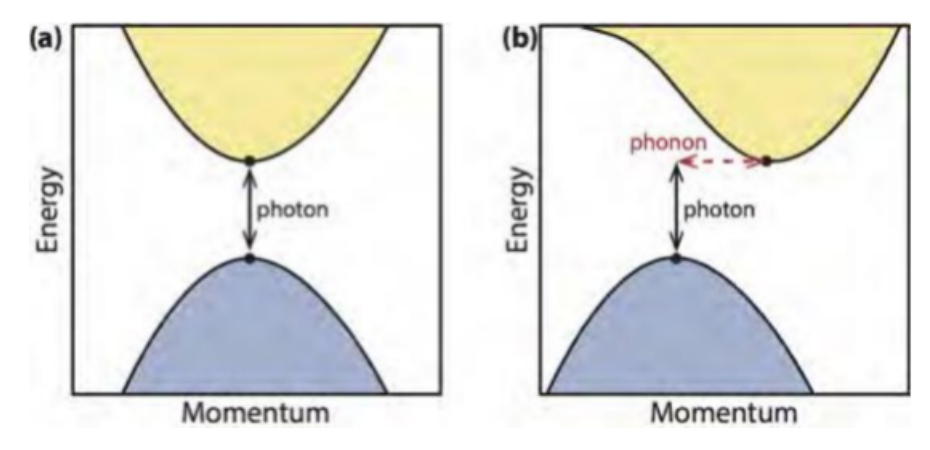


Figure 1.10: (a) Direct bandgap semiconductor; (b) Indirect bandgap semiconductor [5]

1.3. History of solar cells

Solar cell technologies have been developed for more than a century and they can be classified into three separate generations of cell technologies. The $\mathbf{1}^{st}$ Generation solar cell technologies are the Wafer-based cells, while the $\mathbf{2}^{nd}$ Generation refers to Thin-film cells.

1.3.1. Wafer-based cell technology

For nearly half a century now, Wafer-based solar cells such as c-Si have been developed having thicknesses ideally in the range of few hundred micrometres. These cells are known to be some of the most commonly used technology as a result of their relatively high efficiencies. Generally, they are classified into two main categories, namely the mono-crystalline and multi-crystalline cells, based on the level of crystallization.

1.3.2. Thin-film cell technology

The 2^{nd} Generation cell technology comprises of much thinner cells in the thickness range of about few hundred nanometres, which albeit having lower efficiencies than the c-Si technology, were produced owing to various benefits such as flexibility, ease of fabrication, etc. These thin-film cell technologies are also ideally suited for Building-Integrated (BIPV) applications when deposited on flexible substrates.

The Si based thin-film cell technologies predominantly tend to comprise of p-i-n junctions rather than the conventional p-n junctions present in other thin-film technologies such as CIGS and CdTe. The main motive behind this is the reduction of recombination in the intrinsic/undoped layer which has equal electron and hole concentration and hence making this layer less defective. Such a configuration with doped layers on either sides proves useful in creating an electric field across the p-i-n junction which in turn aids in effective charge carrier separation and collection as discussed in the previous

section. Therefore, thin-film cells are considered to be drift-based devices, while wafer-based cells are considered to be diffusion-based devices owing to their reliance on carrier concentration gradient.

The other 2^{nd} generation cell technology such as Perovskites are cost-effective due to its abundancy and also have the capability to challenge the SQ limit. However, this technology is still in its early stages of research.

1.3.3. Multi-Junction Devices

From Figure 1.8, it can be deduced that cells with large bandgap mainly suffer from non-absorption and similarly those with lower bandgap suffer from thermalization. To negate these losses, a multi-junction device with high bandgap cell acting as the top cell and low bandgap cell acting as the bottom cell can be formed. Such a multi-junction configuration can contain anywhere between 3-4 junctions with absorber materials having different bandgap values are stacked on one another. This technique also ensures that there is a better utilization of the solar spectrum and also an improvement in the efficiency [5].

1.4. Motivation behind multi-junction device

As discussed in the previous section, a multi-junction device proves useful in obtaining an improved efficiency along with better utilization of the solar spectrum. Si, in general, is a commonly used, stable, economically feasible material and devices based on Si have quite a good market share [5]. Si cell technologies such as a-Si:H (1.6-1.8 eV), along with a-SiGe:H (1.4-1.6 eV) and nc-Si/c-Si (1.1-1.3 eV) have already been used to obtain triple-junction device [8]. Therefore, the motivation is to develop a cost-effective absorber material having quite a low bandgap to absorb sufficient light below the nc-Si/c-Si cell such that it is not current-limiting in a multi-junction configuration. This could potentially boost the efficiency of the Si-based multi-junction device. An a-/nc-Ge:H cell or a Ge based alloy material such as a-/nc-GeSn:H with a tunable bandgap based on its composition can be used for this purpose as shown in Figure 1.11.

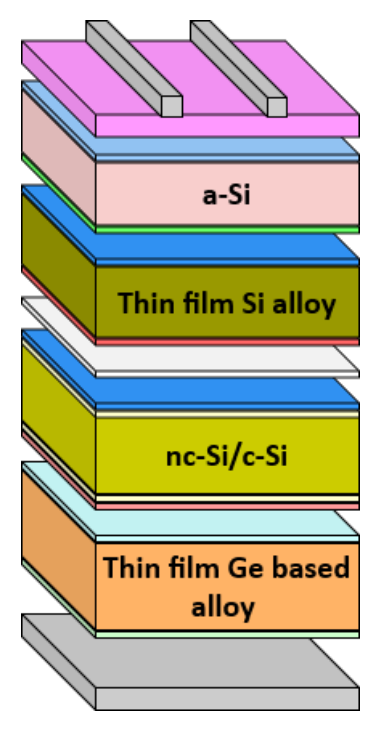


Figure 1.11: Basic structure of a thin film quadruple junction solar cell

8 1. Introduction

1.5. Goal and Outline of the Thesis

The overall goal of this project is to find a device quality Ge:H absorber layer that can be used in a multi-junction PV device. The research objective is two-fold. Firstly, the influence of various deposition parameters such as deposition pressure, deposition power, H_2/GeH_4 dilution ratio, deposition temperature have on the optical, electrical and material properties are characterized, and this is set to result in a range of Ge:H films that can be used as absorber layers. Secondly, a selection of absorber layers are used to form a single junction p-i-n superstrate solar cells and its J-V parameters are characterized.

The structure of this thesis report is as follows: The introduction to this topic is already covered in this chapter. Furthermore, Chapter 2 emphasizes on the theoretical background of this thesis work. Chapter 3 deals with the experimental methodology and the various measurement techniques that were used to characterize the individual Ge:H films and solar cells. Chapter 4 highlights the processing pressure-power range in which the dusty regime can be avoided so as to obtain successful film depositions. Chapter 5 investigates on the effects of various deposition parameters on the film characteristics. Chapter 6 presents the results of the p-n & p-i-n superstrate single junction solar cell. The thesis report will then conclude with Chapter 7, where the most optimal results and/or trends are summarized along with a brief recommendation for further improving the performance of the cell that could be useful for future research.

Theoretical Background

This chapter provides valuable information on basic physics concepts and intrinsic material properties that are involved in this work on PV, and hence provides a theoretical background for this thesis. In this chapter, section 2.1 discusses about the optical properties, and this is followed by sections 2.2 and 2.3 where the electrical and material properties are discussed.

2.1. Optical Properties

Light when incident on a medium generally leads to three outcomes and these are, reflection of light at the surface of the material, absorption by the material and the transmission of light through the material. For a solar cell, it is ideal if all the incident light is absorbed. Although, this is not true in reality. The equation 2.1 describes the basic energy conservation law whenever a light is incident on a medium.

$$R + T + A = 1 \tag{2.1}$$

where Reflectance, Transmittance and Absorptance are dimensionless quantities.

2.1.1. Optical Reflection and Optical Transmission

The interface of two different mediums along with the reflection and transmission undergone by the incident light is shown in Figure 2.1. Based on the refractive index (n) of the respective medium, the speed at which the light propagates varies in different mediums. This change is the cause of a fraction of light to be reflected and transmitted at the interface of the two media. Furthermore, the refractive index (n) of a medium can be defined as the ratio of the speed of light propagation in vacuum to the speed of light propagation in that medium.

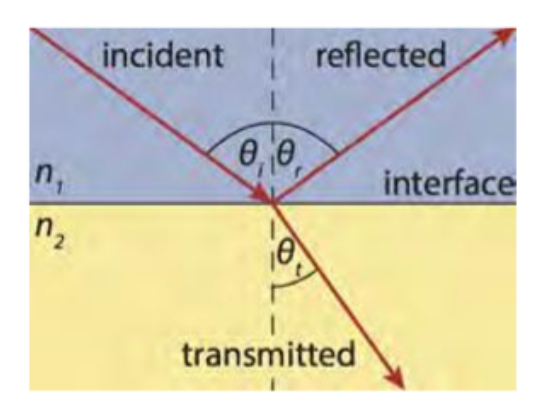


Figure 2.1: Behaviour of incident light a the interface off two different mediums [5]

The angle of the incident light with respect to the normal of the interface is known as the angle of incidence and it is equal to the angle of reflection. Snell's Law [19] describes the relation between the angle of incidence and the angle of transmission as shown in equation 2.2

$$\frac{n_1}{n_2} = \frac{\sin(\theta_t)}{\sin(\theta_i)} \tag{2.2}$$

where, n_1 and n_2 are the refractive indices of medium 1 and 2, and, θ_i and θ_t are the angle of incidence and transmission respectively.

The components of an electromagnetic wave such as the perpendicular electric and magnetic fields are generally orthogonal to the direction in which the wave propagates. The orientation of the electric field with the plane of incidence is defined by the term polarization. There are two types of polarization, namely the s-polarized and p-polarized light. When the electric field orientation is perpendicular to the plane of incidence it is termed as s-polarized light, and while the electric field orientation is parallel to the plane of incidence it is termed as p-polarized light. Fresnel's equation [20] describes the relation between the incident, reflected and transmitted waves.

The transmitted and reflected wave for s-polarized light are as follows,

$$t_s = \frac{2n_1 cos\theta_i}{n_1 cos\theta_i + n_2 cos\theta_t}$$
 (2.3)

$$r_s = \frac{n_1 cos\theta_i - n_2 cos\theta_t}{n_1 cos\theta_i + n_2 cos\theta_t}$$
 (2.4)

The transmitted and reflected wave for p-polarized light are as follows,

$$t_p = \frac{2n_1 cos\theta_i}{n_1 cos\theta_t + n_2 cos\theta_i} \tag{2.5}$$

$$r_p = \frac{n_1 cos\theta_t - n_2 cos\theta_i}{n_1 cos\theta_t + n_2 cos\theta_i}$$
 (2.6)

The light emitted by the sun is unpolarized in nature, hence equal amount of s and p polarized light is emitted, so the total reflectance is defined as shown in equation 2.7. In the case of normal incidence, $\theta_i = \theta_t = 0$, and hence equation 2.7 can be further simplified as shown in 2.8.

$$R = \frac{1}{2}(r_s^2 + r_p^2) \tag{2.7}$$

$$R = \left| \frac{n_1 - n_2}{n_1 + n_2} \right|^2 \tag{2.8}$$

An important phenomenon that can be obtained from Snell's law is the total internal reflection. From Figure 2.1, if $n_2 > n_1$ then there exists a critical angle θ_{crit} . When $\theta_2 \ge \theta_{crit}$, then the light cannot leave the medium 2 and is totally internally reflected back into medium 2 [5]. To have all the light refracted in the cell, it is necessary to minimize the transmittance to the least possible level.

$$sin(\theta_{crit}) = \frac{n_1}{n_2} \tag{2.9}$$

2.1.2. Optical Absorption

A fraction of light is absorbed by the medium through which the light is propagating when the photon energy is greater the energy required to excite the electron. This is accounted for in the overall equation 2.1 specified earlier in the chapter, where A denotes the Absorptance in the medium.

In the complex refractive index ($n+i\kappa$), n is the real part and κ is the imaginary part which is also referred to as the wave number. The attenuation of the electromagnetic field intensity with regards to the distance travelled in a medium is defined by the Lambert-beer law [21] as shown in equation 2.10.

$$I(x) = I_0 \exp(-\alpha x) \tag{2.10}$$

where, I is the EM wave intensity, x is the distance travelled in the medium, α is the absorption coefficient.

The absorption coefficient is a critical parameter that can be obtained from the spectroscopic ellipsometry test. It is dependent on the wavelength and also the extinction coefficient κ as shown in equation 2.11.

$$\alpha(\lambda) = \frac{4\pi\kappa(\lambda)}{\lambda} \tag{2.11}$$

where, λ is the wavelength of light.

Furthermore, the absorptance $A(\lambda)$ can be calculated as the product of the absorption coefficient (α) and the thickness (d) of the medium, as shown in equation 2.12.

$$A(\lambda) = \alpha(\lambda)d\tag{2.12}$$

2.2. Electrical Properties

The electrical properties determine the post-light absorption processes and hence they are quite important. A sufficient conductivity is vital in ensuring that the charge carriers generated upon light absorption are subsequently separated and collected.

2.2.1. Conductivity

The extent to which electricity conduction occurs in a given material is defined as its conductivity (σ). It also quantifies the current carrying capability of the material and it is calculated as shown in equation 2.13 and it is measured in Siemens per meter.

$$\sigma = \frac{1}{R_{TEMP}} \frac{d_{gap}}{dl} \tag{2.13}$$

where, R_{TEMP} is the temperature dependent resistance, d_{gap} and I are the gap between the contacts and contact length respectively, and, d is the thickness of the layer

Temperature plays a major role in determining the conductivity. An increase in the temperature can cause the resistivity to decrease and hence result in an increase in conductivity, which can be verified from the previous equation 2.13. There are certain materials which may exhibit anisotropic conductivity, which refers to conductivity differences based on measurement direction. Conductivity measured along growth direction is known as transverse conductivity, and a high transverse conductivity ensures the collection of the charge carriers. The other conductivity measured along the plane of the layers is known as the lateral conductivity and it is not as critical [6]. A schematic representation of the transverse and lateral conductivity in a cell is shown in Figure 2.2.

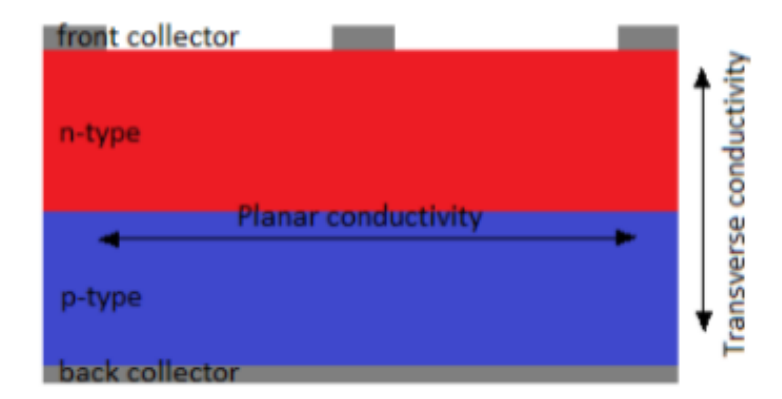


Figure 2.2: Transverse vs lateral conductivity in a cell [6]

2.2.2. Activation Energy

The activation energy (E_{act}) is defined as the energy that is required for an electron in a valence state to be excited to a conduction state. The difference in the fermi level (E_F) in an intrinsic and doped semiconductor material are as follows, the fermi level lies halfway across the bandgap (E_g) in an intrinsic material and near one of the bands in a doped material. In a n-doped material, the fermi level is near the edge of the conduction band and vice-versa for a p-doped material. Hence, the E_{act} of an n-doped layer can be defined as the difference between the conduction band edge and the fermi level. The electrons can easily be excited to a conduction state, if the material has low activation energy. Therefore, a high conductivity is obtained for low activation energy and this can be verified by the Arrhenius equation (2.14).

$$\sigma(T) = \sigma_o \exp(\frac{-E_{act}}{k_B T}) \tag{2.14}$$

where, σ_o is the material dependent conductivity constant, k_B is the Boltzmann constant, and, T is the Temperature (°K)

2.3. Material Properties

The basic material properties of Ge such as the structure, crystallinity, etc. are discussed in this section.

2.3.1. Basic lattice structure

The lattice structure is quite vital as it describes the intrinsic properties of the material. Germanium (Ge) is much heavier and has a higher atomic number than silicon (Si) which is the conventional material used for PV applications. However, the lattice structure for a material like germanium (Ge) is comparable to that observed in silicon (Si), as they belong to the same Group IV in the periodic table having 4 valence electrons in their respective valence shells. The crystalline phase exhibits a tetrahedral diamond-like structure and hence crystalline structure tend to have long range order. However, amorphous phase materials do not show long range order and contain large number of unbonded Ge atoms/dangling bonds due to variations in distances as well as bond angles. The presence of such dangling bonds are related to the defect density in the material and generally tends to affect the electrical properties discussed in the previous section (2.2). Hence, the passivation of these dangling bonds using hydrogen (H) is quite necessary, where most of the Ge atoms are bonded covalently to other neighbouring Ge atoms while the hydrogen atom bonds to the leftover valence electron [7]. The role of deposition parameters is therefore very critical as they influence, amongst other things, the lattice structure of the material. The variation of crystalline fraction with respect to the variation of deposition parameters is shown in Figure 2.3.

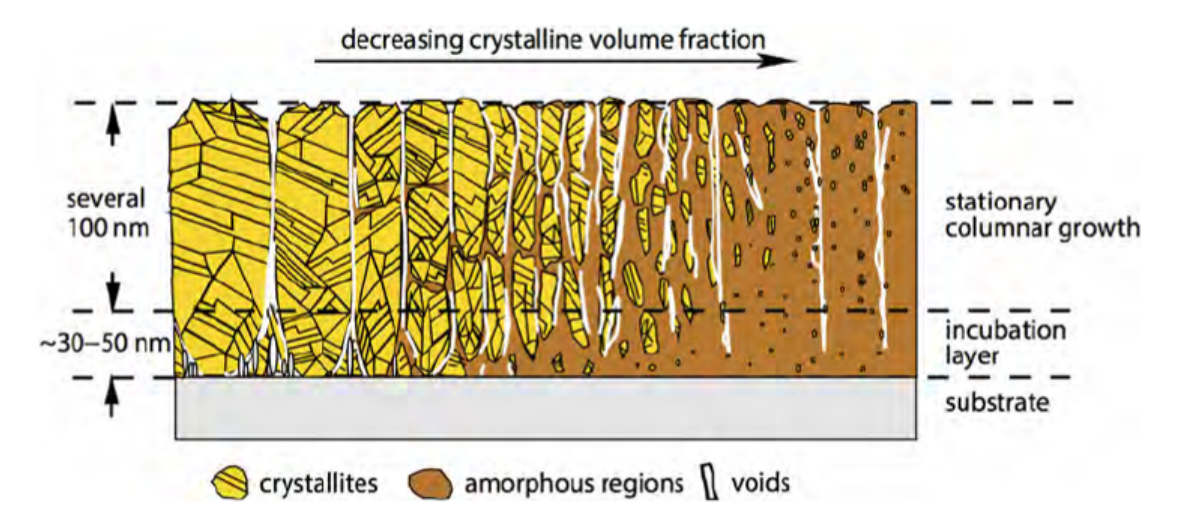


Figure 2.3: Variation in crystalline fraction with respect to deposition parameters [5]

2.3.2. Crystallinity

The crystallinity of the material is determined using the equation described below (2.15),

$$X_{c} = \frac{I_{c-Ge}}{I_{c-Ge} + \gamma I_{a-Ge}}$$
 (2.15)

where, X_c is the crystalline fraction, I_{c-Ge} and I_{a-Ge} are the crystalline peak and amorphous peak areas respectively, and, γ is the correction factor for cross section difference for phonon excitation of c-Ge with respect to a-Ge and a value of 0.85 is adopted for it as per PVMD group of TU Delft [22].

2.3.3. Defects

There are various types of defects that can be found in a material, however in the case of an a-Ge, dangling bonds are the most prominent as discussed in section 2.3.1. These dangling bonds defects have certain energy levels within the bandgap which consequently results in the recombination of the generated charge carriers and thereby preventing them from contributing towards energy generation. In a crystalline lattice having a long-range spatial order, there exists well-defined energy band states along with a clear forbidden energy gap. This can be attributed to the ability of the electron to occupy a large number of states in both the bands. However, in the case of an amorphous lattice, due to the disorder in the lattice structure, there exists tail states for both the bands in the bandgap. Furthermore, the defects in this material create defect states in between the tail states that can be occupied by the charge carriers. Therefore, the bandgap is not properly defined anymore and hence the term mobility gap (E_{mob}) is used to define the energy difference between the conduction and valence band edges. It is to be noted that these principles are comparable for both a-Si as well as a-Ge.

2.3.4. Bandgap

The different bandgaps used in this thesis are the Tauc Bandgap (E_{TAUC}), the E_{04} and the E_{03} optical bandgaps. These bandgaps are obtained upon fitting the Tauc-Lorentz model [23] to the measured SE data. The absorption coefficient from the fitted data is used to calculate the Tauc bandgap using the equation 2.16.

$$E_{TAUC} = (\alpha h \nu)^{\frac{1}{r}} \tag{2.16}$$

where, r denotes the nature of transition, h is the Plank's constant, ν is the Frequency of light, and, α is the absorption coefficient.

A Tauc plot generally is a plot of the quantity $(\alpha h v)^{\frac{1}{r}}$ with respect to the energy of light (hv) from which the Tauc bandgap is calculated upon extrapolation. On the other hand, the E_{04} and the E_{03} optical bandgaps are defined as the energy at which the material's absorption coefficient equals $10^4 cm^{-1}$ and $10^3 cm^{-1}$ respectively, where the absorption coefficient is obtained using the equation 2.16.

Experimental Methodology

This chapter consists of 3 main sections that are specified in chronological order in which the experiments were performed. The first two sections 3.1 and 3.2 give an overview of the steps involved in the overall process and highlights the basic sample preparation/cleaning procedure carried out before the fabrication technique, respectively. It is followed by section 3.3 where all the fabrication techniques involved in the deposition of various layers and solar cells are discussed. Furthermore, in the final section 3.4, the characterization techniques used in this thesis are discussed briefly.

3.1. Overview of Process

In this thesis, the solar cells processed are of the p-i-n superstrate configuration which is schematically depicted in the Figure 3.1, where the cell fabrication begins with the glass and is followed by the front Transparent Conductive Oxide (TCO) and the rest of the layers specified in more detail by the flowchart (3.1) shown previously. In this configuration, the light enters the cell from the top via the transparent glass. In Figure 3.2, a flow chart describing the steps involved in the overall fabrication technique for both individual Ge:H films and solar cells are depicted.

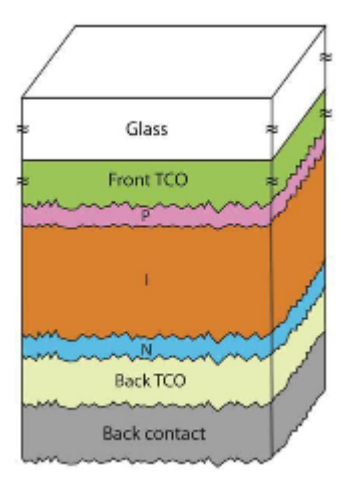


Figure 3.1: A p-i-n superstrate configuration [7]

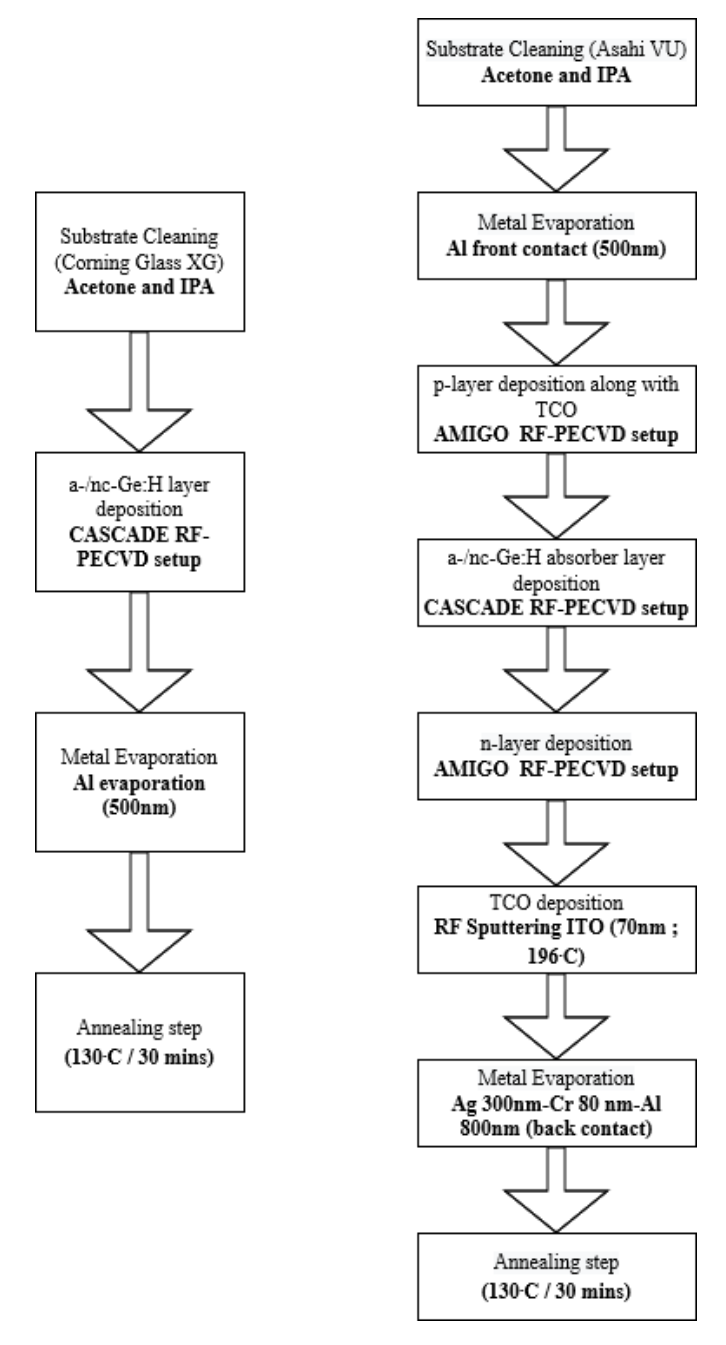


Figure 3.2: Stages involved in the fabrication of Ge:H layers (left) & the corresponding solar cell (right)

3.2. Preparation of Sample

In this thesis, the depositions were carried out on Corning Glass XG and Asahi VU substrates for the fabrication of films and solar cells, respectively. The glass substrates having dimensions of 10 cm x 10 cm were cut into 4 portions of 2.5 cm x 10 cm throughout the work. The most important step of the prefabrication sample preparation process is the ultrasonic bath cleaning. In this cleaning process, sonic waves were used to create bubbles in the bath to remove dust, finger marks,etc. from the surface of the sample. Hence, the samples are are free of dust and other contaminants before being used for fabrication [24]. This cleaning procedure in the bath is carried out using acetone for 10 minutes followed by drying using nitrogen air and then using isopropanol (IPA) for another 10 minutes followed by nitrogen air drying. It is important to specifty that the Asahi VU substrate used for the solar cells is a textured SnO_2 coating on the glass, that is beneficial for improved light trapping for the cells.

3.3. Fabrication techniques

3.3.1. Plasma Enhanced Chemical Vapour Deposition

The deposition of thin film p, i, and n layers were carried out using a radio-frequency plasma enhanced chemical vapour deposition (RF-PECVD) technique. The typical PECVD reaction chamber is depicted in Figure 3.3. The combination of a variety of pumps such as turbo-molecular and foreline pump are used to maintain ultrahigh vacuum conditions inside the chamber so as to make sure that the chamber is devoid of any impurities/dust. There is a heater which is used to control the temperature of the chamber. There exists a couple of electrodes, one of which is grounded on which the substrate holder can be mounted while the other electrode is connected to the RF generator. The chamber also has connections to the gas units via mass flow controllers and based on the deposition to be made the appropriate precursor gases are allowed to flow.

Once the cleaned samples are placed on the holder and mounted to the grounded electrode, an alternating voltage at radio frequency is supplied to the other electrode which is also known as the powered electrode. This induces an oscillating electric field that leads to plasma production. Upon plasma production, the lighter electrons are dispatched from the orbitals which consequently leads to the creation of positive ions of the gas molecule. These positive ions contribute to the film growth due to the lower potential of the substrate in the grounded electrode with respect to the plasma.

The process of PECVD based deposition can be carried out at different pressures, RF powers, temperatures, gas flow rates, deposition times. These deposition parameters are also quite influential on the properties of the deposited material.

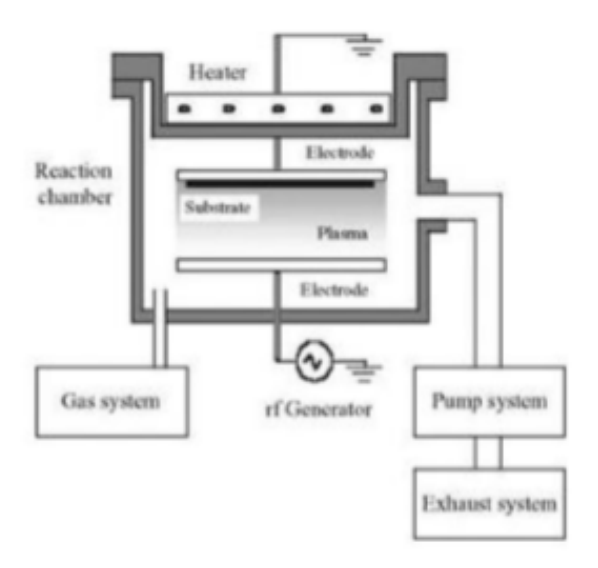


Figure 3.3: Schematic diagram of a RF-PECVD system [8]

The fabrication of the Ge:H films on the Corning Glass substrates and those on the Asahi VU substrates for the i layer of the cells were performed in the RF chamber of a Cascaded Arc Solar Cell Apparatus Delft Eindhoven (CASCADE) setup. This setup is depicted in Figure 3.4 and apart from the RF chamber it also consists of a central load lock, and an ETP-CVD chamber. A RF generator is connected to the RF chamber's circular bottom electrode that is adjustable in height from the outside [25]. The fabrication of the p and n layers for the solar cells were performed in the AMIGO RF-PECVD by Elettrorava s.p.A [26], which consists of six deposition processing chambers (DPC), a load lock chamber (LLC) and a transfer chamber (TC).



Figure 3.4: The CASCADE system (PVMD Group)

3.3.2. RF Magnetron Sputtering

The RF Magnetron Sputtering technique is used for the deposition of the transparent conductive oxide (TCO) of the solar cells in this thesis work. Magnetron Sputtering is a type of the Physical Vapour Deposition technique [5]. The substrate is generally mounted on the anode and the target material is contained in the cathode. A vacuum chamber with an inert Argon (Ar) atmosphere are the conditions in which this process takes place. The plasma of Argon is produced between the electrodes due to an alternating electromagnetic field, and this is accompanied by the ions of the argon gas molecule bombarding into the target material surface and hence leading to release of target material atoms. Furthermore, these atoms tend to diffuse towards the substrate present in the anode and thereby result in growth of the required TCO. A typical RF magnetron sputtering apparatus is shown in Figure 3.5.

In this thesis, a sputtering unit known as Zorro was used to deposit 70 nm of Indium-doped Tin Oxide (ITO) for the p-i-n solar cell and the ITO taget comprises of 10% SnO₂ and 90% In₂O by weight.

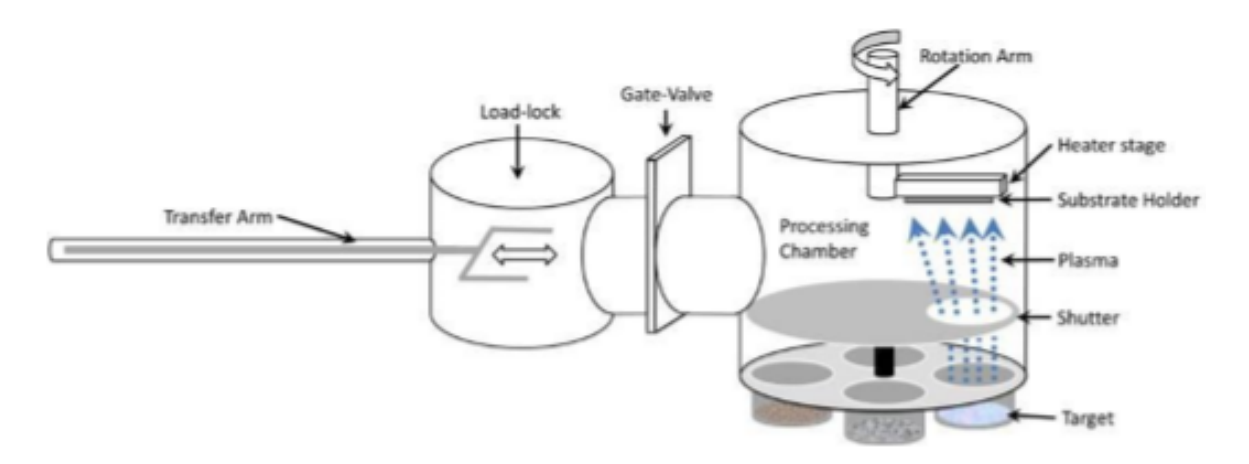


Figure 3.5: Schematic representation of RF magnetron sputtering system (PVMD Group) [7]

3.3.3. Metal Evaporation

For the sake of depositing front and back contacts on the cells and contacts on the individual Ge:H films, the metal evaporation technique was used. This technique can be classified into two, namely, electron beam evaporation and thermal evaporation. In the electron beam evaporation, an high intensity electron beam is focused on the target material that is present in a crucible, hence heating up the target. Meanwhile, in the thermal evaporation, a high current is passed through the crucible with the

target material on it. The target material starts evaporating upon reaching its melting point and this is applicable for both the processes [5]. A typical schematic depiction of the metal evaporation unit is shown in Figure 3.6, where vacuum conditions prevail inside the chamber to reduce oxidation of the metallic depositions and the stage is rotated at 10 rpm speed for the sake of improving uniformity of the depositions [27].

In this thesis, a metal evaporation unit known as Provac was used to deposit 500 nm Aluminium (AI) contacts for individual Ge:H films and for the front contact of the cell. For the back contact of the cell 80 nm of Chromium (Cr), 800 nm of Aluminium (AI) through electron beam technique and 300 nm of Silver (Ag) through thermal technique were deposited.

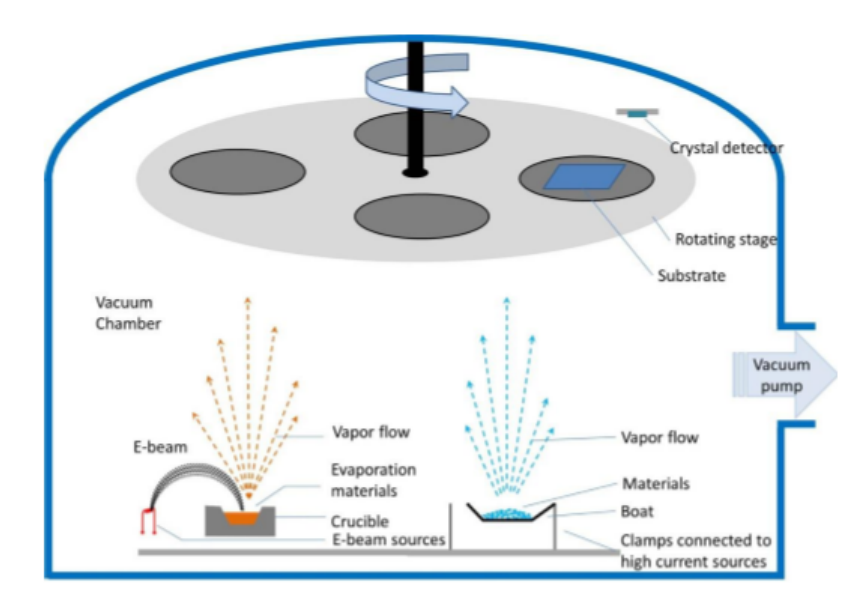


Figure 3.6: Schematic representation of the metal evaporation chamber [7]

3.3.4. Annealing step

The final step before the measurements are carried out on the fabricated layers and cells is the annealing step. This step is performed to ensure proper adhesion of the contacts and to release any stress that might have been developed during the growth stage. This process is carried out for a duration of 30 minutes at a temperature of 130°C in a Heratherm Thermo Scientific oven.

3.4. Characterization techniques

In this section the various techniques used for the characterization of individual Ge:H films as well as solar cells based on their electrical and optical properties are discussed.

3.4.1. Dark Conductivity and Activation Energy

The temperature-based conductivity measurements of a semiconductor material prove useful in determining the activation energy and the dark conductivity of the material. The dark conductivity parameter can provide an insight on the defect density in the material and the detrimental effects it has on the material's electrical properties. These measurements are carried out in the dark and they measure the J-V curves based on the temperature. The temperature range in which these measurements are carried out is from 130°C-60°C with 5°C step variation.

Equation 3.1 represents the formula that is used to calculate the dark conductivity of a given semi-conductor material.

$$\sigma_d(T) = \frac{dI(T)}{tlV(T)} \tag{3.1}$$

where, t is the thickness of the contacts in mm, d is the distance between the contacts in mm, I is the length of the contacts in mm, I(T) and V(T) are the current and voltage measured as a function of temperature.

In this thesis, the dark conductivity is measured in the Keithly 6517A electrometer setup for the films deposited on the Corning Glass XG substrate that have a thickness of around 100 nm. These Ge:H films have 500 nm Al contacts which were evaporated onto it and were then annealed at a temperature of 130°C in a Heratherm Thermo Scientific oven for 30 minutes.

As discussed earlier in section 2.2.2, the activation energy is defined as the energy required for an electron in a valence state to be excited to a conduction state. Based on the Arrhenius equation as shown in equation 2.14, the slope of the dark conductivity vs 1000/T is used to obtain the activation energy.

3.4.2. Spectroscopy Ellipsometry

The spectroscopy ellipsometry measurements are used to determine the optical properties of the semi-conductor material. In this thesis, various optical properties of the material such as the thickness, Tauc bandgap, E04 and E03 bandgaps, refractive index (n) and the extinction coefficient (k) were obtained by performing this measurement technique. This technique is a non-destructive method that is also used to characterize the surface roughness of the material. The change in the polarization upon the reflection of the incident light off the surface is measured in terms of the amplitude ratio (Ψ) and phase difference (Δ) as shown in equation 3.2.

$$tan(\Psi). \exp^{\Delta} = \rho = \frac{r_p}{r_s}$$
 (3.2)

where, ρ is the complex reflectance ratio, r_p and r_s are the reflectivity of p and s-polarized light.

A simple schematic representation of the Spectroscopy ellipsometry (SE) technique is shown in Figure 3.7.

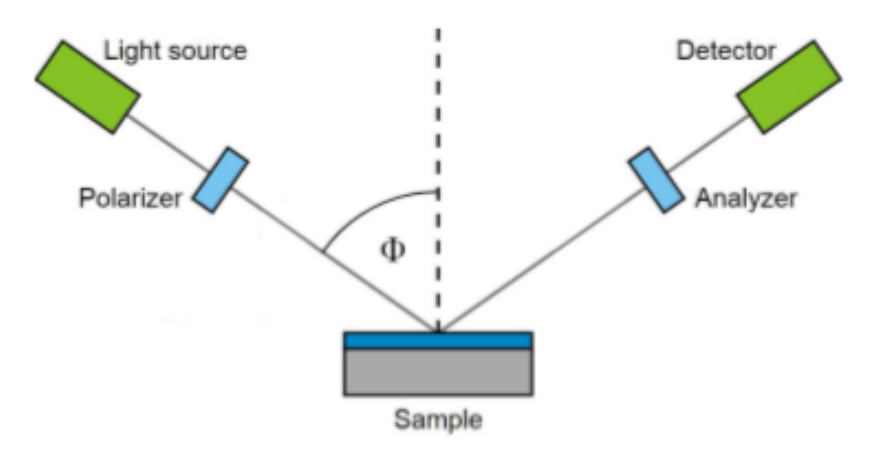


Figure 3.7: The schematic depiction of an ellipsometry setup [9]

The ellipsometry measurements are generally performed at angles close to the brewster's angle at which the ratio of r_p and r_s is maximal [6]. In this thesis, the M-2000DI spectrometer from J.A. Woolam Co. Inc. [28] was used to carry out the ellipsometry measurements.

Based on the material in which the measurements are carried out, various optical models are chosen so as to mimic the optical properties of the material. A software known as completeEASE which has an iterative approach is used to adjust the oscillator functions, thickness and roughness of the surface to fit the measurement curve with the chosen optical model [29]. Furthermore, when the mean square error between the measurement curve and the model is less than 10, the necessary optical data from the fitted model are extracted.

3.4.3. Raman Spectroscopy

The phases involved in the structure of the Ge:H films can be identified and quantified with the help of the Raman Spectroscopy technique. The basic underlying principle behind the working of this technique is the Raman shift, which is defined as the shift in frequency when the incident light collides with the atoms in the lattice of the measured material causing the scattering of the incident light. This shift can be classifed into Stokes-shift or anti-Stokes shift based on whether the wavelength and energy of the incident light is shifted up or down, respectively. The atomic structure and the different bondings involved between atoms are highlighted by the various stretching modes that occurs due to the interaction of the incident photons with the material's lattice.

In this thesis, a Renishaw inVia Raman microscope was used with a green laser having a wavelength of 514 nm acting as the source of the incident light. Since all the relevant stretching modes occurred in the range of 100 to 2200 cm⁻¹, this range was chosen for carrying out the measurements.

Peak Wavenumber (cm ⁻¹)	Bonds	Stretching Mode	Source
80	a-Ge	TA [transverse acoustic phonon mode]	[30] [31]
177	a-Ge	LA [longitudinal acoustic phonon mode]	[30] [31]
230	a-Ge	LO [longitudinal optic phonon mode]	[30] [31]
278	a-Ge	TO [transverse optic phonon mode]	[31] [32] [33]
297-300	nc-Ge	scattering at localized optical phonons in Ge nanocrystals	[34] [35]
295	c-Ge	single crystal germanium, non symmetric peak	[36]
300.7	c-Ge	single crystal germanium	[32] [37]
533	Ge-C		[38] [39] [40] [41]
540	Ge-H	wagging	[]

Table 3.1: Raman stretching mode peaks to their corresponding wavenumber for a-/nc-Ge:H

The table 3.1 lists the various possible Raman stretching mode peaks with their corresponding wavenumbers for an a-/nc-Ge:H material. In this thesis, the peaks that are identified as the the most important ones are as follows,

- a-Ge (Transverse optic phonon mode) at 278 cm⁻¹ corresponds to the amorphous fraction in the material.
- nc-Ge (scattering at localized optical phonons in Ge nanocrystals) at 297-300 cm⁻¹ can represent the nano-crystalline fraction in the material.
- c-Ge (single crystal germanium) at 300.7 cm⁻¹ can indicate the crystalline fraction in the material.
- Ge-H (wagging) at 540 cm⁻¹ can be a good indicator of hydrogen concentration in the material.

and the intensity of these peaks can be used to define the concentration of these bonds in the material. Furthermore, as discussed earlier in section 2.3.2, the crystalline fraction present in the material can be obtained.

3.4.4. Fourier Transform Infrared Spectroscopy

The Fourier Transform Infrared Spectroscopy (FTIR) technique is a useful method that defines the vibrational character of the material. When infrared light is incident on the material of interest, the chemical bonds present tend to wag, stretch and bend and hence the infrared light is adsorbed by these chemically bonded groups at specific wavenumber range [42]. An ideal FTIR spectrum comprises of peaks and these peaks correspond to the vibrational frequencies between the bonds of the atoms in the material. The FTIR measurement technique for a sample material is relative to a background material/substrate that is measured first. Therefore, the measurement of a sample material is in terms of either % transmittance or % absorbance that is devoid of the spectral peaks of the background material [43]. This technique is therefore quite useful in determining the amount of a specific material present in the film along with the various bonds involved and the stability shown by the material upon analysis of the measurement peaks with a data fitting procedure.

The data-fitting procedure for the FTIR absorbance spectrum was performed using the Fityk freeware [44]. Two important characteristics can be determined from the fitted spectrum, the hydrogen

concentration (C_H) in the film and the absorption coefficient of the summed GeO_x peaks (α_{GeO_x}), respectively. The hydrogen concentration (C_H) is determined by making use of the area under the Ge-H absorbance peak at $560 cm^{-1}$, using the equation 3.3 listed below.

$$C_H = \frac{\rho_{Ge}}{\rho_H} \left(A \frac{A_{abs}(\omega)}{d} \ln(10) \omega^{-1} \right)$$
 (3.3)

The part within brackets represents the hydrogen content (N_H), where, ω is the wavenumber, d is the film thickness, A_{abs} is the area of gaussian measured around 560cm^{-1} , A is the proportionality constant whose value is assumed to be $1.3*10^{19} \text{cm}^{-2}$ as per literature [45] and is also in the same order as per other literature work [46].

The absorption coefficient of the GeO_x peaks is used to quantitatively express the GeO_x peak intensity. This is due to multiple gaussians being fitted in the range of $800\text{-}1050\text{cm}^{-1}$, with peak centres at 846cm^{-1} , 860cm^{-1} , 930cm^{-1} and 1000cm^{-1} that might correspond to different GeO_x bonding configurations. Therefore, determining a single proportionality constant for these various bonding configurations is rather arbitary. Hence, the absorption coefficient of the summed GeO_x peaks (α_{GeO_x}) is used as a thickness-independent factor for the sum of the relative GeO_x peak intensities.

Peak Wavenumber (cm ⁻¹)	Bonds	Stretching Mode	Source
400	GeH ₂	rocking B1	[47] [46]
440	Si-O		[48]
500	Ge-O-Ge	isolated group, bending, broad peak, occurs with O ₂ in chamber	[49]
560/(565)	Ge-H/Ge-H ₂	wagging/rolling B2	[50] [51] [52] [33]
610	Ge-C		[38] [53] [39] [40]
660	Ge_2O_2	surface oxidation of Ge	[54]
670	Ge-O-Ge-H	only for T_s < 225°C samples with O_2 source	[49]
760-765	GeO_x	oxidation of nanocrystalline germane surface	[33]
820	Ge-CH₃	rocking	[38] [55] [56]
820-830	GeO_x	bending, associated with unstable material	[57] [52]
950-1200	Si-O-Si	stretch	[58] [59]
1640	H ₂ O	bending	[33]
1870/1875	Ge-H	monohydride stretch	[60] [50] [61] [51] [62]
1975	Ge-H ₂	dihydride stretch, associated with unstable material	[50] [51] [62]
2025/2055	O ₂ GeH/O ₃ GeH	strecthing	[33]
2800-3000	C-H _x	C-H ₍₁₋₃₎ associated with unstable material	[62]

Table 3.2: FTIR peaks to their corresponding wavenumber for a-/nc-Ge:H

The table 3.2 lists the various possible FTIR peaks with their corresponding wavenumbers for an a-/nc-Ge:H material.

3.4.5. Photo-thermal Deflection Spectroscopy

The PDS is based on detecting the laser beam deflection in the periodically heated liquid Perfluorohexane Fluorinert FC-72 which is nontoxic and non-irritating to the eyes and skin. It is thermally and chemically stable, compatible with sensitive materials, nonflammable, and leaves essentially no residue upon evaporation. The thin film deposited on non-absorbing glass substrate immersed in nonabsorbing liquid (FC-72) is periodically illuminated by a monochromatic light that acts as the heating source. When the incident light is absorbed in the sample, the heat is transferred to the liquid inducing thermal waves that change the refractive index of the liquid and deflect the probe laser beam. The amplitude of the oscillation of the laser beam is detected by the position detector and lock-in amplifier referenced to the incident light frequency, and hence it is proportional to the amount of light absorbed in the sample. To normalize the measured PDS spectra we use a carbon nanotubes (CNT) layer deposited on glass substrate as a highly absorbing reference sample before performing the thin film sample measurements [10]. This technique is useful in determining the optical absorption close to and below the bandgap energy of the material, where other techniques such as the Spectroscopy Ellipsometry (SE) are not very sensitive. The PDS setup used by the PVMD group is schematically depicted in Figure 3.8, where K1-K5 are the positioning systems for the sample (S) and DT, DR, DB and DA are the detectors measuring the T-, R-, B- and A- spectra respectively.

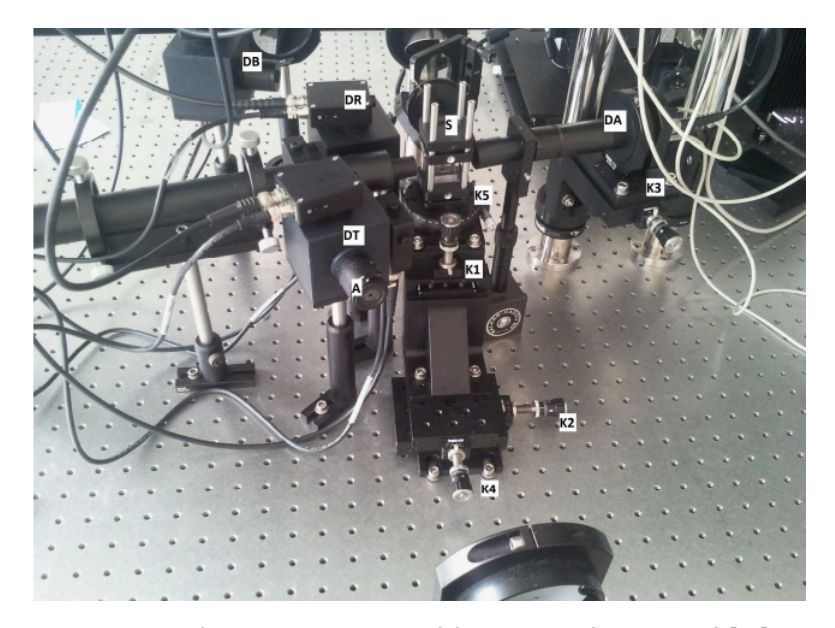


Figure 3.8: Schematic representation of the PDS setup (PVMD Group) [10]

3.4.6. J-V characteristics

The cell performance is characterized through the J-V measurements and it is used to obtain parameters such as the open circuit voltage (V_{oc}), short circuit current density (J_{sc}), shunt (R_s) and series resistance (R_{sh}), etc. for the solar cells. The measurement are carried out under 1 sun illumination and Standard Test Conditions (STC). The Standard Test Conditions (STC) denotes an AM1.5 spectrum at room temperature of 25°C under 1000 W/m² irradiance. In this thesis, a Wacom Solar Simulator is used for the purpose of performing J-V measurements, which comprises of a halogen and xenon lamp to compensate for the AM1.5 spectrum along with a cooling system attached to the stage so as to main room temperature of 25°C. This setup is calibrated using reference c-Si cells from Fraunhofer Institute of Solar energy Systems. A schematic representation of the J-V characteristics of a solar cell is shown in Figure 3.9.

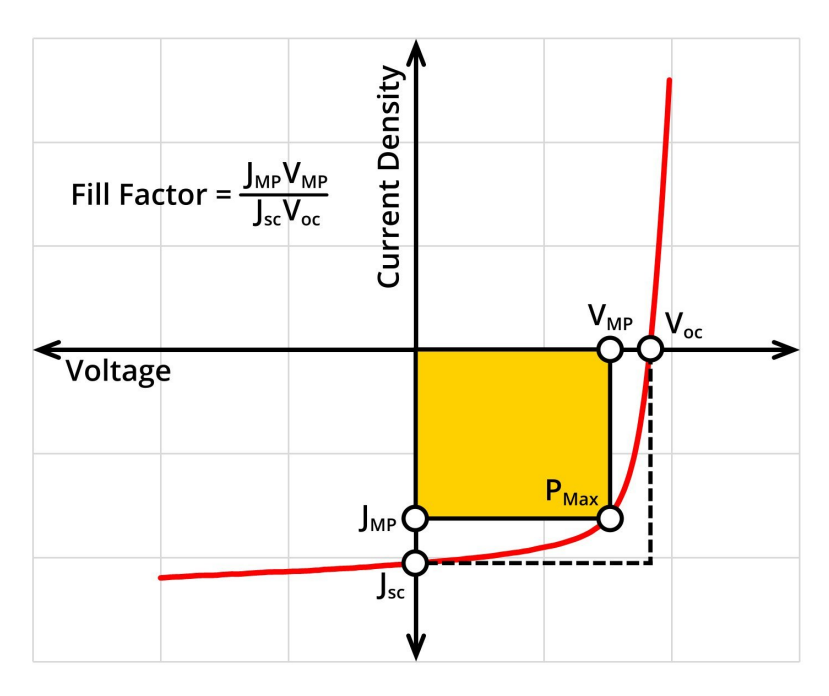


Figure 3.9: Schematic representation of an ideal J-V curve for a solar cell [11]

Processing Range for Successful Film Deposition

This chapter focuses on the different deposition pressure-power combinations used for processing the initial few Ge:H films. Subsequently, a processing window is found where successful film deposition is obtained. The first section 4.1 gives an insight into the initial choice of deposition parameters based on the information obtained from literature. In section 4.2, the type of deposition obtained for these initial set of pressure-power combinations are discussed and in section 4.3 the associated properties of the successfully deposited films are assessed.

4.1. Initial choice of deposition parameters

The various deposition parameters involved are the deposition pressure (mbar), RF Power (W), GeH_4 flow rate (sccm), H_2 flow rate (sccm), Deposition Temperature (°C) and Electrode Distance (mm). From the literature paper of Jiang et. al. [63], an insight into the deposition parameters used for the deposition of Ge:H films was obtained. Thereby, these set of parameters were chosen for the deposition of the initial few films and they are described in detail in the Table 4.1.

Deposition Parameter	Value/Range	Units
GeH ₄ flow rate	2	sccm
H ₂ flow rate	100	sccm
Deposition Temperature	200	°C
Deposition Time	10	minutes
Electrode Distance	20	mm
Deposition Pressure	0.5-1-1.5-2-3-5	mbar
RF Power	5-10-15-20-25-30-50	W

Table 4.1: Initial deposition parameters for obtaining Ge:H films

4.2. Assessment of the type of deposition

To map the type of deposition of the Ge:H layers using the conditions mentioned in the previous section 4.1, a system is introduced with three classifications:

- **No Deposition** Sub-optimal combination of various deposition parameters resulting in failure of plasma ignition.
- **Film Deposition** Optimal combination of various deposition parameters resulting in ignition of a stable plasma.
- **Dust Deposition** Sub-optimal combination of various deposition parameters resulting in dusty conditions within the chamber and hence dust deposited on the film substrate.

A successful film deposition can be visualized as a uniform layer of Ge:H due to the ignition of a stable plasma under clean chamber conditions. While the dust deposition can be visualized as a non-uniform layer with poor adhesion and particulates peeling off from the substrate that occurs due to dusty conditions present within the chamber.

Initially, the deposition pressure was set to 1 mbar and the RF power was varied from 5 W to 50 W. At these deposition conditions, a set of successful film depositions were obtained. Furthermore, the deposition pressure was varied at each RF power to obtain a range/window for processing. At relatively lower deposition pressures (< 1 mbar), the plasma could not be ignited for low RF powers. This could possibly be due to a combination of insufficient voltage being supplied to the electrode which does not induce an oscillating electric field that is required for plasma production and also the lack of sufficient number of gas molecules. Hence, there was no deposition obtained at these conditions. The pressure was then varied in steps of 2 mbar from the initial deposition pressure (1 mbar). At these deposition pressures, the relatively high power conditions (30 W-50 W) resulted in dusty conditions being produced within the chamber. As a result, these films were deposited with dust rather than having a successful film deposition. Furthermore, the deposition pressure was also varied in smaller steps of 0.5 mbar between 1 mbar and 3 mbar. This was done to investigate whether a set of successful film depositions can be obtained at each RF power for these pressures. However, for these pressures, dust was being deposited at relatively lower RF powers in comparison to the depositions made at higher pressures (3 mbar & 5 mbar). This could possibly be associated to the dusty conditions that were already present in the chamber from the previous depositions. The various pressure-power combinations and their respective deposition type is shown in Figure 4.1.

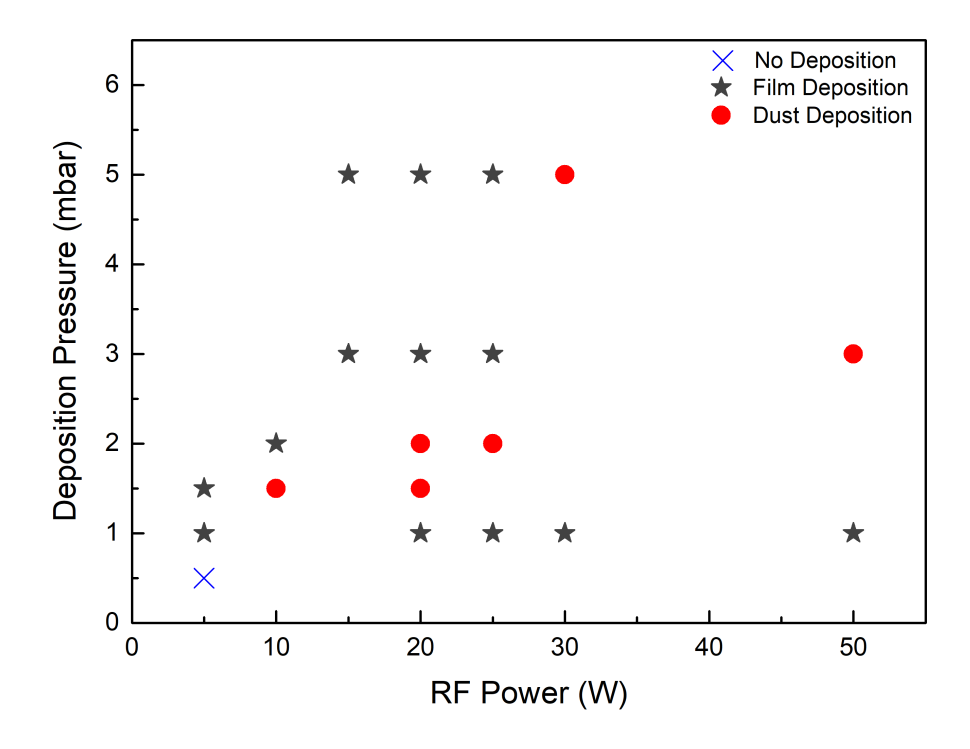


Figure 4.1: Type of deposition obtained for various pressure-power combinations

4.3. Properties of the successfully deposited films

The deposition rate of these initial films revealed that the deposition pressure is a critical parameter. It can be seen from Figure 4.2 that as the deposition pressure increases the deposition rate also tends to increase drastically, however a drop and an inconsistent variation in the deposition rate can be observed

when nearing the pressure-power combinations that result in the deposition of dust and this can be attributed to the dusty conditions beginning to occur within the chamber. The electrical parameters of these films such as the activation energy and the dark conductivity were investigated and are also plotted in Figure 4.2. It can be inferred that when the pressure is increased to values of 3 mbar and higher, there is a significant decrease in the activation energy. It can be speculated that this trend could be related to the increasing defect density in these films which have energy levels closer to the conduction band [64]. This is in line with the dark conductivity results which depict a similar trend of higher dark conductivities values for the films deposited at high pressures.

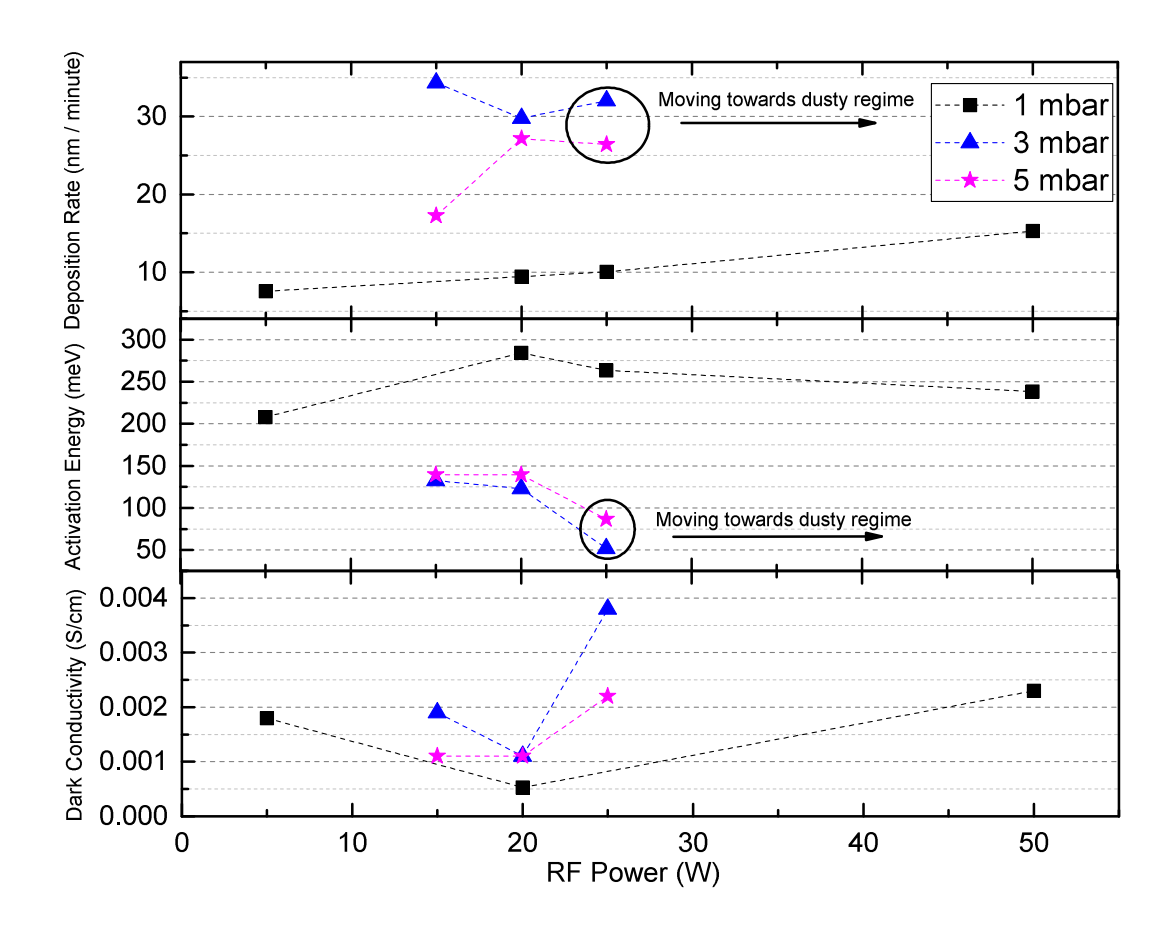


Figure 4.2: Deposition rate & Electrical parameters for various pressure-power combinations

Hence, it is evident that for the deposition conditions reported in Table 4.1, successful film deposition were obtained for the 1 mbar pressure region for varied RF powers and for the higher pressures (3 & 5 mbar) at RF powers lower than 30 W. Additionally, the films processed at 1 mbar pressure also showed high activation energies and low dark conductivities which can possibly attribute to a more intrinsic and less defective material being deposited in comparison to the films deposited at higher pressure regions.

Characterization of a-/nc-Ge:H films

This chapter focuses on the effect of varying different deposition parameters on the characteristics of individual Ge:H films. In the initial few sections (5.1 to 5.3) deposition parameters such as the $F(H_2)/F(GeH_4)$ dilution ratio, deposition pressure, RF power & deposition temperature are varied and the subsequent trends observed in the electrical, optical and material properties are discussed. In section 5.4 the effect of a post-deposition process such as the Hydrogen Post Treatment (HPT) on the film properties is described in detail. Furthermore, in section 5.5 the Photo-thermal Deflection Spectroscopy results are discussed briefly. The chapter concludes with section 5.6 where the overall results and trends are analysed.

5.1. Effect of varying $F(H_2)/F(GeH_4)$ dilution ratio

The results obtained in sections 4.2 and 4.3 were useful in determining the pressure-power combination for which the $F(H_2)/F(GeH_4)$ dilution ratio is varied. The $F(H_2)$ & $F(GeH_4)$ denote the flow rates (in sccm) of H_2 & GeH_4 , respectively. Since the 1 mbar pressure region for varied RF powers was found to be ideal with regards to various electrical properties, hence a low RF power (5 W) and a high RF power (20 W) at the aforementioned pressure were chosen. Apart from this, a few other pressure-power combinations, 4.5 mbar-15 W & 4 mbar-20 W, were also chosen to observe the effect of varying dilution ratio on various parameters. The $F(H_2)/F(GeH_4)$ dilution ratio was varied between 50 to 400 in steps of 50 for the lower pressure-power combinations (1 mbar-5 W & 1 mbar-20 W). Similarly, it was varied between 200 to 400 in steps of 50 for the higher pressure-power combinations (4.5 mbar-15 W & 4 mbar-20 W). Table 5.1 represents the various deposition parameters that were involved while varying the dilution ratio.

Deposition Parameter	Value/Range	Units
Deposition Pressure	1,4,4.5	mbar
RF Power	5,15,20	W
Deposition Temperature	200	°C
Electrode Distance	20	mm
Deposition Time	adjusted to obtain thickness of 100 nm	minutes
F(H ₂)/F(GeH ₄) dilution ratio	50-100-150-200-250-300-350-400	-
H_2 flow rate (F(H_2))	100,125,150,175,200	sccm
GeH ₄ flow rate (F(GeH ₄))	0.5,1,2	sccm

Table 5.1: Deposition parameters for varying $F(H_2)/F(GeH_4)$ dilution ratio

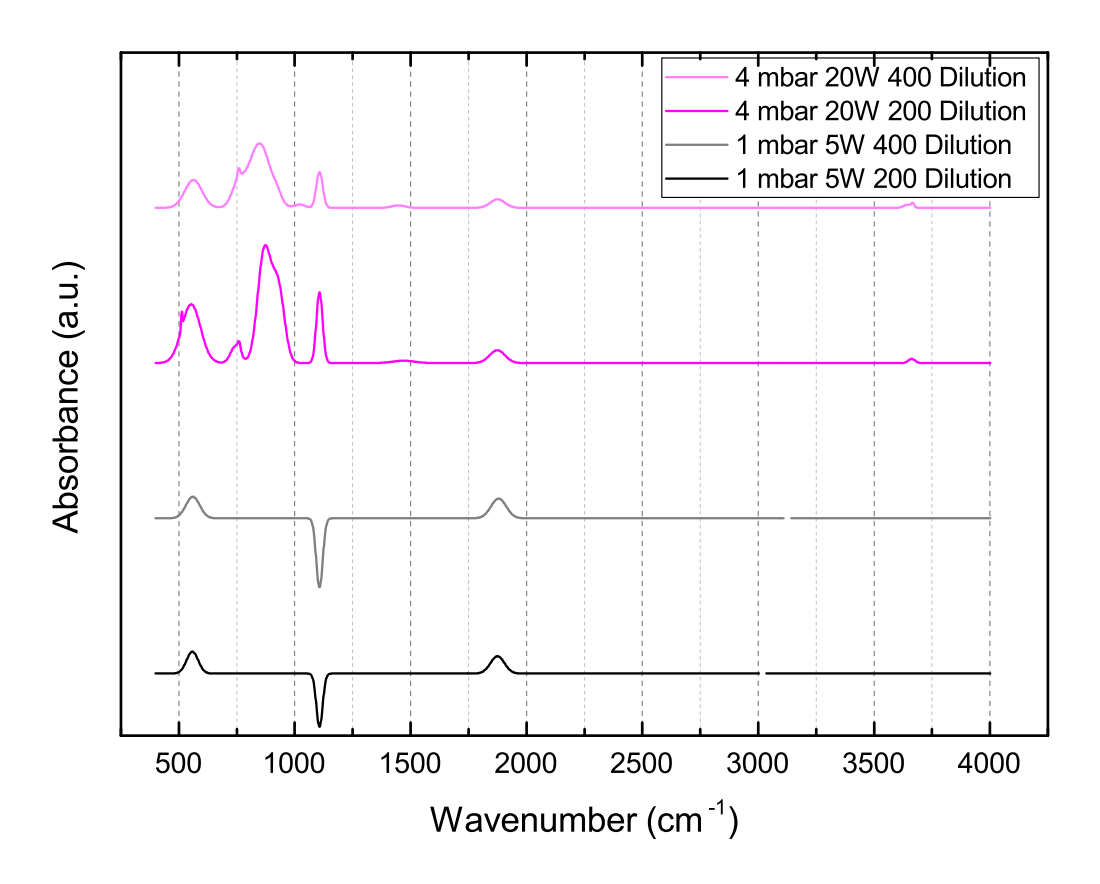


Figure 5.1: Fitted FTIR Spectrum for films with varying F(H₂)/F(GeH₄) dilution ratio

The fitted FTIR spectrum of a few selected films with the increase in F(H₂)/F(GeH₄) dilution ratio is depicted in Figure 5.1. It can be observed that the films deposited at 1 mbar-5 W do not show any peaks in the range of 830-1000cm⁻¹ that correspond to various oxides of Ge (GeO_{τ}) as per Table 3.2. The wagging mode peak of Ge-H at 560cm^{-1} remains fairly constant with the increase in $F(H_2)/F(GeH_4)$ dilution ratio from 200 to 400. As discussed in section 3.4.4, the hydrogen concentration (C_H) in the film is evaluated using the area under this peak by using the equation 3.3. The peak at 1875cm⁻¹ depicts the Ge-H stretching mode peak, which remains fairly constant too. On the other hand, the films deposited at 4 mbar-20 W show significantly higher GeO_x peaks in the 830-1000cm⁻¹ range. The position and the intensity of these peaks shift significantly with increasing F(H₂)/F(GeH₄) dilution ratio. These films also depict a relatively small peak around 1640cm⁻¹, that denote the presence of H_2O molecule (as per Table 3.2). Additionally, these films also show higher hydrogen concentration (C_H) in comparison to the films deposited at 1 mbar-5 W, visualized by the larger 560cm⁻¹ Ge-H wagging mode peak. However, due to the heavy oxygen contamination, the properties of these films are predominantly determined by it rather than the hydrogen and its passivation of these films. The GeO_x peaks in the range of $850\text{-}1000\text{cm}^{-1}$ can be quantitatively expressed by the thickness-independent absorption coefficient (α_{GeO_x}) factor which is described in section 3.4.4 as well.

The absorption coefficient (α_{GeO_x}) of the films that roughly characterize the oxygen contamination in the films as a function of varying $F(H_2)/F(GeH_4)$ dilution ratio is depicted in Figure 5.2. The parameter α_{GeO_x} remains at zero for the lower pressure films and it can be attributed to denser films being deposited at these pressures with increasing $F(H_2)/F(GeH_4)$ dilution ratio. This is in line with the increase in the refractive index of these films with respect to the $F(H_2)/F(GeH_4)$ dilution ratio. The refractive index at wavelength of 600nm as a function of the $F(H_2)/F(GeH_4)$ dilution ratio is plotted in Figure 5.3. The deposition of such denser films at these low pressure conditions can be attributed a combination of factors such as increased etching by hydrogen atoms, low Ge-radicals availability and

low energetic ion bombardment. However, for the high pressure films, the parameter α_{GeO_X} is quite high denoting high oxygen contamination. This can attributed to the relatively high porosity in these films denoted by their lower refractive index.

The hydrogen concentration (C_H) in the films as a function of varying $F(H_2)/F(GeH_4)$ dilution ratio is also depicted in Figure 5.2. They initially decrease until the $F(H_2)/F(GeH_4)$ dilution ratio reaches high values. At the higher $F(H_2)/F(GeH_4)$ dilution ratio values, they show no clear trend. This can possibly be attributed to the change in the absolute flow rate values of H_2 and GeH_4 . The literature paper by Lucovsky et. al. [49] and Schroder et. al. [65], prove that unlike a-Si, the oxygen contamination and hydrogen concentration (C_H) are competitive in the Ge films.

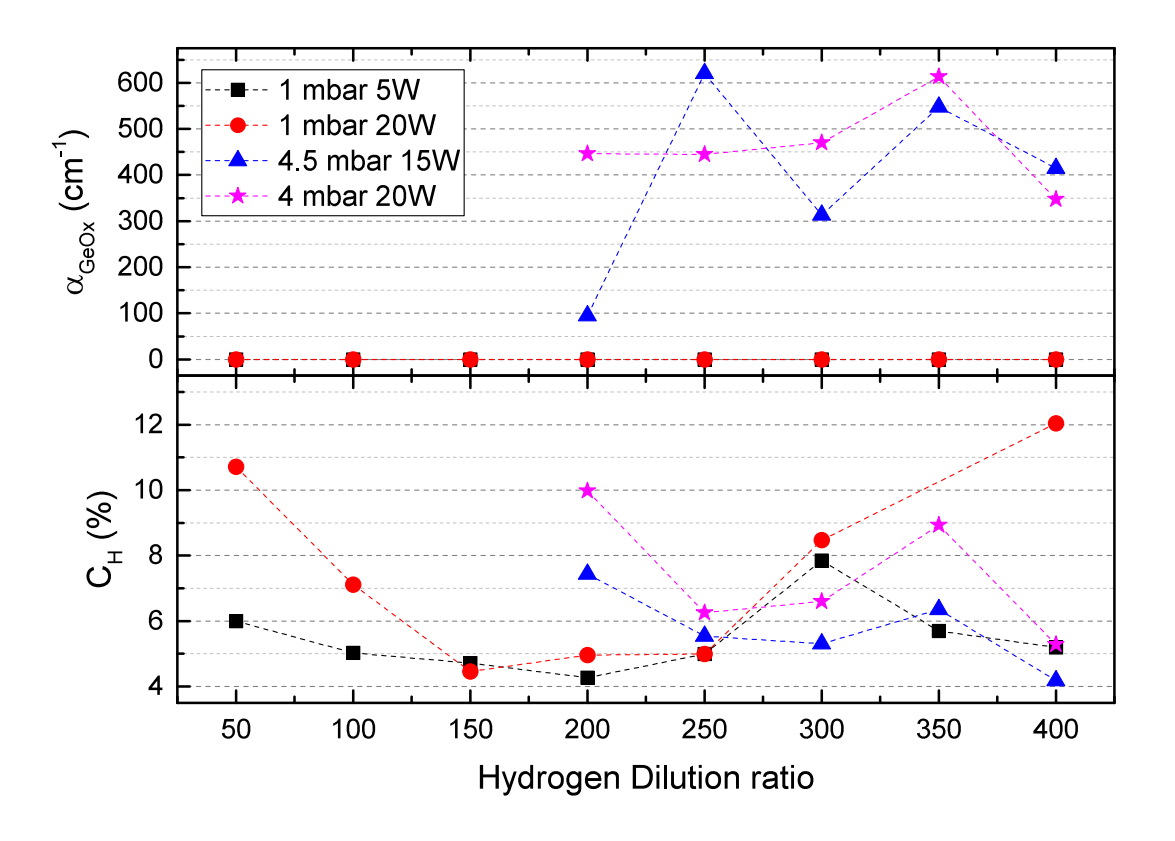


Figure 5.2: Effect of varying $F(H_2)/F(GeH_4)$ dilution ratio on the α_{GeO_x} & the hydrogen concentration (C_H)

Figure 5.3 depicts the variation in the E_{04} optical bandgap with the $F(H_2)/F(GeH_4)$ dilution ratio. It can be observed that with the increase in the $F(H_2)/F(GeH_4)$ dilution ratio, the E_{04} optical bandgap increases. This trend can possibly be attributed to the increased sub-bandgap absorption due to the increased defect density in the low pressure films with the increase in $F(H_2)/F(GeH_4)$ dilution ratio. This hypothesis can be supported by the fact that a decrease is observed in the hydrogen concentration (C_H) with increasing $F(H_2)/F(GeH_4)$ dilution ratio thereby causing more unpassivated Ge dangling bonds in these films. For the high pressure films, the above reasoning can be given for the increasing E_{04} trend but since these films show significant oxygen contamination due to their lower refractive index, it might possibly result in the passivation of the defects. If so, it might result in a reduced sub-bandgap absorption and a consequent decrease in the E_{04} optical bandgap. However, the E_{04} optical bandgap is seen to be increasing in these high pressure films as well. Therefore, it could possibly be due to effect of void-density and oxidation on the bandgap/mobility gap outweighing the effect of the defect passivation by the oxygen. Similar trends are also observed in the E_{03} optical bandgap as a function of $F(H_2)/F(GeH_4)$ dilution ratio and it is depicted in Figure A.1.

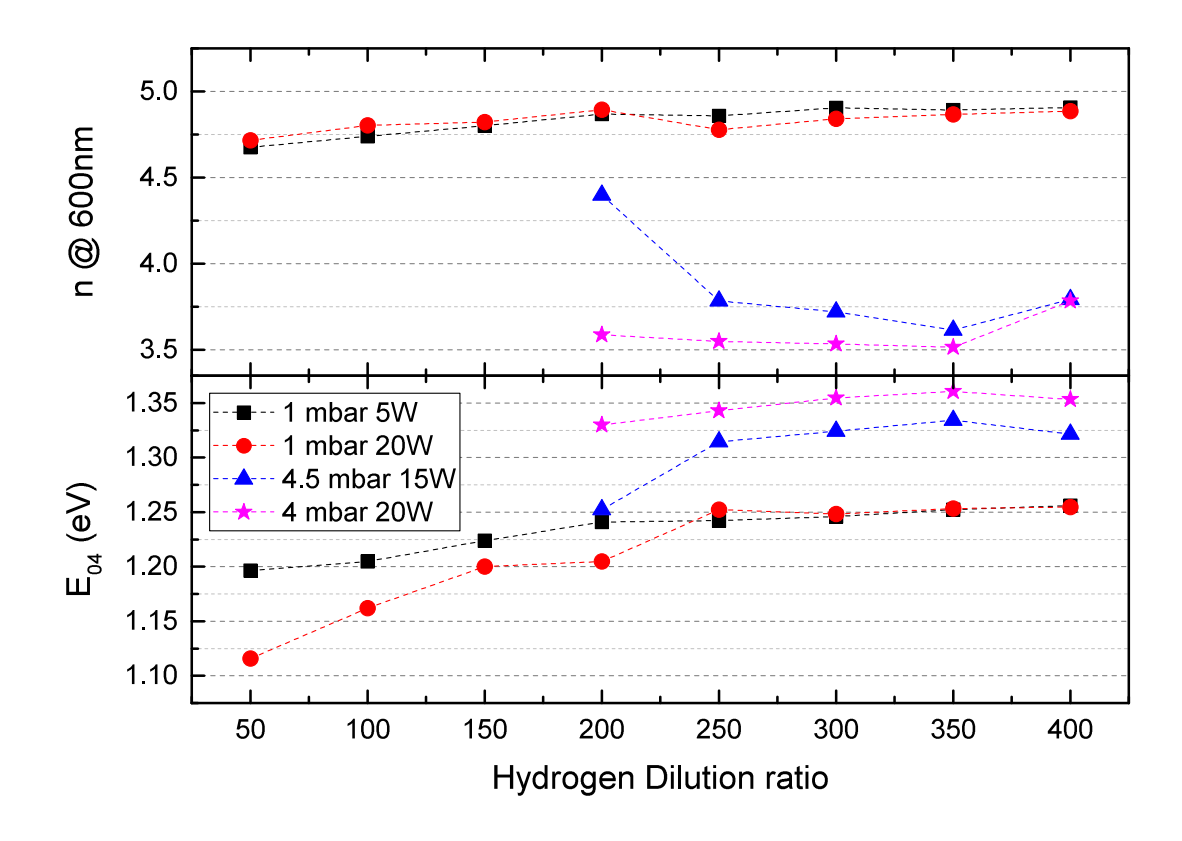


Figure 5.3: Effect of varying $F(H_2)/F(GeH_4)$ dilution ratio on the n @ 600nm & the E_{04} optical bandgap

Figure 5.4 depicts the variation of the dark conductivity with respect to the $F(H_2)/F(GeH_4)$ dilution ratio. It can be observed that the dark conductivity of the low pressure films increases with the increasing $F(H_2)/F(GeH_4)$ dilution ratio. This can be associated to the activation energy results also depicted in Figure 5.4. As discussed earlier, due to the decrease in hydrogen concentration (C_H) with increasing F(H₂)/F(GeH₄) dilution ratio, the unpassivated Ge dangling bonds could increase. Since these dangling bonds have defect energy levels closer to the conduction band [64], these low pressure films become more n-type with increasing $F(H_2)/F(GeH_4)$ dilution ratio. This is in line with the marginal decrease in the activation energy in these low pressure films with increasing $F(H_2)/F(GeH_4)$ dilution ratio and hence the increase in the dark conductivity can be verified. On the other hand, the dark conductivity of the high pressure films remains fairly constant with increasing F(H₂)/F(GeH₄) dilution ratio and is much lower than the dark conductivity values of the low pressure films. This is quite unexpected considering the fact that these high pressure films show high oxygen contamination and subsequently lower activation energy values, which should ideally result in a higher dark conductivity than the low pressure films. However, this is not the case as observed in the dark conductivity result. The possible explanation to this trend consists of two steps. Firstly, the passivation of the defects by the oxygen and a subsequent reduction in σ_o , and secondly, the effect of reduced σ_o outweighing the effect of reduction in activation energy due to the oxygen contamination. The relationship of σ_{α} , known as the pre-exponential factor, with the dark conductivity and the activation energy is represented in equation 2.14. The photo/dark conductivity results are depicted in Figure 5.4 as well. It can be directly related to the oxygen contamination in the films. For the low pressure films that do not show any oxygen contamination, the photo-conductivity values are higher than that of the high pressure films which show significant oxygen contamination. Despite this result, the photo/dark conductivity values is higher for the oxygen contaminated films at high pressures than the low pressure films without any oxygen contamination. Therefore, it can be concluded that this trend is associated to the greater impact of the decrease in σ_o and the dark conductivity upon oxygen contamination than the trend in the photo-conductivity with respect to the oxygen contamination.

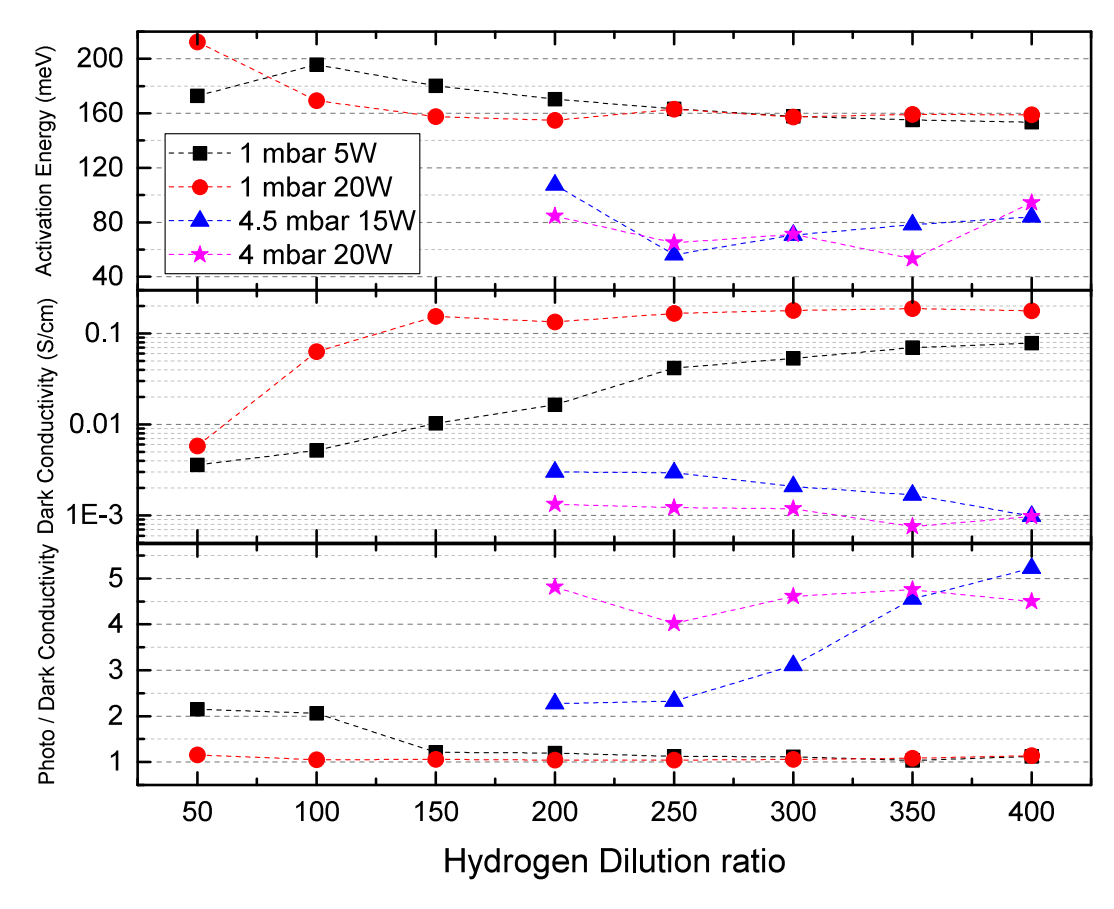


Figure 5.4: Effect of varying $F(H_2)/F(GeH_4)$ dilution ratio on the Activation Energy (E_{act}) , Dark Conductivity & the Photo/Dark conductivity ratio

The Raman Spectroscopy results of the films at dilution ratios of 200 and 400 are depicted below in Figures 5.5 and 5.6, respectively. The crystalline fraction as a function of varying $F(H_2)/F(GeH_4)$ dilution ratio is shown in Figure 5.7. It is calculated using equation 2.15 from the Raman Spectroscopy results for the low and high pressure films.

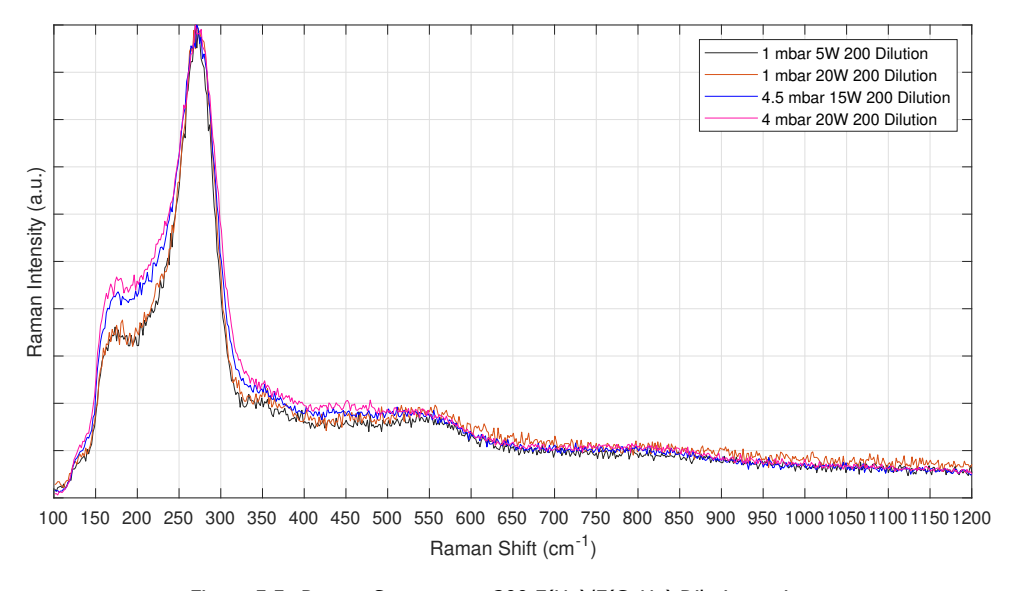


Figure 5.5: Raman Spectrum at 200 $F(H_2)/F(GeH_4)$ Dilution ratio

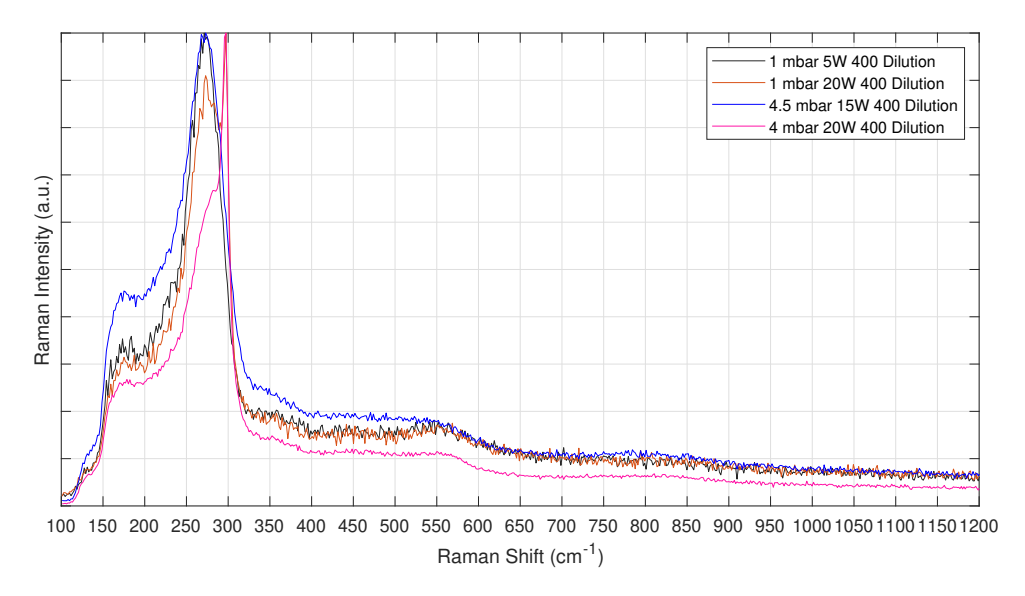


Figure 5.6: Raman Spectrum at 400 F(H₂)/F(GeH₄) Dilution ratio

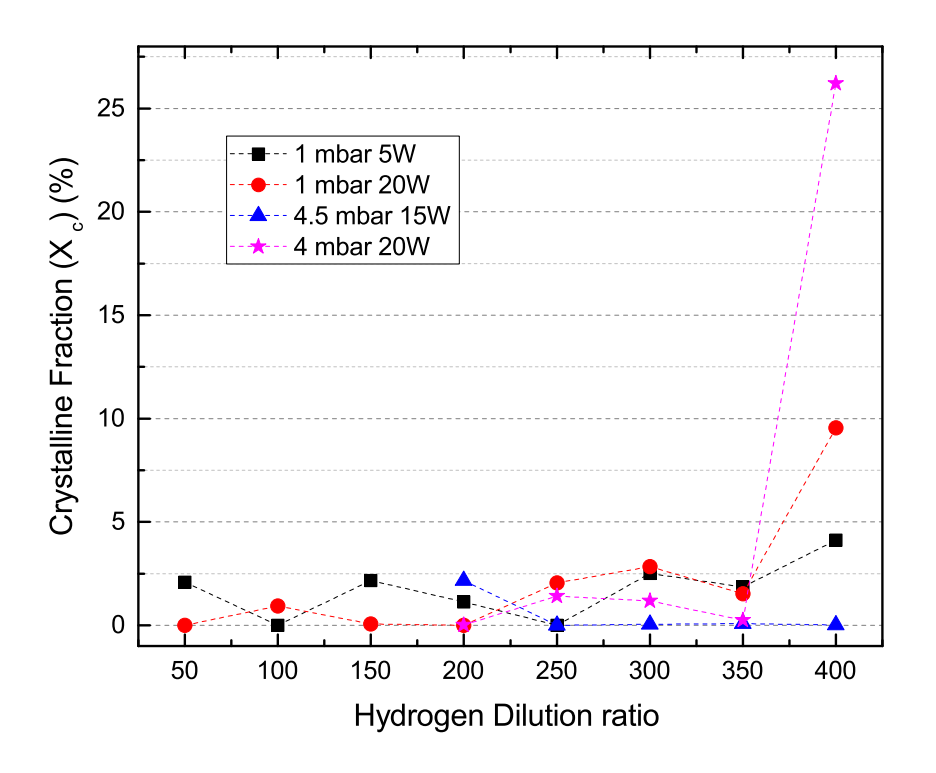


Figure 5.7: Crystalline Fraction (X_c) vs $F(H_2)/F(GeH_4)$ dilution ratio

From Figure 5.5, it is quite clear that at dilution ratios lower than 400 none of the films show nano-crystalline behaviour. The films at dilution ratio of 200, show two amorphous peaks at 177cm⁻¹ (Longitudinal Acoustic (LA) phonon mode) and at 278cm⁻¹ (Transverse Optic (TO) phonon mode of a-Ge), as per Table 3.1. The LA peak with respect to the TO peak, is noticeably bigger for the higher pressure films. The underlying cause to this trend is unknown. From Figure 5.6, it can be observed that at the highest dilution ratio of 400, only the films processed at 20 W RF power show a crystalline

peak at around 300cm⁻¹ as per Table 3.1. Another interesting aspect is that the 1 mbar-20 W sample at 400 dilution ratio proves useful to observe the transition from a amorphous structure into a nanocrystalline structure as it depicts both the 278cm⁻¹ peak (Transverse Optic phonon mode of a-Ge) and the 300cm⁻¹ peak. From the results of the crystalline fraction, it is quite clear that only at the highest dilution ratio of 400, the crystalline fraction present in the material reaches considerable values.

5.2. Effect of varying Pressure-Power

The results obtained in the previous section 5.1 were useful in determining the range of variation in the pressure-power combinations so as to study their effects on the various properties of the films grown. Since the lower pressure films showed a high refractive index while the higher pressure films showed significant photo/dark conductivity ratio (albeit due to oxygen contamination) at the highest dilution ratio of 400, hence the $\rm H_2/GeH_4$ dilution ratio is fixed at 400. The pressure is then varied in steps of 1 mbar for the RF powers of 5 W and 20 W, and also other RF powers are chosen such as 10 W, 15 W and the 25 W to obtain a more broad operating range. The pressure is varied in smaller steps of 0.5 mbar for the higher RF powers (>15 W) to closely observe the region of transition from a-Ge to nc-Ge in the films grown. Table 5.2 represents the various deposition parameters that were involved while varying the pressure-power combinations.

Deposition Parameter	Value/Range	Units
Deposition Pressure	1,2,3,3.5,4,4.5	mbar
RF Power	5,10,15,20,25	W
Deposition Temperature	200	°C
Electrode Distance	20	mm
Deposition Time	adjusted to obtain thickness of 100 nm	minutes
H ₂ /GeH ₄ dilution ratio	400	-
H ₂ flow rate	200	sccm
GeH ₄ flow rate	0.5	sccm

Table 5.2: Deposition parameters for varying pressure-power

The two important parameters obtained from the fitted FTIR spectrum are the absorption coefficient of GeO_x (α_{GeO_x}) and the hydrogen concentration in the film (C_H) as seen in the previous section. The thickness-independent absorption coefficient (α_{GeO_x}) factor is obtained from the GeO_x peaks in the range of 850-1000cm⁻¹ as described earlier. Similarly, the hydrogen concentration in the films is obtained using the area under the wagging mode peak at 560cm⁻¹. The fitted FTIR spectrum of specific films with varying pressure is depicted in Figure A.3.

The oxygen contamination in the films characterized by the parameter α_{GeO_x} as a function of increasing pressure-power is depicted in Figure 5.8. The absence of oxidation in the low RF power films is directly linked to the relatively high refractive index of these films which remains fairly constant with increasing pressure, thereby denoting less porosity. On the other hand, the significant oxygen contamination for the films deposited at higher RF powers (>5 W), especially at pressures of 3 mbar and higher can be verified by the sharp decrease in the refractive index for these films that occurs around the same pressure region denoting the deposition of much porous films. The refractive index at wavelength of 600nm as a function of pressure-power is depicted in Figure 5.9. This drastic drop in the refractive index for pressures above 2 mbar coincides with the films showing a crystalline phase. This can be observed in the Raman Spectroscopy results later in this section. Another interesting observation is that most of the other parameters discussed in this section begin to vary drastically from this high pressure region (>2 mbar) for these higher RF power (>5 W) films. The hydrogen concentration in the films as a function of increasing pressure-power is also depicted in Figure 5.8. There is no clear trend observed in the hydrogen concentration for each combination of pressure-power.

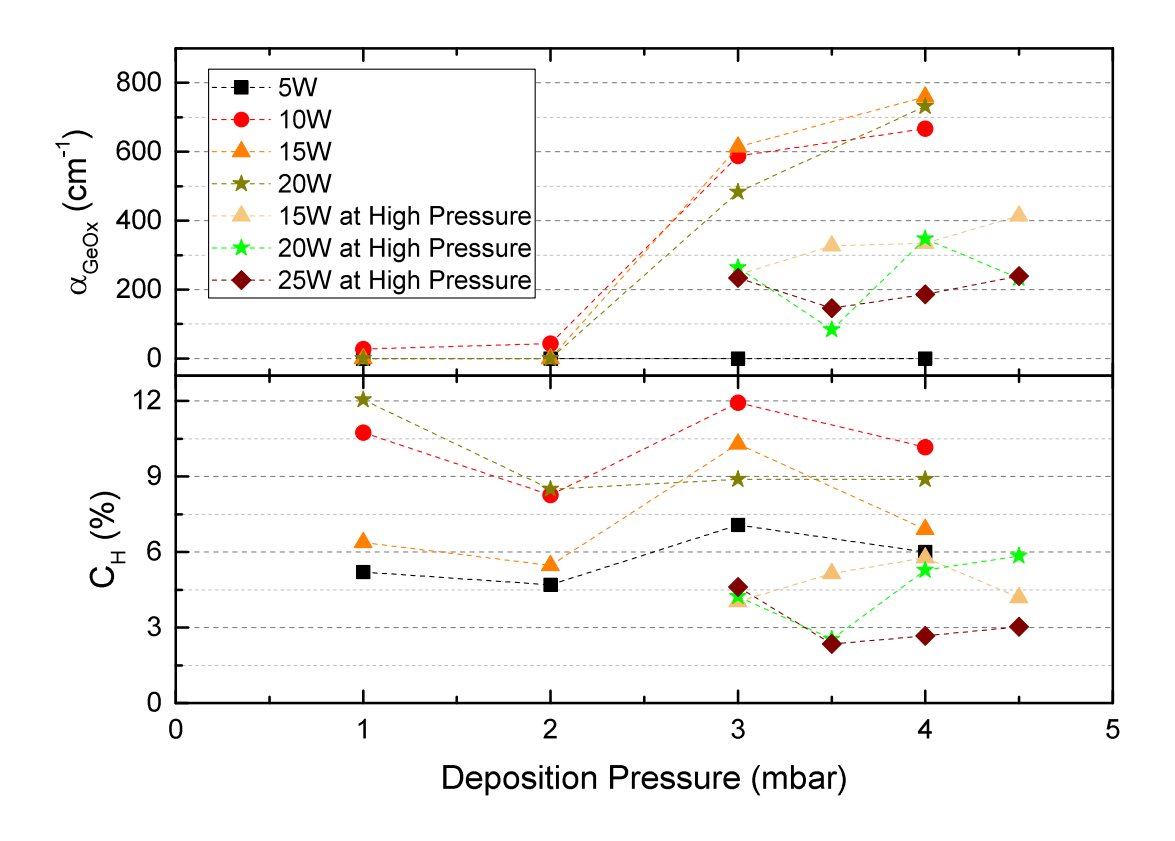


Figure 5.8: Effect of varying pressure-power on the $\alpha_{{\it GeO}_x}$ & the hydrogen concentration (C_H)

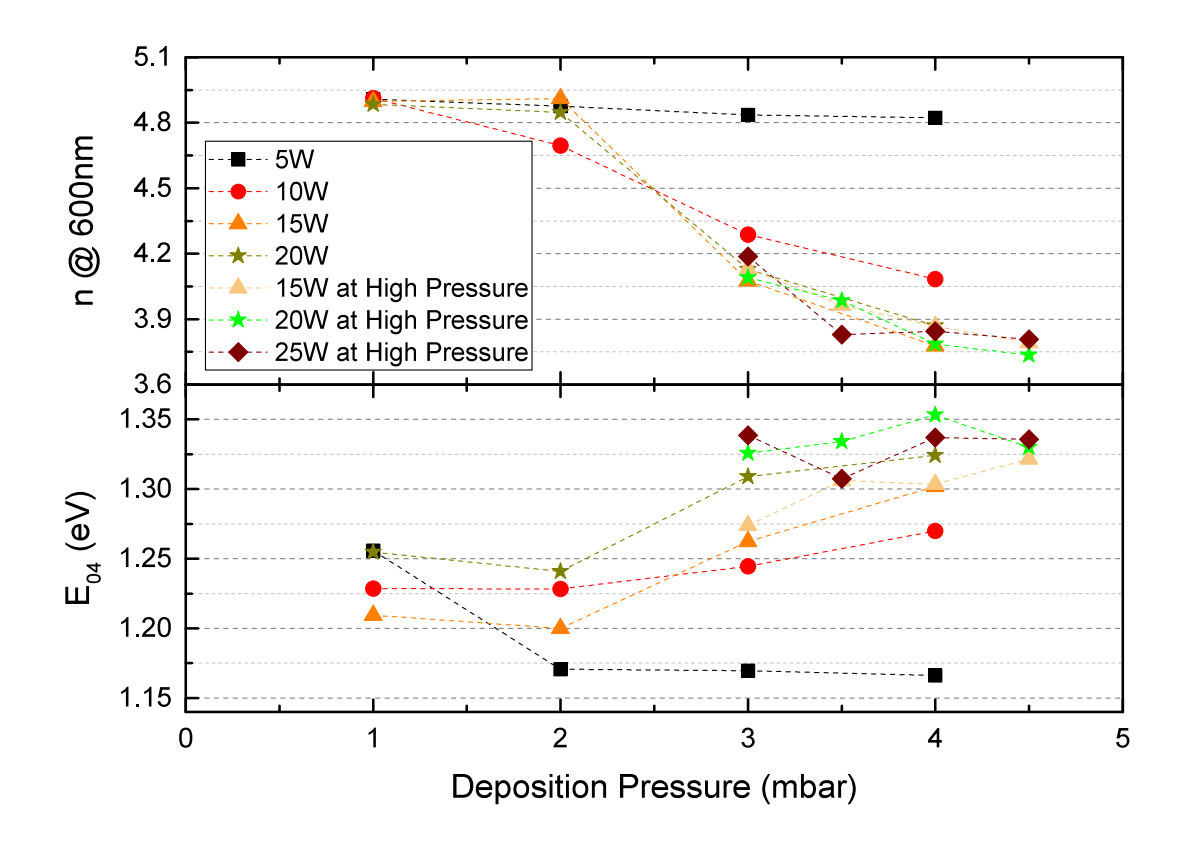


Figure 5.9: Effect of varying pressure-power on the n @ 600nm & the $\rm E_{04}$ optical bandgap

The E_{04} optical bandgap as a function of varying pressure for various RF powers is depicted in Figure 5.9 as well. It can be seen that only for the films with the lowest RF power (5 W), the E_{04} optical bandgap decreases initially and then remains fairly constant with increasing pressure. This trend denotes a linear relationship with the hydrogen concentration (C_H) and the relatively high refractive index which remains fairly constant with increasing pressure due to which there is no oxygen contamination. However, in the case of the films deposited at larger RF powers (>5 W) the trend observed is different. Initially, they show a relatively small decrease in the E_{04} optical bandgap denoting a linear relationship with the hydrogen concentration (C_H) and refractive index at lower pressures (1-2 mbar) when there is no oxygen contamination and then show an increase in the E_{04} optical bandgap at higher pressures (>2 mbar). Therefore, this increase can possibly be due to the same reasoning mentioned in the previous section regarding the oxygen passivation effect being outweighed by the effect of void-density and oxidation on the bandgap/mobility-gap. This is also in line with the drastic drop observed in the refractive index at pressures of 2 mbar and above which denotes a more porous material being processed. A similar trend for both the low (5 W) and high RF power (>5 W) films can be observed for the E_{03} optical bandgap as well. This is depicted in Figure A.4.

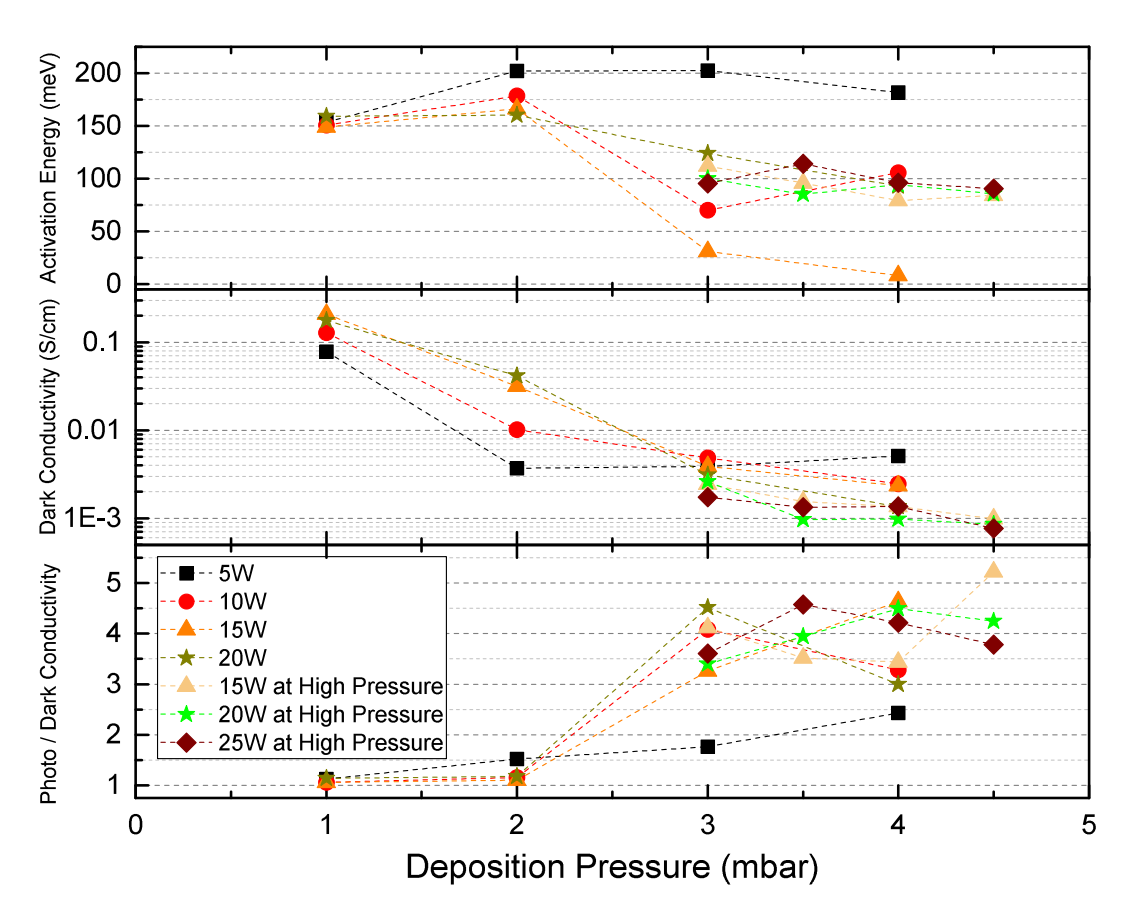


Figure 5.10: Effect of varying pressure-power on the Activation Energy (E_{act}), Dark Conductivity & the Photo/Dark Conductivity ratio

The dark conductivity of the films as a function of pressure-power is depicted in Figure 5.10. It can be observed that the films deposited at a low RF power (5 W) have a lower dark conductivity than the films higher RF powers (>5 W) until the pressure exceeds 3 mbar. This could possibly be associated to the higher activation energy values along with the higher refractive index which remains fairly constant denoting a denser material with the absence of oxygen contamination. The activation energy results as a function of pressure-power is also depicted in Figure 5.10. As discussed earlier, the films deposited at higher RF powers (>5 W), show substantial oxygen contamination due to their increasing porosity with the increase in pressure. The increasing porosity facilitates the significant oxygen contamination which could result in the films becoming more n-type with increasing pressure as verified by the literature

paper by M. Moreno et. al. [66]. This is in line with the drastic decrease in the activation energies of these high power films with increasing pressure. However, the dark conductivity results for these films is guite unexpected as it decreases with the increasing pressure. This trend can be supported by the same reasoning as explained in the previous section with regards to the oxygen contamination and its effect on defect passivation, σ_0 compared to the activation energy. The extent of impact that the oxygen contamination has on the decrease in σ_o and subsequently on the dark conductivity can be observed by the decrease in the dark conductivity values of the high power films below that of the low power films at high pressures (> 3 mbar). The Photo/Dark conductivity results as a function of pressure-power is depicted in Figure 5.10 as well. It can be observed that for the films deposited at low RF power (5 W), the photo/dark conductivity values, although quite low, shows a gradual increase with pressure. This is guite promising considering the fact that the associated dark conductivity values shows an initial decrease and then remain fairly constant with increasing pressure along with a high refractive index without any oxygen contamination as seen earlier. The photo/dark conductivity values are much higher for the films deposited at higher RF powers (>5 W). As seen in the previous section, the effect of oxygen contamination on σ_a and dark conductivity primarily contribute to such photo/dark conductivity values rather than the photo-conductivity in itself. Hence, high photo/dark conductivity values are obtained for these high power films at higher pressures (> 2 mbar). Another interesting aspect is the crystallinity having a significant impact on the photo/dark conductivity values in these high pressure-power films. The coincidence between the high crystallinity and large photo/dark conductivity can be verified by the Raman Spectroscopy results later in this section.

The Raman Spectrum of the low RF power (5 W and 10 W) and the high RF power (15 W, 20 W & 25 W) films at different pressures is shown in Figure 5.11 and Figure 5.12, respectively. From Figure 5.11, it can be deduced that for RF powers upto 15 W, the films do not show nano-crystalline nature with the increase in pressure. This can be visualized by the amorphous peaks at 177cm⁻¹ that denotes the Longitudinal Acoustic (LA) phonon mode of a-Ge and at 278cm⁻¹ that denotes the Transverse Optic (TO) phonon mode as mentioned in Table 3.1. It is interesting to observe the change in the LA peak with respect to the TO peak of a-Ge with pressure. Therefore, there is a clear increasing trend observed but the underlying cause is not well understood.

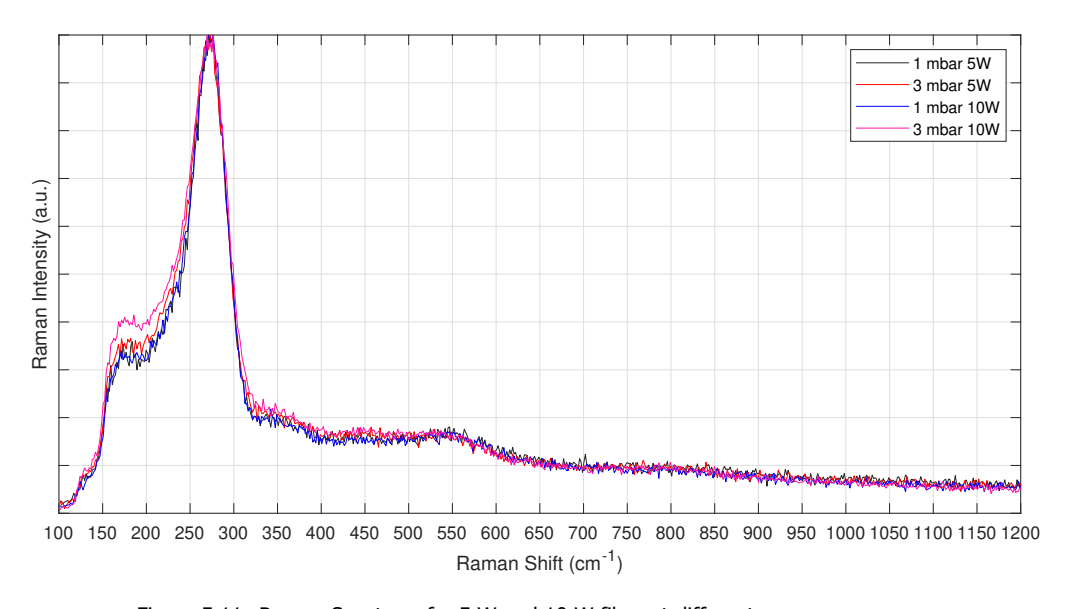


Figure 5.11: Raman Spectrum for 5 W and 10 W films at different pressures

From Figure 5.12, it can be observed that the films at 15 W tend to show amorphous nature with the increase in pressure much like the films at lower RF powers (5 W and 10 W). However, for the films deposited at RF powers of 20 W and above, nano-crystalline nature can be observed through the peak at 300cm^{-1} . At low pressure of 1 mbar the film shows the transition from amorphous to nano-crystalline structure by depicting peaks at both 278cm^{-1} and 300cm^{-1} . As the pressure is increased further, the LA

& TO amorphous peaks at 177cm⁻¹ & 278cm⁻¹, respectively, disappears and only the nano-crystalline peak at 300cm⁻¹ remain. Furthermore, as the RF power is increased to 25 W, the films become more nano-crystalline in nature. The crystalline fraction as a function of varying pressure-power is depicted in Figure 5.13. It is calculated using the Equation 2.15 from the Raman Spectroscopy results. It can be observed that it is significantly high for films processed at pressures of 3 mbar and higher & for powers higher than 15 W.

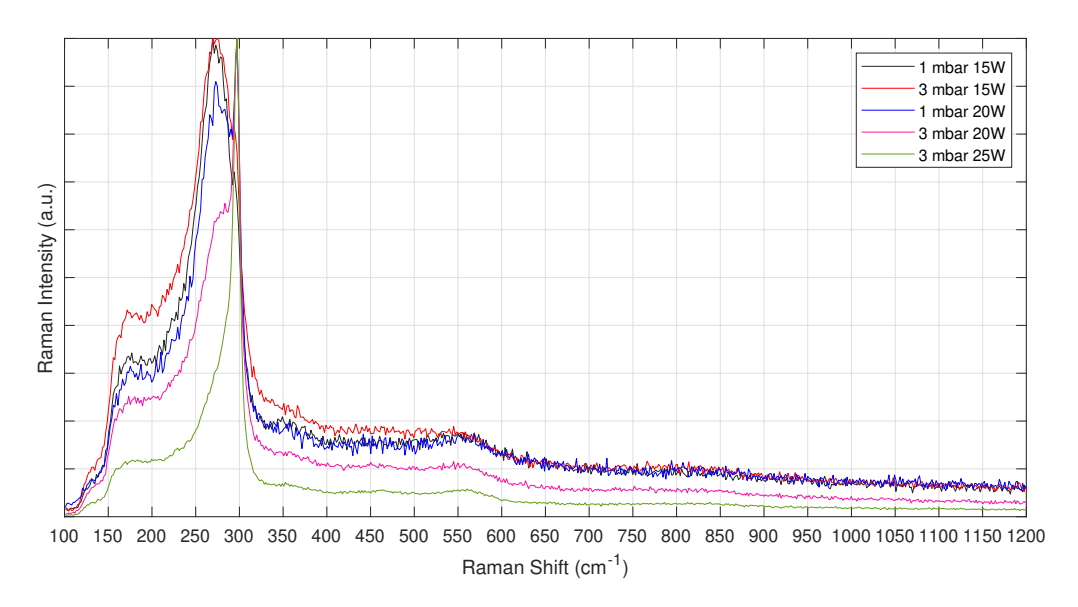


Figure 5.12: Raman Spectrum at 15 W, 20 W & 25 W films at different pressures

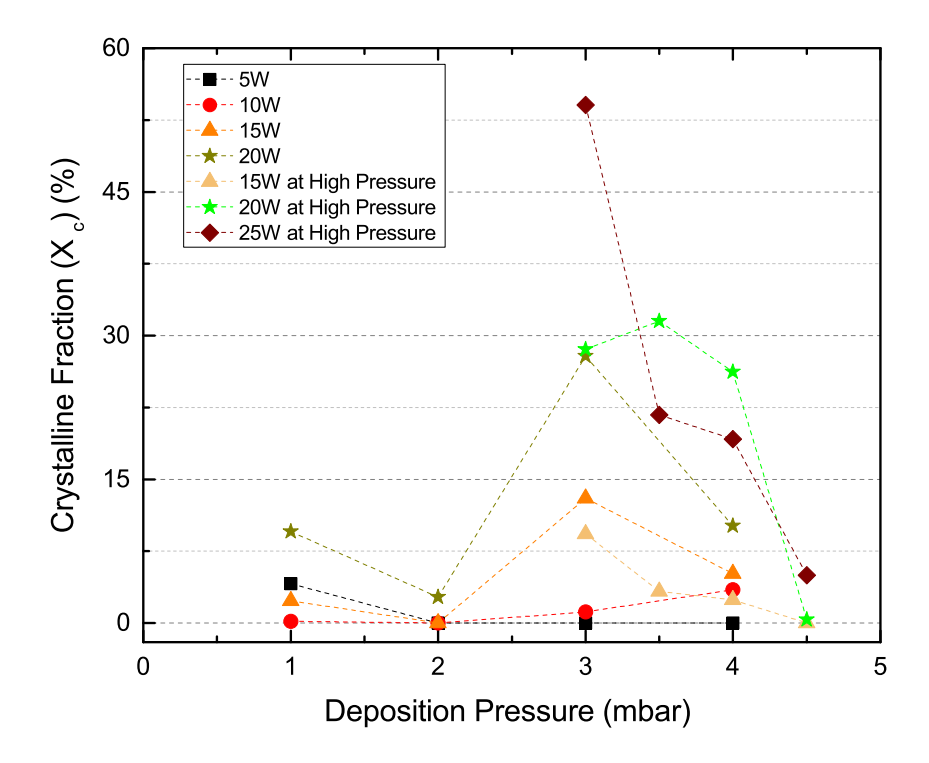


Figure 5.13: Crystalline Fraction (X_c) vs Pressure-Power

5.3. Effect of varying Deposition Temperature

The results of the Raman spectroscopy and the photo/dark conductivity ratio obtained in the section 5.2 were useful in determining the films for which the effect of variation of the deposition temperature on different properties were to be studied. Therefore, one film of nc-Ge:H (3.5 mbar-25 W) and a-Ge:H (4.5 mbar-15 W) each that showed high photo/dark conductivity ratio were chosen. Table 5.3 represents the various deposition parameters that were involved while varying the deposition temperature.

Deposition Parameter	Value/Range	Units
Pressure-Power	3.5-25,4.5-15	mbar-W
Deposition Temperature	150-200-250-300-350	°C
Electrode Distance	20	mm
Deposition Time	adjusted to obtain thickness of 100 nm	minutes
H ₂ /GeH ₄ dilution ratio	350,400	-
H ₂ flow rate	175,200	sccm
GeH₄ flow rate	0.5	sccm

Table 5.3: Deposition parameters for varying deposition temperature

The fitted FTIR spectrum of specific films with varying deposition temperature is depicted in Figure A.6. As discussed in previous sections, the relevant parameters from the FTIR spectrum such as the α_{GeO_x} and the hydrogen concentration (C_H) in the films are obtained by using the area under the peaks in the 850-1000cm⁻¹ range and the Ge wagging mode peak at 560cm⁻¹.

Figure 5.14 depicts the absorption coefficient (α_{GeO_X}) that roughly characterizes the oxygen contamination that is present in the films as a function of varying deposition temperature. The common trend between both sets of films is that the films deposited at lower temperatures ($\leq 250^{\circ}$ C for 4.5 mbar-15 W & $\leq 300^{\circ}$ C for 3.5 mbar-25 W) show mild oxygen contamination. This can possibly be attributed to the decreasing hydrogen concentration (C_H) in the films with increasing deposition temperature which can result in an increase in the unpassivated dangling bonds. Therefore, it is possible that these unpassivated dangling bonds could easily react with atmospheric oxygen. The films deposited at higher temperatures ($>250^{\circ}$ C for 4.5 mbar-15 W & $>300^{\circ}$ C for 3.5 mbar-25 W) show very less or no oxidation despite a further decrease in the hydrogen concentration (C_H) in the films. This can be associated to the fact that denser films are produced at higher deposition temperatures due to a possible reduction of voids in the films from a certain threshold temperature as per the literature paper by Eberhardt et. al. [61]. This is in line with the increase in the refractive index of the films with increasing deposition temperature. The hydrogen concentration and refractive index at a wavelength of 600nm for both the films as a function of deposition temperature are shown in Figure 5.14 and 5.15, respectively.

The underlying mechanism to the reduction of voids from the threshold temperature in these films is believed to be based on the surface diffusion as reported in multiple literature work for a-Si [67], [68]. In section 5.6, the reason behind the large flux and low surface diffusion of the Ge-radicals on the growing surface and the subsequent formation of large void density is explained. A certain activation energy is required for the Ge-radicals on the growing surface to reach and fill a site that could result in a void. Therefore, it is possible that at certain threshold temperature, small voids are being filled. Therefore, a dense film is obtained that is resistant to oxygen contamination. The surface diffusion increases further for temperatures beyond the threshold temperature, thereby reducing the oxygen contamination further as discussed earlier. Since, the activation energy for surface diffusion is a function of growth flux [67], therefore the threshold temperature is different for the films of each deposition parameter combination.

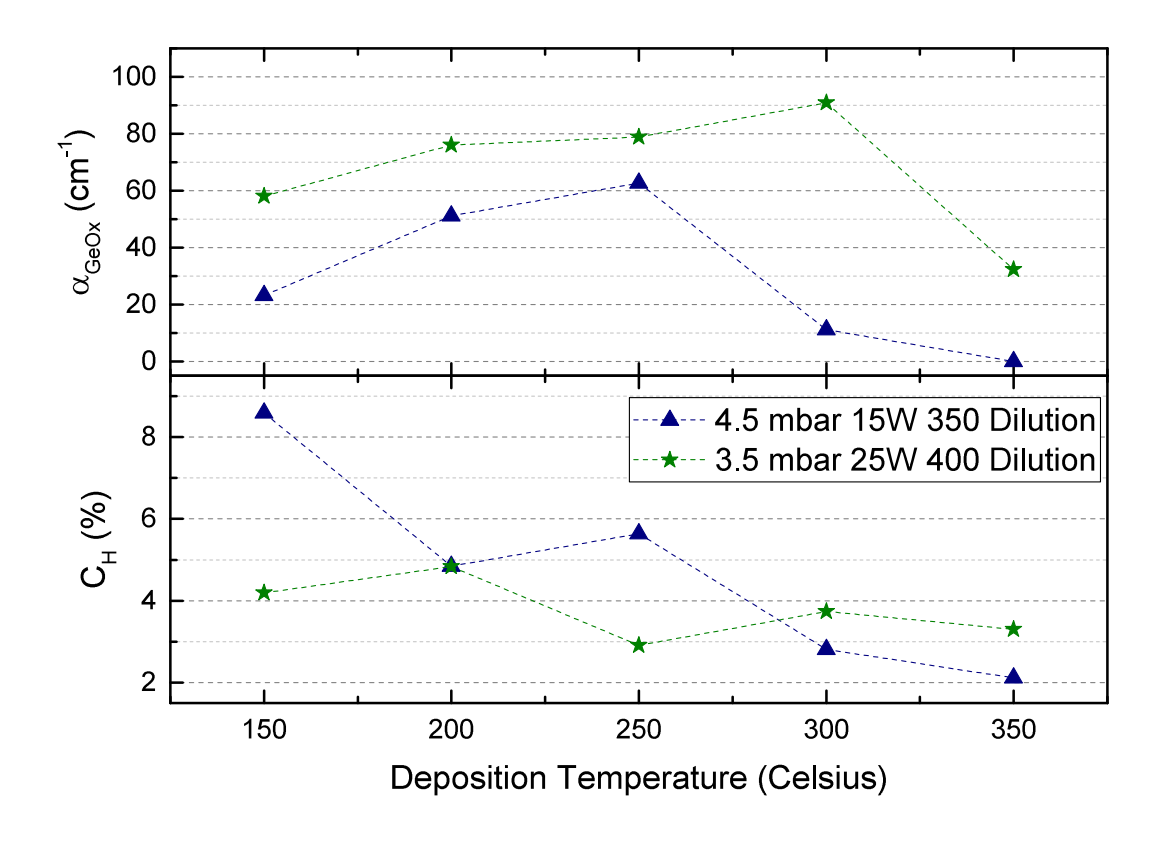


Figure 5.14: Effect of varying Deposition Temperature on the α_{GeO_X} & the hydrogen concentration (C_H)

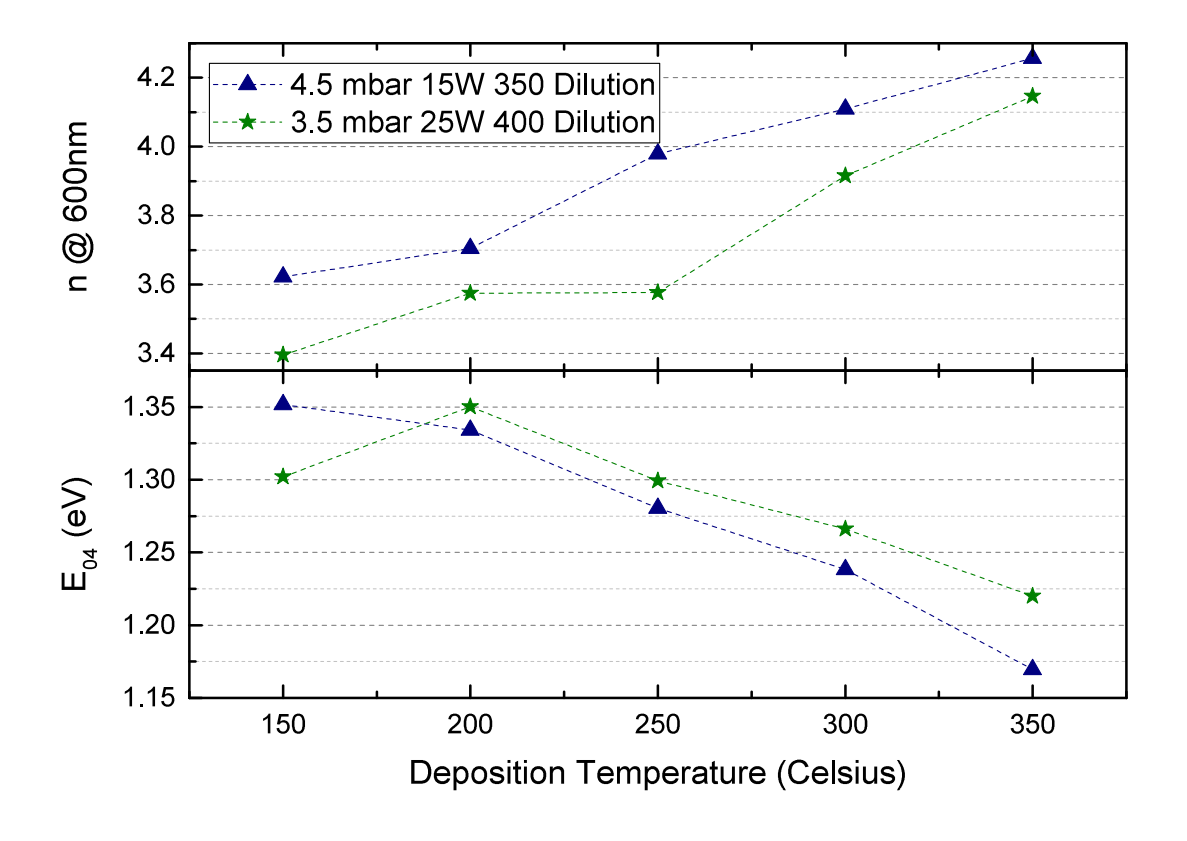


Figure 5.15: Effect of varying Deposition Temperature on the n @ 600nm & the $\rm E_{04}$ optical bandgap

The E_{04} optical bandgap as a function of deposition temperature is depicted in Figure 5.15 as well. It can be observed that for both the series of films, it tends to decrease with increasing deposition temperature. The decrease of the E_{04} optical bandgap is more pronounced in the lower dilution films (4.5 mbar-15 W) than the other films (3.5 mbar-25 W) with comparatively higher dilution. It is interesting to note that this also coincides with the increase of the refractive index at a wavelength of 600nm discussed earlier. Therefore, the decreasing E_{04} optical bandgap along with the increasing refractive index have a linear dependence on the hydrogen concentration (C_H) which is line with the literature paper by Nakashita et. al. [54]. A similar overall trend can also be observed in the E_{03} optical bandgap as a function of deposition temperature. This is depicted in Figure A.7.

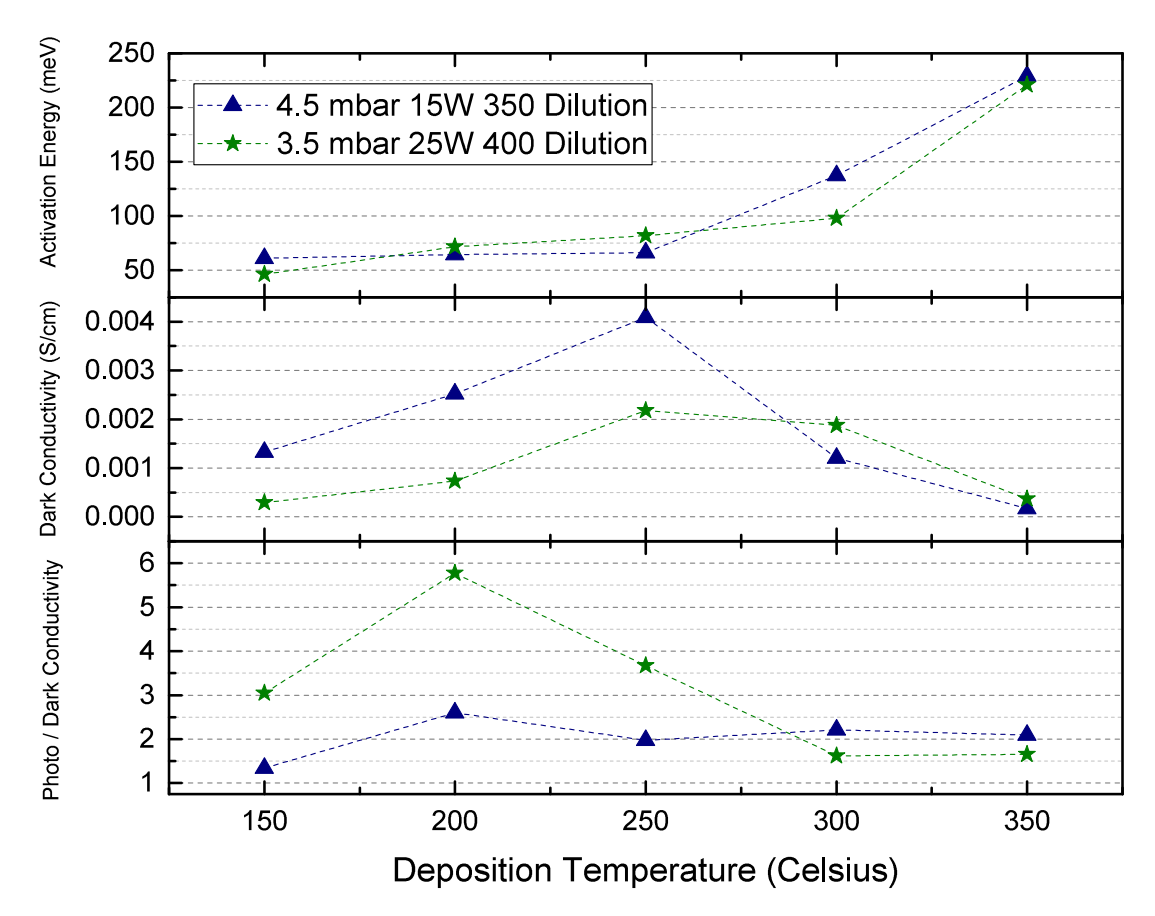


Figure 5.16: Effect of varying Deposition Temperature on the Activation Energy (E_{act}), Dark conductivity & the Photo/Dark Conductivity ratio

The dark conductivity as a function of deposition temperature is depicted in Figure 5.16. It can be observed that the dark conductivity increases until the deposition temperature reaches a certain threshold value (which varies for each of the two pressure-power combinations) and then begins to decrease. This can be linked to the fact that at the lower temperature region ($\leq 250^{\circ}$ C for 4.5 mbar-15 W & $\leq 300^{\circ}$ C for 3.5 mbar-25 W), the films deposited show increasing oxygen contamination as compared to those films deposited at the higher temperature region ($\geq 250^{\circ}$ C for 4.5 mbar-15 W & $\geq 300^{\circ}$ C for 3.5 mbar-25 W). This can also be verified by the results of the activation energy (\leq_{act}) which is also depicted in Figure 5.16. As discussed in previous sections, the classification of the oxidized films to be more n-type than the non-oxidized films holds true based on the results of the activation energy verified by previous literature works [65],[66]. Additionally, it is interesting to note that the effect of oxygen contamination on the σ_{o} is not as significant as was observed in previous sections. The trend in the photo/dark conductivity ratio is depicted in Figure 5.16 as well. It is interesting to note that for the lower dilution films (4.5 mbar-15 W), the photo/dark conductivity remains relatively constant. However, for the higher dilution films (3.5 mbar-25 W), the higher values of photo/dark conductivity could be associated to the oxygen contamination along with low dark conductivity value until the threshold

temperature is reached. Beyond the threshold temperature, it drops to significantly lower values due to reduced oxygen contamination.

The Raman Spectroscopy results of both the films (4.5 mbar-15 W-350 Dilution & 3.5 mbar-25 W-400 Dilution) at different deposition temperature is depicted in Figure 5.17. The crystalline fraction as a function of varying deposition temperature is depicted in Figure 5.18. It is calculated using the Equation 2.15 from the Raman Spectroscopy results.

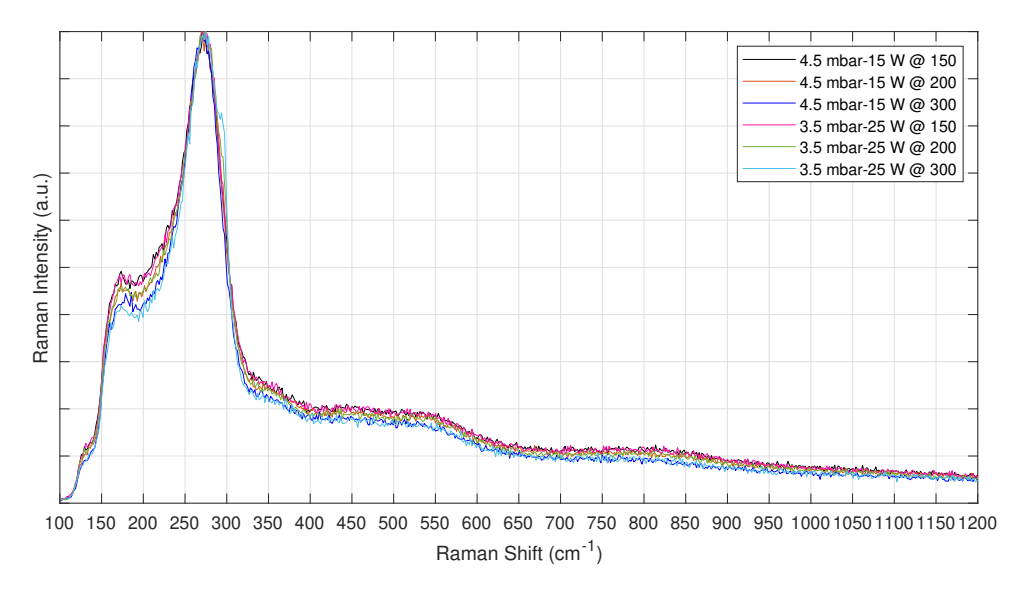


Figure 5.17: Effect of varying Deposition Temperature on the Raman Spectroscopy results

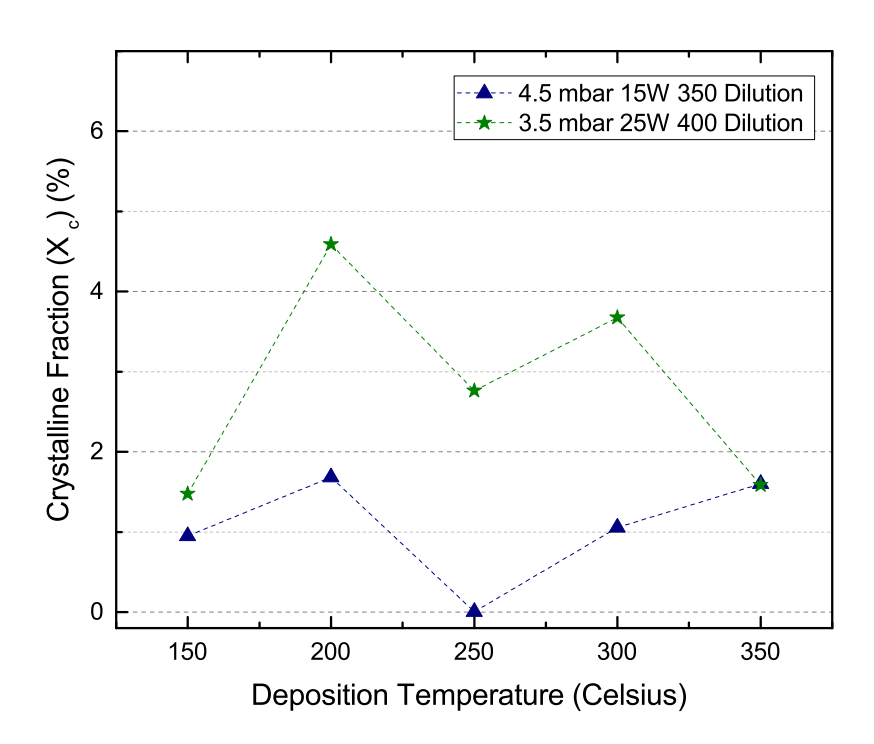


Figure 5.18: Crystalline Fraction (X_c) vs Deposition Temperature

In Figure 5.17, with the variation in the deposition temperature, the amorphous nature of the material for the 4.5 mbar-15 W films remains unchanged. This can be visualised by the peaks at 177 cm⁻¹ and 278 cm⁻¹ that denote the Longitudinal Acoustic and Transverse Optic phonon mode of a-Ge respectively as per Table 3.1. Similarly, the 3.5 mbar-25 W films also depict amorphous nature which does not vary with varying deposition temperature. However, in the previous section, the latter showed nano-crystalline behaviour that were observed by the peak at around 300 cm⁻¹ for a deposition temperature of 200°C in the Raman spectrum. This change from nc-Ge to a-Ge could possibly be due to the change in the chamber conditions. From Figure 5.18, it can be observed that both these films contain very low crystalline fraction which does not vary much with the variation in deposition temperature.

5.4. Effect of Hydrogen Post Treatment (HPT)

The literature paper by Karg et. al. [69], suggests that a post-deposition process such as the Hydrogen Post Treatment (HPT) reduced the defect density for films with quite low thicknesses (< 200nm). From the results obtained in the previous sections, a few films were specifically selected to study the effect of Hydrogen Post Treatment (HPT) on the film properties. An a-Ge film with no oxidation, mild oxidation and substantial oxidation along with a nc-Ge film were chosen for this purpose. Each of these films were subjected to a No HPT, Short HPT and a Long HPT conditions after their respective depositions. The conditions of the HPT along with the general deposition conditions of these films are represented in Table 5.4.

Deposition Parameter	Value/Range	Units
Pressure-Power	2-20,3-20,4-20,4.5-15	mbar-W
H ₂ /GeH ₄ dilution ratio	200,350,400	-
HPT conditions	3-8-200	mbar-W-sccm
Deposition Temperature	200	°C
Electrode Distance	20	mm
Deposition Time	adjusted to obtain thickness of 150 nm	minutes
H ₂ flow rate	175,200	sccm
GeH ₄ flow rate	0.5,1	sccm

Table 5.4: Deposition and HPT parameters

The effect of different HPT duration on the E_{04} optical bandgap is shown in Figure 5.19. It can be inferred that the E_{0.4} optical bandgap does not show much difference. Although not conclusive, the E₀₄ optical bandgap shows a marginal decrease when subjected to a short HPT duration for most of the films. In Figure 5.19, the refractive index of the films at 600nm for different HPT duration is also depicted. The results/trend is not very conclusive similar to the results of the E_{04} optical bandgap. However, it can be seen that for most of the films (each with different deposition parameter combination), a short duration of HPT is beneficial in obtaining a slightly less porous film as observed by the increase in the refractive index. This could possibly be associated to passivation of the dangling bonds present in the films. When these films are subjected to longer HPT conditions, some of them also show a marginal decrease in the refractive index. A speculation can be made that this could possibly be due to the etching of the films by the atomic hydrogen at these long HPT duration. The Photo/Dark conductivity ratio with respect to the duration of HPT is depicted in Figure 5.20. It can be observed that the photo/dark conductivity ratio marginally increases for a couple of films (4.5 mbar-15 W-200 Dilution & 3 mbar-20 W-350 Dilution) when subjected to a short duration of HPT and subsequently decrease as the films are subjected to longer HPT duration. The oxygen contamination in the films can be characterized by the absorption coefficient of GeO_x from the fitted FTIR spectrum and it is also depicted in Figure 5.20. It in interseting to observe that a couple of films (4.5 mbar-15 W-200 Dilution & 2 mbar-20 W-400 Dilution) that previously show oxidation, do not show oxidation anymore when subjected to a short duration of HPT. Since the value of α_{GeO_x} in these films is quite low in comparison to those in films discussed in previous sections, it can be possibly be associated to surface oxidation taking place in these films. The dark conductivity and the oxygen contamination results as a function of HPT duration, although not conclusive, seem to be promising for some of the films.

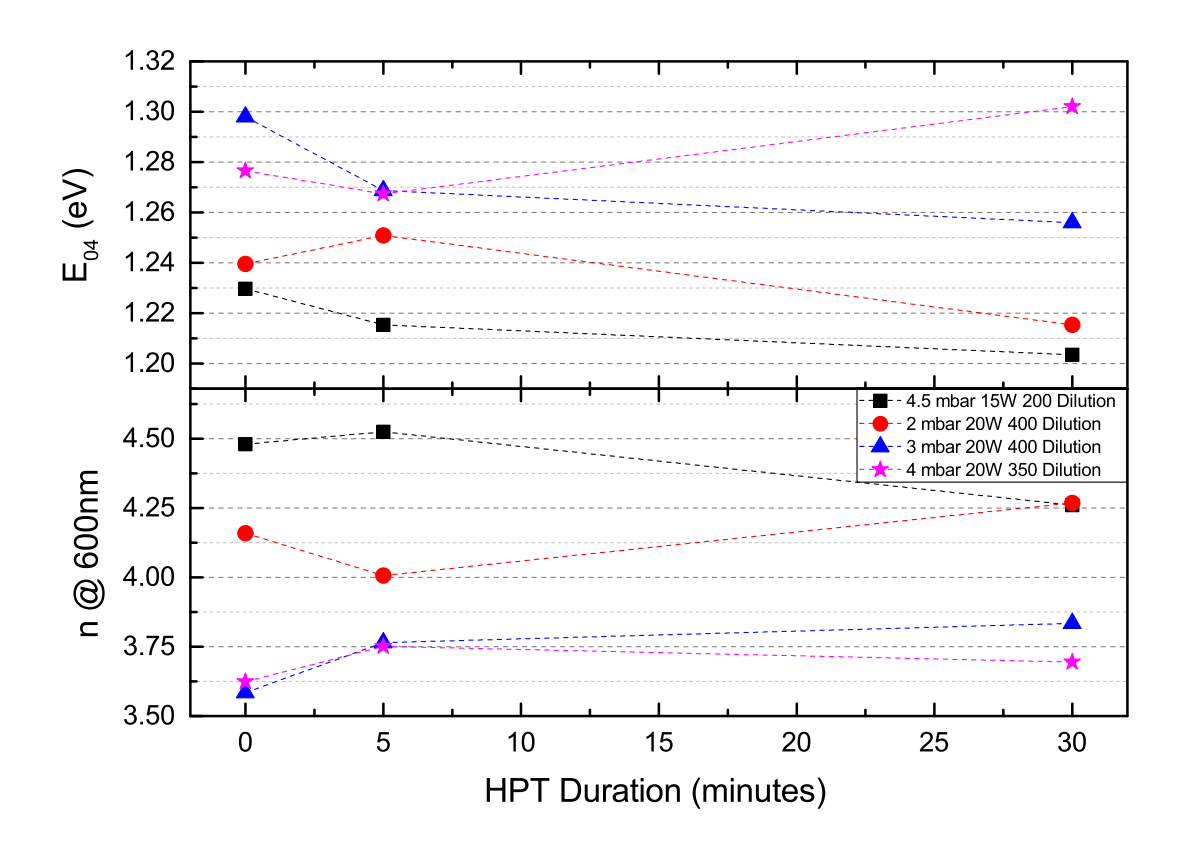


Figure 5.19: Effect of varying HPT duration on the $\rm E_{04}$ bandgap & n @ 600nm

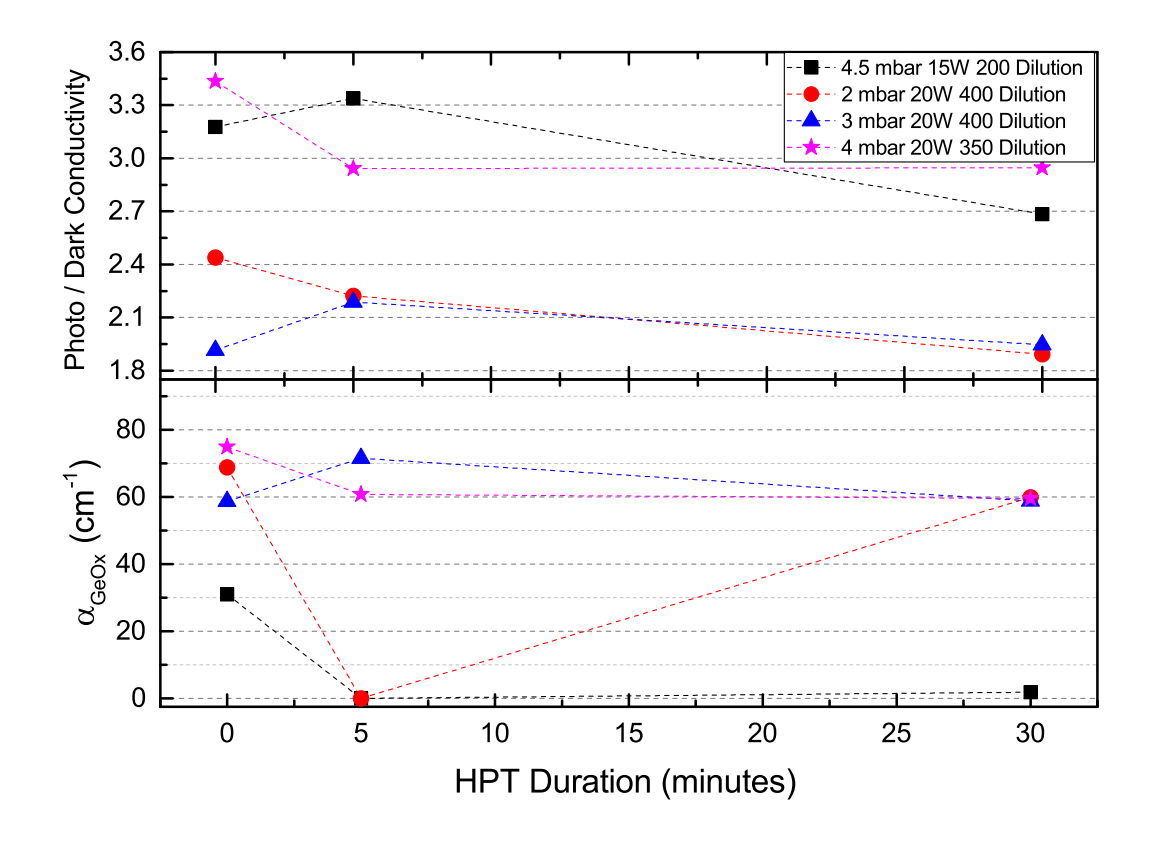


Figure 5.20: Effect of varying HPT duration on the Photo/Dark Conductivity ratio & α_{GeO_x}

5.5. Photo-thermal Deflection Spectroscopy and Ellipsometry results - Comparison and Analysis

The bandgaps obtained from the Spectroscopy Ellipsometry device are the Tauc bandgap (E_{TAUC}) and the E_{04} and E_{03} optical bandgaps. In the previous sections, the E_{04} and E_{03} optical bandgaps from the Ellipsometry results have been reported. They are considered more reliable due to the fact that these are absolute values unlike the Tauc bandgap (E_{TAUC}) which has an error margin based on the approximations made with regards to the thickness during the data-fitting procedure. Figure 5.21 depicts the relation between the Tauc bandgap (E_{TAUC}) and the E_{04} and E_{03} optical bandgaps obtained from Ellipsometry for all the films processed. It can be observed that the Tauc bandgap (E_{TAUC}) has a predominantly linear relation with optical bandgaps.

However, the E_{04} and E_{03} optical bandgaps can also be obtained from the Photo-thermal Deflection Spectroscopy measurements. The optical absorption determined by this technique are considered to be more accurate at near- and below- bandgap region of the films and hence these optical bandgaps are also considered to be more precise as discussed in section 3.4.5. In Figure 5.22, the absorption coefficient of certain films obtained from the Photo-thermal Deflection Spectroscopy technique as a function of the photon energy is depicted. It can be seen that the films that show oxygen contamination tend to have lower absorption coefficient (α) and it is very much pronounced at higher levels of photon energies. From this result, the E_{04} and E_{03} optical bandgaps can also be obtained. This can aid in comparing it to the same parameters obtained through the Ellipsometry technique that has been reported throughout this work.

Table 5.5 shows the values of the E_{04} and E_{03} optical bandgaps (from Ellipsometry results) that has been reported in the previous sections with respect to the same obtained through the Photo-thermal Deflection Spectroscopy results.

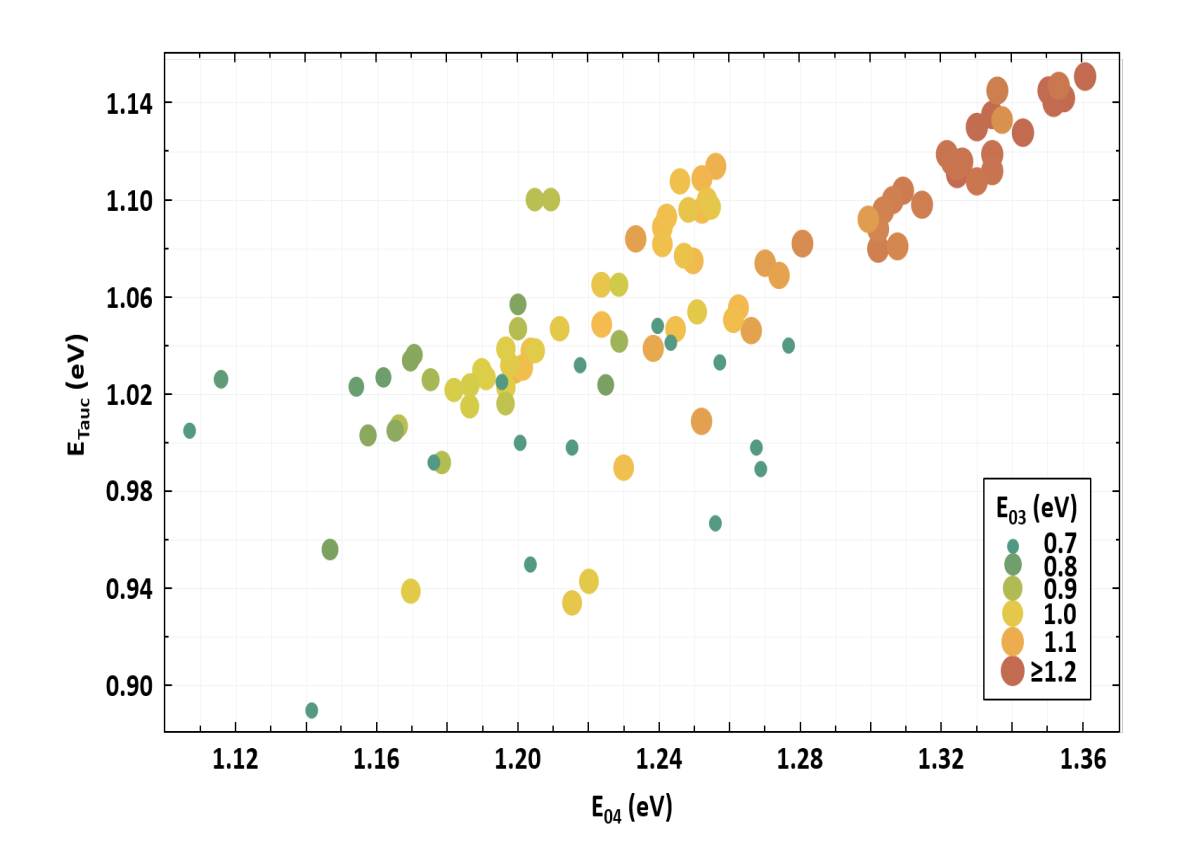


Figure 5.21: E_{TAUC} vs E_{04} and E_{03} (Ellipsometry results)

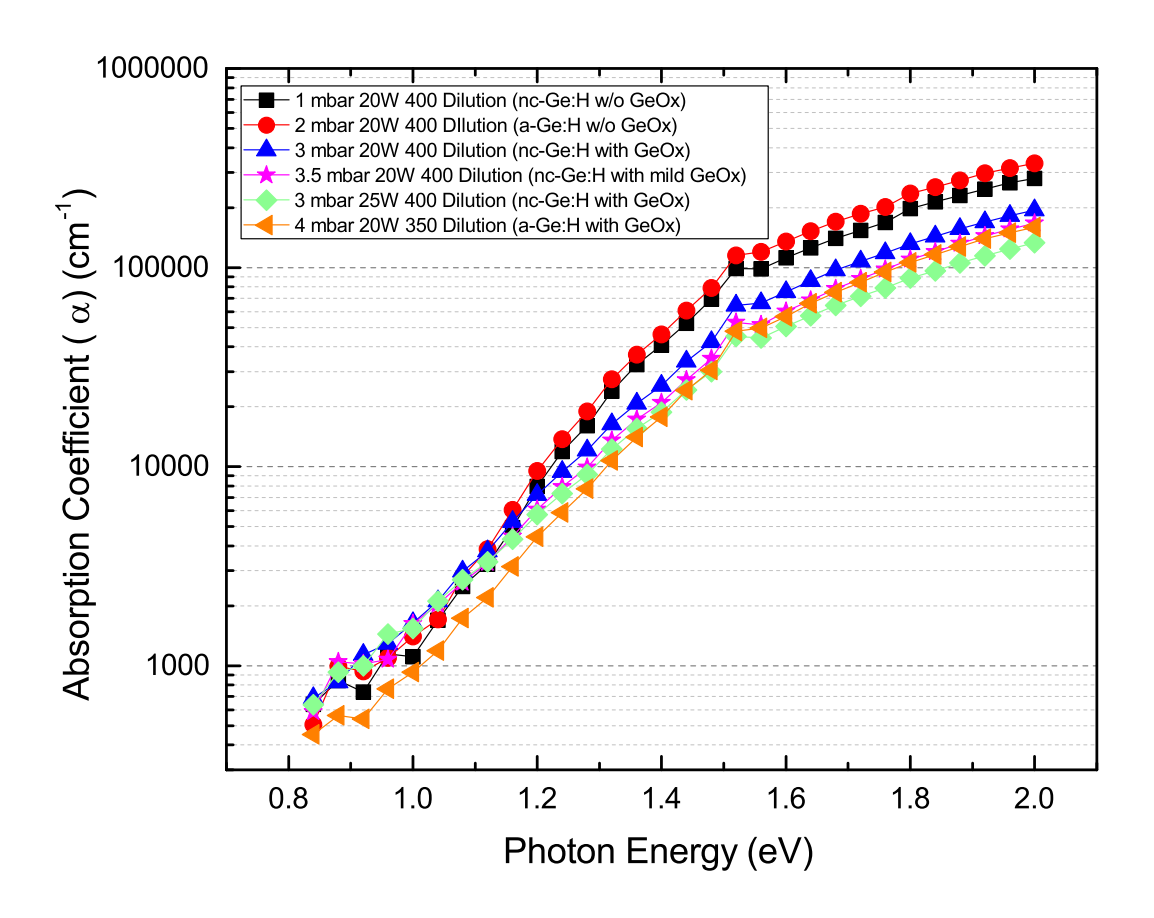


Figure 5.22: Absorption Coefficient (α) vs Photon Energy - from PDS results

Selected film	Optical Bandgaps	Ellipsometry results	PDS results
1 mbar 20W 400 Dilution	E ₀₄	1.254	1.221
1 mbai 2000 400 biludon	E ₀₃	1.000	0.945
2 mbar 20W 400 Dilution	E ₀₄	1.240	1.205
2 mbai 2000 400 Diludion	E ₀₃	1.055	0.938
3 mbar 20W 400 Dilution	E ₀₄	1.325	1.257
3 mbar 2000 400 Diludion	E ₀₃	1.187	0.910
3.5 mbar 20W 400 Dilution	E ₀₄	1.334	1.283
3.3 IIIbai 2000 400 Dilution	E ₀₃	1.187	0.880
3 mbar 25W 400 Dilution	E ₀₄ E ₀₃	1.338	1.290
3 mbar 25W 400 bilddon	E_{03}	1.149	0.920
4 mbar 20W 350 Dilution	E ₀₄	1.360	1.315
Tilibai 2000 330 bilution	E ₀₃	1.220	1.025

Table 5.5: E_{04} and E_{03} optical bandgaps comparison - Ellipsometry and PDS results

Thus, from the table above it can be seen that the ellipsometry results of the optical bandgaps that has been reported in this work are fairly similar to that obtained in the Photo-thermal Deflection spectroscopy results. Hence, it is a fairly good characterization of the optical bandgap of the films.

5.6. Overall Results and Trends

The GeH_4 precursor dissociates more easily than the commonly used SiH_4 precursor [69] [70] due to the fact that Ge as an element is much more heavier than Si, leading to a large flux of Ge radicals to the growing surface. Additionally, the Ge radicals formed during the deposition process also have a comparatively higher reactivity and hence lower mobility on the growing surface [71]. The results of these conditions is that it is difficult to avoid high deposition rates and porous growth of Ge with sufficient void density. Consequently, these void-rich films might easily undergo oxidation upon exposure to ambient. The oxygen contamination in the films has a major influence on various parameters as discussed in the previous sections.

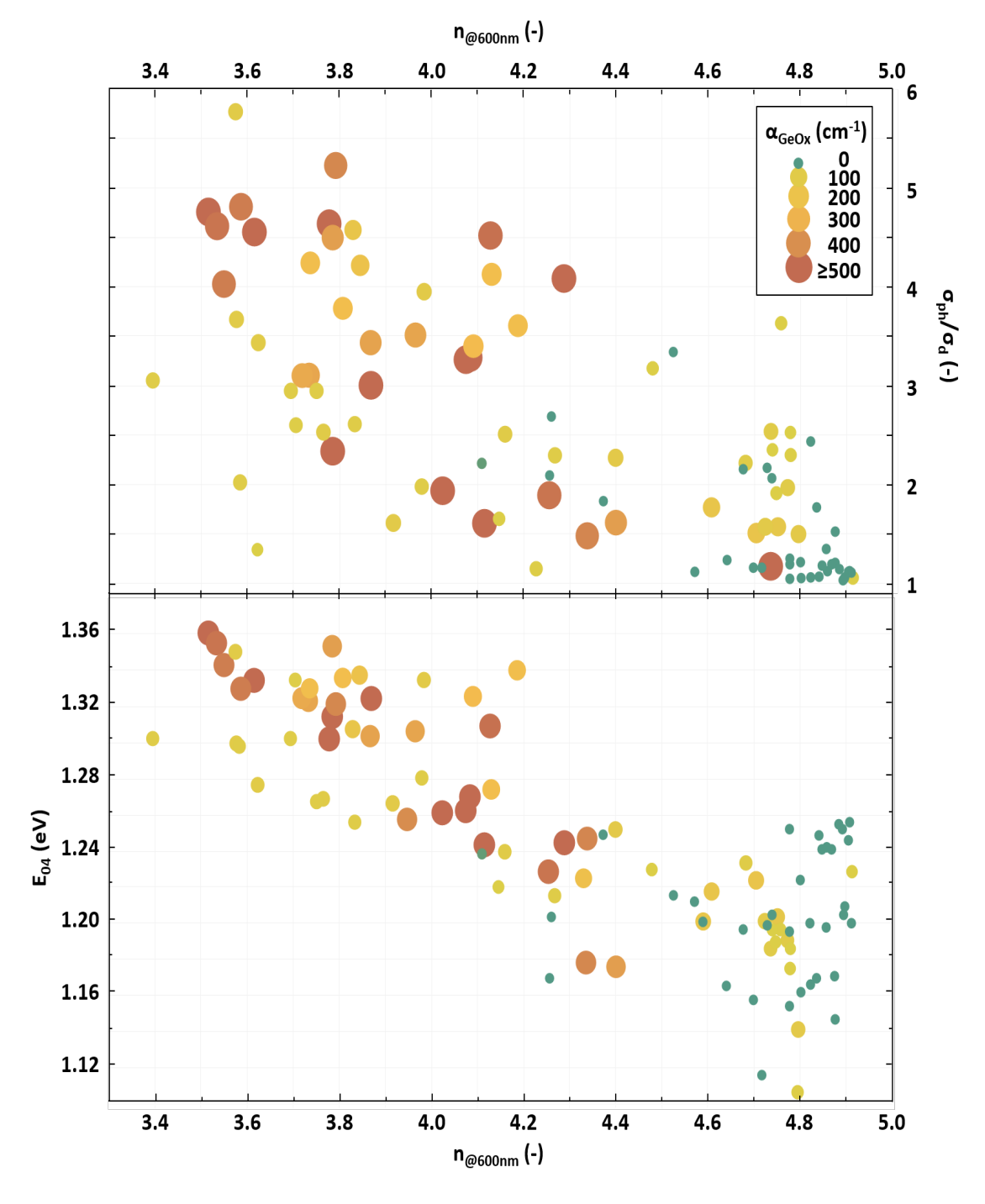


Figure 5.23: E_{04} & Photo/Dark conductivity vs n @ 600nm - as a function of α_{GeO_x}

Figure 5.23 depicts the relation of the absorption coefficient of GeO_x to the refractive index of the film and the associated E_{04} optical bandgap for all the films deposited as a part of this work. It can be observed that less porous/denser films having a high refractive index show lower oxygen contamination along with lower E_{04} optical bandgap. Similarly, the films that are comparatively more porous easily get contaminated by oxygen and they also show larger E_{04} optical bandgap. This trend can possibly be explained with the reasoning that the increase in the porous nature of the films is synonymous to the presence of more voids. Furthermore, if the defects at these voids are energetically well aligned with the reaction potential of the GeO_x bonds, then the increase in the voids could result in the increase in oxygen contamination. This would mean that with increasing void density and the decrease in the refractive index, the oxygen contamination would continuously increase. However, the oxygen contamination as a function of n @ 600nm is near discrete. Therefore, it is likely that the species responsible for oxidation is unable to diffuse into Ge:H if it is dense. The average Ge-Ge bond length in a fairly dense a-Ge:H is around 2.46 $^{\circ}$ [72], while that of an H₂O molecule is around 2.75 $^{\circ}$ [73]. So the water vapour from the ambient would be unable to penetrate. However, if enough Ge atoms are missing in the lattice of the a-Ge:H, i.e. with sufficient void density, then they would diffuse into the film and cause oxygen contamination in the bulk. the increase in oxygen contamination has led to decrease in the refractive index and this has been reported in literature [65]. Hence, the non-linear relation between the refractive index (n @ 600nm) and the α_{GeO_x} is a possibility of porosity-induced oxygen contamination and vice-versa.

Similarly, the oxygen contamination of the films also has a complex relationship with the photo/dark conductivity ratio. Figure 5.23 also depicts the relation between the absorption coefficient of the GeO_x bonds to the refractive index and the associated photo/dark conductivity ratio for all the films processed in this work. To explain this trend we look into the effect of the oxygen contamination on the dark conductivity with respect to other electrical parameters such as activation energy (E_{act}), preexponential factor (σ_o), photo-conductivity & photo/dark conductivity depicted in Figure 5.24. As seen in sections 5.1 and 5.2, the effect of oxygen contamination on the dark conductivity is more significant than that on the activation energy. This can be possibly associated to the significant decrease in the σ_o (about 1-5 orders of magnitude) upon oxidation causing a greater impact on the dark conductivity than the decrease in the activation energy. This also seems to suggest that the oxygen contamination may be able to passivate the dangling bonds effectively, which might possibly reduce the defect density and consequently the σ_o & dark conductivity. Additionally, some of the oxygen contaminated films also show a lower photo-conductivity than the films without any oxygen contamination. Therefore, it is conclusive that for most of the films reported in this work, the relatively high photo/dark conductivity shown by the films with oxygen contamination is related to the decrease in dark conductivity rather than the effect of the photo-conductivity.

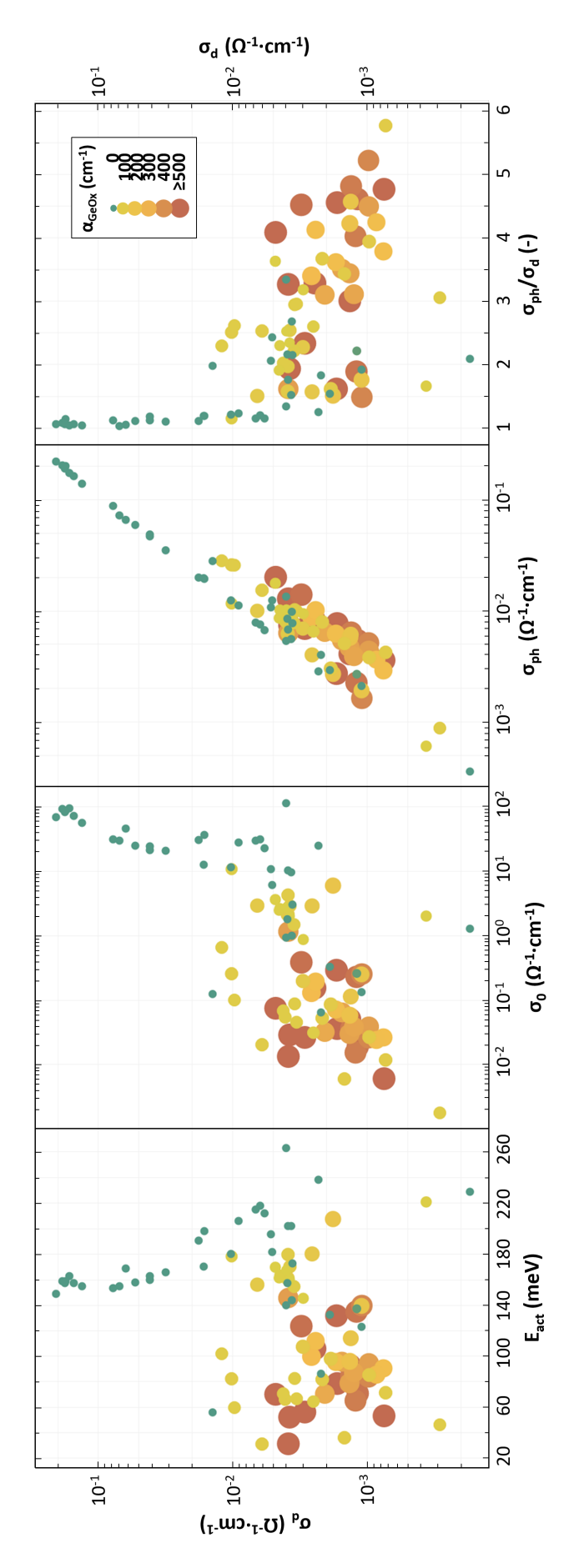


Figure 5.24: Dark Conductivity (σ_d) vs E $_{act}$, σ_o , σ_{ph} & photo/dark conductivity ratio - as a function of α_{GeO_x}

Single Junction Solar Cell

This chapter focuses on the performance of various single junction cells processed by using some of the individual Ge:H films discussed in the previous chapter. In section 6.1, the J-V characteristics of a p-n configuration with the Ge:H film acting as an n-type absorber is discussed. In section 6.2, the J-V characteristics of a p-i-n superstrate cell configuration with the Ge:H film acting as the i-type absorber, despite its n-type nature, is studied.

6.1. p-n configuration cells

The results obtained in section 5.4 were used to determine the deposition conditions for the Ge:H n-type absorber. Film A (4 mbar-20 W-350 Dilution-NO HPT) showing a-Ge:H nature and Film B (3 mbar-20 W-400 Dilution-Short HPT) that showed nc-Ge:H nature with relatively significant photo/dark conductivity ratios were chosen for this purpose. Table 6.1 represents the deposition parameters that were involved in the deposition of the n-layer.

Deposition Parameter	Value/Range	Units
Film A deposition conditions	4-20-350	mbar-W
Film B deposition conditions	3-20-400	mbar-W
HPT conditions (Film B)	3-8-200	mbar-W-sccm
HPT duration (Film B)	10	minutes
Deposition Temperature	200	°C
Electrode Distance	20	mm
Deposition Time	adjusted for thicknesses of 50, 100 & 150 nm	minutes
H ₂ flow rate	175,200	sccm
GeH₄ flow rate	0.5	sccm

Table 6.1: Deposition and HPT parameters for the n-layer

The various stages in the processing of this p-n configuration device is depicted in the Figure 6.1. An Asahi VU glass substrate with Flourine-doped Tin Oxide (FTO) was used, to which 500nm Al front contacts were added through the metal evaporation device Provac. A 3-4 nm layer of AZO was added as a protective layer to avoid blackening of the FTO, along with the nc-Si p-layer deposited in the AMIGO RF-PECVD setup. Then the Ge:H n-type absorbers were processed in the CASCADE setup. Then 70nm Indium-doped Tin Oxide (ITO) was deposited as the back TCO layer. Furthermore, a combination of 300nm Ag, 80nm Cr & 800nm Al were used as the back contacts in this device. A post-deposition annealing step at 130°C was carried out for 30 minutes to ensure the proper adhesion of the contacts.

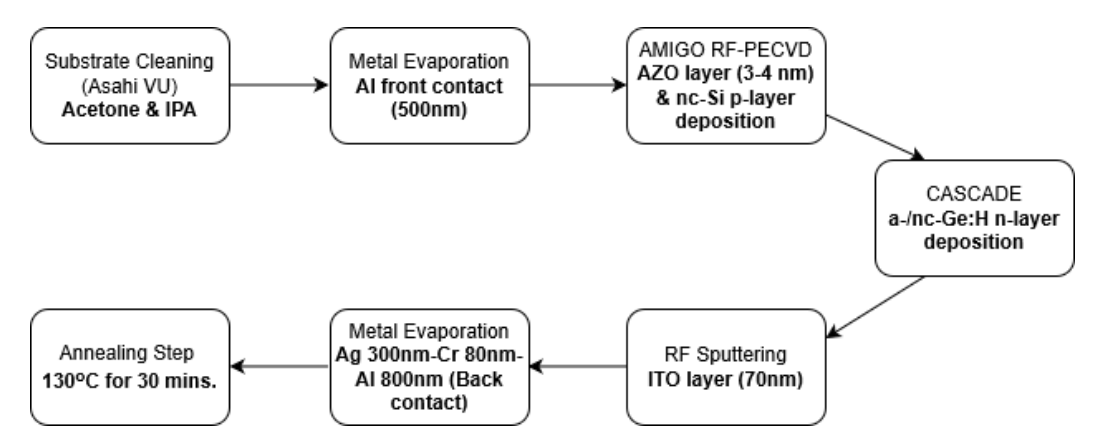


Figure 6.1: Various stages in the processing of the p-n configuration cells

In Figure 6.2, the J-V characteristics obtained from the measurements on the Wacom Solar Simulator are depicted as a function of n-layer thickness. It can be observed that the cells processed at high n-type absorber thicknesses (>50 nm), showed a resistor-like behaviour. While most of these cells failed, a couple of cells with absorber thickness of 50nm were the closest to resemble a cell-like behaviour. This suggests that there is a scope for improvement with regards to the processing of these cells. The above results can be verified by the results of the $R_{\rm S}$ and $R_{\rm Sh}$ explained in the next paragraph.

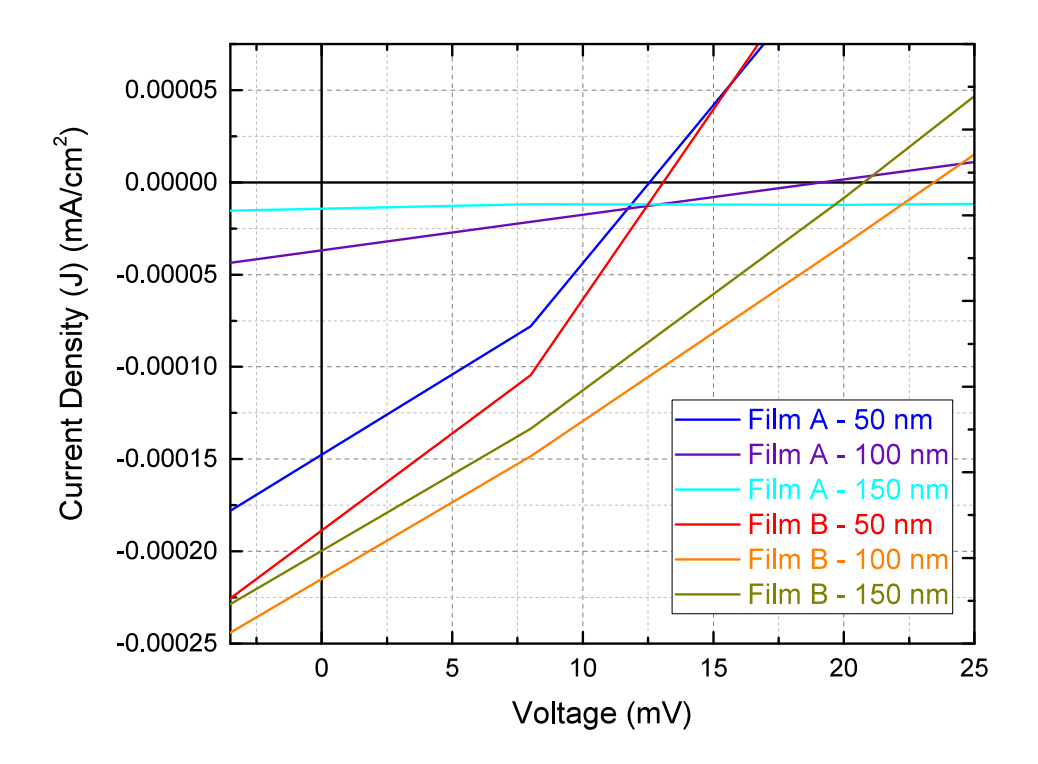


Figure 6.2: J-V characteristics as a function of n-layer thickness for Film A & Film B

The variation in R_s and R_{sh} as a function of n-type absorber thickness for both these absorbers is depicted in Figure 6.3. The significantly low values of the primary J-V parameters in the cells with film A as the n-type absorber layer can be attributed to the high R_s . The underlying cause of the significantly high R_s possibly causes a degradation of the I_{sc} as well apart from that in the fill factor (FF). The high I_{sc} can in turn be associated to the significant bulk resistance in the p-n junction. These cells also

show a high R_{sh} . Similarly, the cells with film B as the n-type absorber layer also show significantly low values of the primary J-V parameters. In contrast, these cells show comparatively lower R_s and R_{sh} . However, the values of the R_s is still quite high and hence significantly affect the I_{sc} and FF as well.

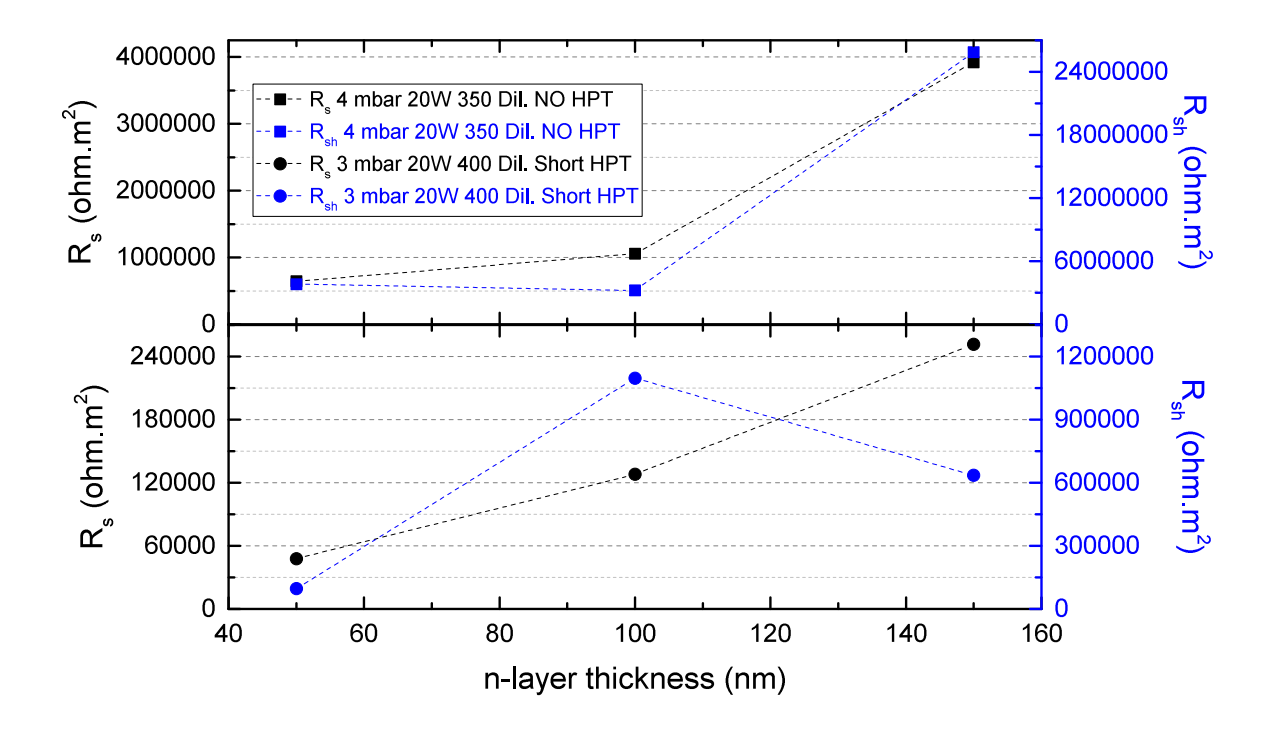


Figure 6.3: Series and Shunt resistances as a function of n-layer thickness for Film A (top); Film B (bottom)

The above results suggest that the device performance is being hampered. Ideally, a high R_{sh} is required and it can be obtained by increasing the thickness but there exists a trade-off as the R_s tends to increase as well when the layer becomes too thick. This is explained in the literature work on n-layer of CdS by H. Fujiwara et. al. [74] & also by K. Ariga et. al. [75]. A similar trend in the R_s and R_s with increasing thickness is observed in the cells reported in this section. Additionally, the losses associated to the R_{sh} become quite considerable if the material is quite defective/void-rich. This is in line with the porous nature of the n-type absorber layer which might possibly result in an defective material as reported in the previous chapter. Hence, this could be a possible hypothesis to the sub-optimal values of the R_s and the losses related to R_{sh} which in turn results in the resistor-like behaviour of most of these cells.

6.2. p-i-n superstrate configuration cells

As in the previous section, film B was also used as the i-layer, despite its n-type nature, in a p-i-n configuration device. However, only the cell with the 100nm absorber layer thickness was successfully processed while the others were accidentally damaged during the deposition of the cells. Most of the stages of processing mentioned in the previous section 6.1 were the same except for the fact that the chosen Ge:H was deposited to act as an intrinsic absorber layer. A separate n-layer of a-Si was deposited after the absorber layer to obtain the desired configuration. Therefore, the cell can be attributed to a more accurate p-n-n configuration. The J-V characteristics of this cell also fairly represented a resistor-like behaviour. The reason behind this is similar to that explained in the previous section.

7

Conclusions and Recommendations

The overall goal of the project is to find a device quality low-bandgap Ge:H absorber layer that can be used in the bottom cell of a multi-junction PV device. The first research objective of this thesis work was to study the influence of various deposition parameters on the various properties so as to obtain a set of Ge:H films that can be used as absorber layers. The other research objective was to use some of these absorber layers to form single-junction solar cells and subsequently analyze their performance.

Initially, the influence of various deposition parameters such as H_2/GeH_4 dilution ratio, deposition pressure, power, deposition temperature & a post-deposition HPT process on the Ge:H film properties were investigated. A processing window was found to be in the range of 1-5 mbar with the RF power ranging from 5-25 W with the electrode distance set at 20mm. nc-Ge:H films were processed in the range 20-25 W for deposition pressures of 2 mbar and higher.

A significant oxygen contamination was observed in most of the films. The presence and fraction of oxygen in these films was found to be related to the refractive index. The low refractive index (n @ 600nm) values highlights the porous nature of these films with significant void density. Hence, the films easily underwent oxidation through water vapour molecules when exposed to the ambient conditions. The oxygen contamination had a significant impact on the various properties of the films. The E_{04} optical bandgap was observed to increase upon oxygen contamination. Thereby, impeding the development of a low bandgap absorber layer to be used in the bottom cell of a multi-junction device. Additionally, the Activation Energy (E_{act}) was observed to decrease and generally there was a stronger decrease observed in the pre-exponential factor (σ_o) upon oxygen contamination. This meant that the decrease in the σ_o outweighed the decrease in the Activation Energy (E_{act}), thereby causing the dark conductivity to decrease drastically by 1-3 orders of magnitude in the oxidized films. This in turn resulted in higher photo/dark conductivities values in the oxidized films as compared to the un-oxidized ones. The underlying mechanism was believed to be the passivating effect of the oxygen thereby resulting in the decrease of Ge-dangling bond associated defect density in the films.

With regards to the un-oxidized films, the films deposited at 5 W at highest dilution ratio of 400 showed a linearly increasing photo/dark conductivity & decreasing E_{04} optical bandgap with increasing deposition pressure, which is quite promising. These films also showed a relatively high Activation Energy (around 200 meV) & a high refractive index with respect to increasing deposition pressure. Similarly, the films deposited at 4.5 mbar-15 W-200 dilution ratio with a short duration post-deposition HPT, tend to show relatively decent photo/dark conductivity ratios (around 3.4) along with a relatively good refractive index. They show a E_{04} optical bandgap around 1.2 eV and the lowest E_{TAUC} bandgap amongst un-oxidized films of around 0.93 eV.

Finally, p-n and p-i-n configuration cells were processed for specific films acting as the n-type absorber layer and intrinsic (i) absorber layer, respectively. The J-V characteristics for most of the cells showed resistor-like behaviour. The significantly high R_s values along with the losses associated to the R_{sh} degraded the critical cell parameters significantly. The losses associated to the resistances could

possibly be attributed to the void-rich nature of the films that is being used as the n-type/i- absorber layer. However, a couple of cells with low absorber layer thicknesses (50 nm) were close to resembling a cell-like behaviour based on their J-V characteristics & comparatively lower $R_{\rm s}$.

As a part of future research work, it would be interesting to observe the properties of these films deposited at varied electrode distances. Additionally, the effect of adding a material such as Sn (tin) to these films to make GeSn:H films could be intriguing. The effect of Sn on the optical & electrical properties of the films could provide an interesting insight into the growth mechanism. It would also be interesting to observe the extent of oxygen contamination in those films. Furthermore, single junction cells with an a-/nc-GeSn:H absorber layer can be processed and their performance can be analysed.

- [1] Enerdata, Electricity domestic consumption, (2019).
- [2] IEA, Global energy & co2 status report 2019, (2019).
- [3] U.S. Energy Information Administration, *Annual energy outlook*, (2020).
- [4] Atmospheric Composition Change the European Network of Excellence, *Climate change classes* 1, (2008).
- [5] A. H. M. Smets, M. Zeman, O. Isabella, R. van Swaaij, and K. Jager, *Solar energy: The physics and engineering of photovoltaic conversion, technologies and systems* (UIT, Cambridge, England, 2016).
- [6] T. de Vrijer, Stability and Performance of Doped Silicon Oxide Layers for Use in Thin Film Silicon Solar Cells, Master's thesis, Delft University of Technology (2015).
- [7] G. Yang, *High-efficient n-i-p thin-film silicon solar cells*, Ph.D. thesis, Delft University of Technology (2015).
- [8] S. J. Roerink, *Development of a-SiGe:H from material characterization to multi-junction device*, Master's thesis, Delft University of Technology (2019).
- [9] Wikipedia contributors, *Ellipsometry Wikipedia, the free encyclopedia,* (2020), [Online; accessed 30-March-2020].
- [10] Z. Remes, R. Vasudevan, K. Jarolimek, A. H. Smets, and M. Zeman, *The optical spectra of a-si:* H and a-sic: H thin films measured by the absolute photothermal deflection spectroscopy (pds), in Solid State Phenomena, Vol. 213 (Trans Tech Publ, 2014) pp. 19–28.
- [11] Ossila Ltd., Solar cells: A guide to theory and measurement, (2020).
- [12] M. Höök and X. Tang, Depletion of fossil fuels and anthropogenic climate change—a review, Energy Policy **52**, 797 (2013), special Section: Transition Pathways to a Low Carbon Economy.
- [13] S. Shafiee and E. Topal, When will fossil fuel reserves be diminished? Energy Policy **37**, 181 (2009).
- [14] EPA, Sources of greenhouse gas emissions, (2019).
- [15] K. Branker, M. Pathak, and J. Pearce, *A review of solar photovoltaic levelized cost of electricity,* Renewable and Sustainable Energy Reviews **15**, 4470 (2011).
- [16] The Editors of Encyclopedia Britannica, *Photovoltaic effect*, (2008).
- [17] W. Shockley and H. J. Queisser, *Detailed Balance Limit of Efficiency of p-n Junction Solar Cells*, Journal of Applied Physics **32**, 510 (1961).
- [18] A. Richter, M. Hermle, and S. W. Glunz, *Reassessment of the limiting efficiency for crystalline silicon solar cells*, IEEE Journal of Photovoltaics **3**, 1184 (2013).
- [19] Wikipedia contributors, *Snell's law Wikipedia, the free encyclopedia,* (2020), [Online; accessed 27-March-2020].
- [20] Wikipedia contributors, *Fresnel equations Wikipedia, the free encyclopedia,* (2020), [Online; accessed 27-March-2020].

[21] Wikipedia contributors, *Beer–lambert law — Wikipedia, the free encyclopedia,* (2020), [Online; accessed 27-March-2020].

- [22] M. de Grunt, IRFR Manual, PVMD Group, Delft University of Technology (2013).
- [23] G. E. Jellison and F. A. Modine, Parameterization of the optical functions of amorphous materials in the interband region, Applied Physics Letters 69, 371 (1996), https://doi.org/10.1063/1.118064
- [24] R. K. Kothandaraman, *Development of four-terminal devices utilising thin-film solar cells*, Master's thesis, Delft University of Technology (2018).
- [25] C. Smit, Expanding thermal plasma deposition of microcrystalline silicon for solar cells, Ph.D. thesis, Department of Applied Physics (2005).
- [26] Elettrorava S.p.A., Pecvd deposition systems, (2020), [Online; accessed 27-March-2020].
- [27] D. M. Mattox, in *Handbook of Physical Vapor Deposition (PVD) Processing (Second Edition)* (William Andrew Publishing, Boston, 2010) second edition ed., pp. 735 746.
- [28] J. A. Woollam Co., Inc., *M-2000 specifications*, (2007), [Online; accessed 30-March-2020].
- [29] R. Vismara, Optical characterization of photovoltaic materials and structures for thin-film solar cells based on advanced texturization, Master's thesis, Delft University of Technology (2014).
- [30] D. Bermejo and M. Cardona, *Raman scattering in pure and hydrogenated amorphous germanium and silicon*, Journal of Non-Crystalline Solids **32**, 405 (1979), electronic Properties and Structure of Amorphous Solids.
- [31] Collaboration: Authors and Editors of the volumes III/17A-22A-41A1a, *Germanium (ge) raman phonon frequencies and wavenumbers*, Group IV Elements, IV-IV and III-V Compounds. Part a-Lattice Properties , 1 (2001).
- [32] V. Volodin, G. Krivyakin, G. Ivlev, S. Prokopyev, S. Gusakova, and A. Popov, *Crystallization of amorphous germanium films and multilayer a-ge/a-si structures upon exposure to nanosecond laser radiation*, Semiconductors **53**, 400 (2019).
- [33] Y.-P. Chou and S.-C. Lee, *Structural, optical, and electrical properties of hydrogenated amorphous silicon germanium alloys,* Journal of Applied Physics **83**, 4111 (1998), https://doi.org/10.1063/1.367229 .
- [34] Y. Maeda, Visible photoluminescence from nanocrystallite ge embedded in a glassy sio₂ matrix: Evidence in support of the quantum-confinement mechanism, Phys. Rev. B **51**, 1658 (1995).
- [35] V. Volodin, D. Marin, V. Sachkov, E. Gorokhov, H. Rinnert, and M. Vergnat, *Applying an improved phonon confinement model to the analysis of raman spectra of germanium nanocrystals,* Journal of Experimental and Theoretical Physics **118**, 65 (2014).
- [36] P. Klement, C. Feser, B. Hanke, K. v. Maydell, and C. Agert, *Correlation between optical emission spectroscopy of hydrogen/germane plasma and the raman crystallinity factor of germanium layers*, Applied Physics Letters **102**, 152109 (2013).
- [37] P. Alfaro-Calderón, M. Cruz-Irisson, and C. Wang-Chen, *Theory of raman scattering by phonons in germanium nanostructures,* Nanoscale Research Letters **3**, 55 (2008).
- [38] H. Jamali, R. Mozafarinia, and A. Eshaghi, Evaluation of chemical and structural properties of germanium-carbon coatings deposited by plasma enhanced chemical vapor deposition, Journal of Alloys and Compounds **646**, 360 (2015).
- [39] C. Jiang, J. Zhu, J. Han, Z. Jia, and X. Yin, Chemical bonding and optical properties of germanium—carbon alloy films prepared by magnetron co-sputtering as a function of substrate temperature, Journal of Non-Crystalline Solids **357**, 3952 (2011).

[40] J. Zhu, C. Jiang, J. Han, H. Yu, J. Wang, Z. Jia, and R. Chen, *Optical and electrical properties of nonstoichiometric a-ge1–xcx films prepared by magnetron co-sputtering*, Applied Surface Science **258**, 3877 (2012).

- [41] S. Park, J. D'Arcy-Gall, D. Gall, Y.-W. Kim, P. Desjardins, and J. Greene, *C lattice site distributions in metastable ge 1- y c y alloys grown on ge (001) by molecular-beam epitaxy,* Journal of applied physics **91**, 3644 (2002).
- [42] Brian C. Smith, Fundamentals of Fourier transform infrared spectroscopy (CRC press, 2011).
- [43] Thermo Nicolet Corporation, Introduction to fourier transform infrared spectrometry, (2001).
- [44] M. Wojdyr, Fityk: a general-purpose peak fitting program, Journal of Applied Crystallography 43, 1126 (2010).
- [45] M. S. Abo-Ghazala and S. A. Hazrny, *Hydrogen bonding in hydrogenated amorphous germanium*, Tsinghua Science and Technology **9**, 177 (2004).
- [46] M. Cardona, *Vibrational spectra of hydrogen in silicon and germanium*, physica status solidi (b) **118**, 463 (1983), https://onlinelibrary.wiley.com/doi/pdf/10.1002/pssb.2221180202 .
- [47] T. Matsumoto, Y. Murata, and J.-i. Watanabe, Study of silicon-hydrogen bonds at an amorphous silicon/silicon nitride interface using infrared attenuated total reflection spectroscopy, Applied physics letters **60**, 1942 (1992).
- [48] C. E. Viana, A. N. R. d. Silva, N. I. Morimoto, and O. Bonnaud, *Analysis of SiO2 Thin Films Deposited by PECVD Using an Oxygen-TEOS-Argon Mixture*, Brazilian Journal of Physics **31**, 299 (2001).
- [49] G. Lucovsky, S. Chao, J. Yang, J. Tyler, R. Ross, and W. Czubatyj, *Chemical bonding of hydrogen and oxygen in glow-discharge—deposited thin films of a-ge: H and a-ge:(h, o), Physical Review B* **31**, 2190 (1985).
- [50] W. Paul, *Structural, optical and photoelectronic properties of improved pecvd a-ge:h,* Journal of Non-Crystalline Solids **137-138**, 803 (1991).
- [51] I. Chambouleyron, F. C. Marques, J. P. de Souza, and I. J. R. Baumvol, *Structure and composition of amorphous ge1-xsnx thin films*, Journal of Applied Physics **63**, 5596 (1988), https://doi.org/10.1063/1.340338.
- [52] B. Najafov and V. Figarov, *Hydrogen content evaluation in hydrogenated nanocrystalline silicon and its amorphous alloys with germanium and carbon*, International Journal of Hydrogen Energy **35**, 4361 (2010).
- [53] C. Hu, L. Qiao, H. Tian, X. Lu, Q. Jiang, and W. Zheng, *Role of carbon in the formation of hard ge1–xcx thin films by reactive magnetron sputtering*, Physica B: Condensed Matter **406**, 2658 (2011).
- [54] T. Nakashita, A. Inoue, S. Hagiwara, F. Uehara, and K. Kohno, *Dependence of electronic properties of hydrogenated amorphous ge on deposition condition,* Japanese journal of applied physics **31**, 1730 (1992).
- [55] P. Kazimierski and L. Jóźwiak, *Transition from amorphous semiconductor to amorphous insulator in hydrogenated carbon–germanium films investigated by ir spectroscopy,* Journal of Non-Crystalline Solids **355**, 280 (2009).
- [56] M. Gazicki, R. Ledzion, R. Mazurczyk, and S. Pawłowski, *Deposition and properties of germanium/carbon films deposited from tetramethylgermanium in a parallel plate rf discharge,* Thin Solid Films **322**, 123 (1998).
- [57] M. Gazicki, *Plasma deposition of thin carbon/germanium alloy films from organogermanium compounds*, Chaos, Solitons & Fractals **10**, 1983 (1999).

[58] A. H. M. Smets, T. Matsui, and M. Kondo, High-rate deposition of microcrystalline silicon p-i-n solar cells in the high pressure depletion regime, Journal of Applied Physics 104, 034508 (2008), https://doi.org/10.1063/1.2961334.

- [59] A. Bronneberg, A. Smets, M. Creatore, and M. van de Sanden, On the oxidation mechanism of microcrystalline silicon thin films studied by fourier transform infrared spectroscopy, Journal of Non-Crystalline Solids 357, 884 (2011).
- [60] W. Lau, Infrared characterization for microelectronics (World scientific, 1999).
- [61] K. Eberhardt and G. Bauer, Effect of h-content and h-bonding configuration on light and thermal induced metastability in amorphous hydrogenated germanium (a-ge:h), Journal of Non-Crystalline Solids 164-166, 19 (1993), proceedings of the Fifteenth International Conference on Amorphous Semiconductors Science and Technology.
- [62] Y. Yashiki, S. Kouketsu, S. Miyajima, A. Yamada, and M. Konagai, *Growth and characterization of germanium carbon thin films deposited by vhf plasma cvd technique*, in 2006 IEEE 4th World Conference on Photovoltaic Energy Conference, Vol. 2 (2006) pp. 1608–1611.
- [63] J. Jiang, K. Chen, D. Feng, and D. Sun, *Structural evolution during the crystallization process of germanium films prepared by plasma enhanced chemical vapour deposition*, Thin Solid Films **230**, 7 (1993).
- [64] M. Stutzmann, J. Stuke, and H. Dersch, *Electron spin resonance of doped glow-discharge amorphous germanium*, physica status solidi (b) **115**, 141 (1983), https://onlinelibrary.wiley.com/doi/pdf/10.1002/pssb.2221150116.
- [65] B. Schröder, A. Annen, T. Drüsedau, H. Freistedt, P. Deák, and H. Oechsner, *Influence of oxygen incorporation on the properties of magnetron sputtered hydrogenated amorphous germanium films*, Applied Physics Letters **62**, 1961 (1993), https://doi.org/10.1063/1.109504.
- [66] M. Moreno, N. Delgadillo, A. Torres, R. Ambrosio, P. Rosales, A. Kosarev, C. Reyes-Betanzo, J. [de la Hidalga-Wade], C. Zuniga, and W. Calleja, *Boron doping compensation of hydrogenated amorphous and polymorphous germanium thin films for infrared detection applications*, Thin Solid Films **548**, 533 (2013).
- [67] A. H. M. Smets, W. M. M. Kessels, and M. C. M. van de Sanden, Surface-diffusion-controlled incorporation of nanosized voids during hydrogenated amorphous silicon film growth, Applied Physics Letters 86, 041909 (2005), https://doi.org/10.1063/1.1853508.
- [68] A. Smets, W. Kessels, and M. Van De Sanden, *The effect of ion-surface and ion-bulk interactions during hydrogenated amorphous silicon deposition,* Journal of Applied Physics **102**, 073523 (2007).
- [69] F. Karg, H. Böhm, and K. Pierz, *Influence of plasma deposition on structural and electronic properties of a-ge:h*, Journal of Non-Crystalline Solids **114**, 477 (1989), proceedings of the Thirteenth International Conference on Amorphous and Liquid Semiconductors.
- [70] Y. Shing, J. Perry, and C. Allevato, *Amorphous silicon germanium alloy film deposition with in situ plasma diagnostics*, Solar Cells **24**, 353 (1988).
- [71] A. Bhaduri, P. Chaudhuri, S. Vignoli, and C. Longeaud, *Correlation of structural inhomogeneities with transport properties in amorphous silicon germanium alloy thin films*, Solar Energy Materials and Solar Cells **94**, 1492 (2010), pVSEC 18.
- [72] T. Abtew and D. Drabold, *Ab initio models of amorphous si 1- x ge x: H,* Physical Review B **75**, 045201 (2007).
- [73] R. L. Redington and D. E. Milligan, Infrared spectroscopic evidence for the rotation of the water molecule in solid argon, The Journal of Chemical Physics 37, 2162 (1962), https://doi.org/10.1063/1.1732982.
- [74] H. Fujiwara and R. W. Collins, Spectroscopic Ellipsometry for Photovoltaics (Springer, 2018).
- [75] K. Ariga and M. Ebara, *Materials Nanoarchitectonics* (John Wiley & Sons, 2018).



Appendix A - Additional Results of film characteristics

A.1. Effect of varying H₂/GeH₄ dilution ratio

Figure A.1 depicts the $\rm E_{03}$ optical bandgap as a function of varying $\rm H_2/GeH_4$ dilution ratio.

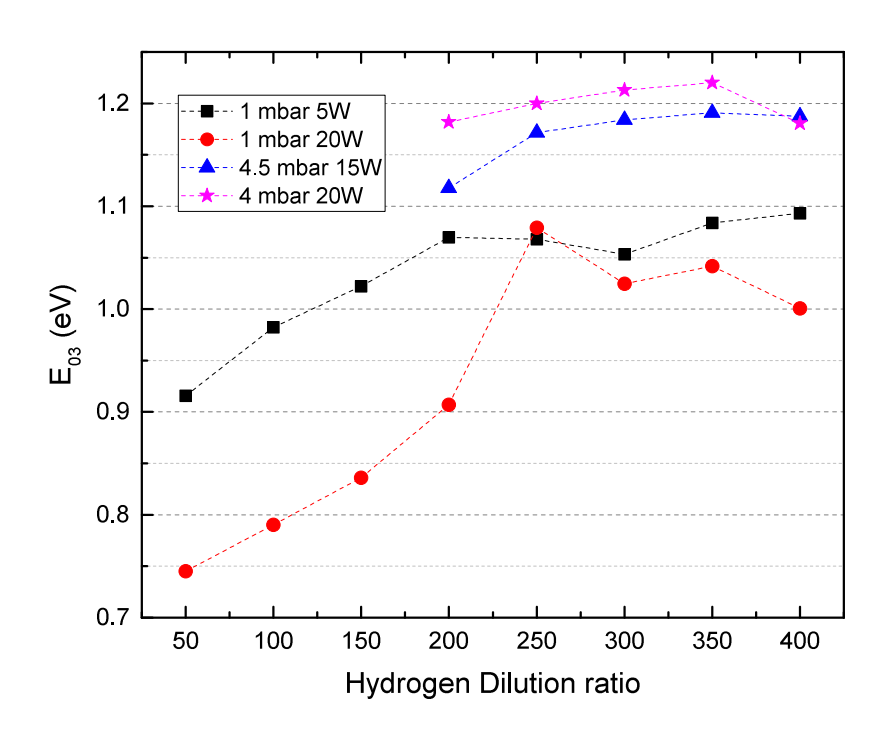


Figure A.1: E₀₃ optical bandgap vs H₂/GeH₄ dilution ratio

Figure A.2 depicts the Deposition rate as a function of varying H_2/GeH_4 dilution ratio.

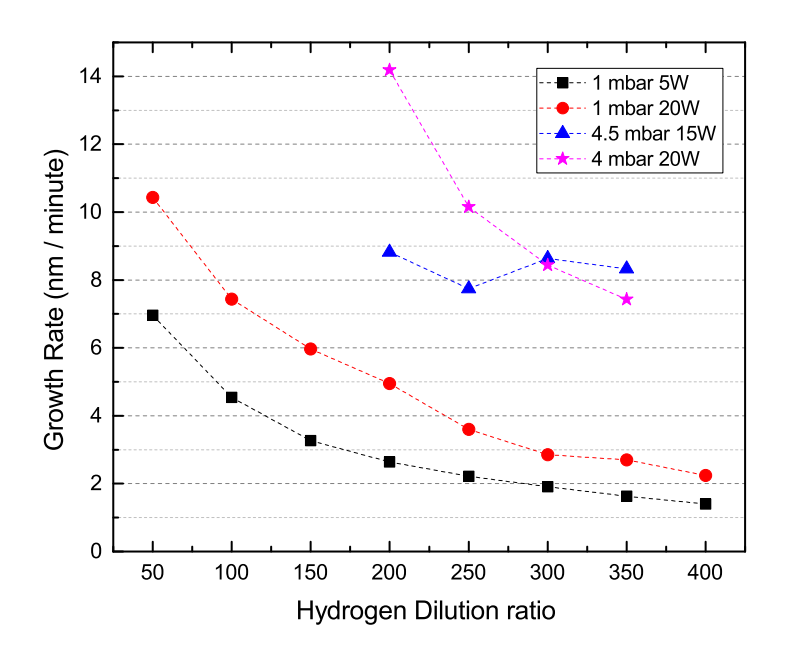


Figure A.2: Deposition rate vs H₂/GeH₄ dilution ratio

A.2. Effect of varying Pressure-Power

Figure A.3 depicts the fitted FTIR Spectrum for films as a function of varying pressure-power.

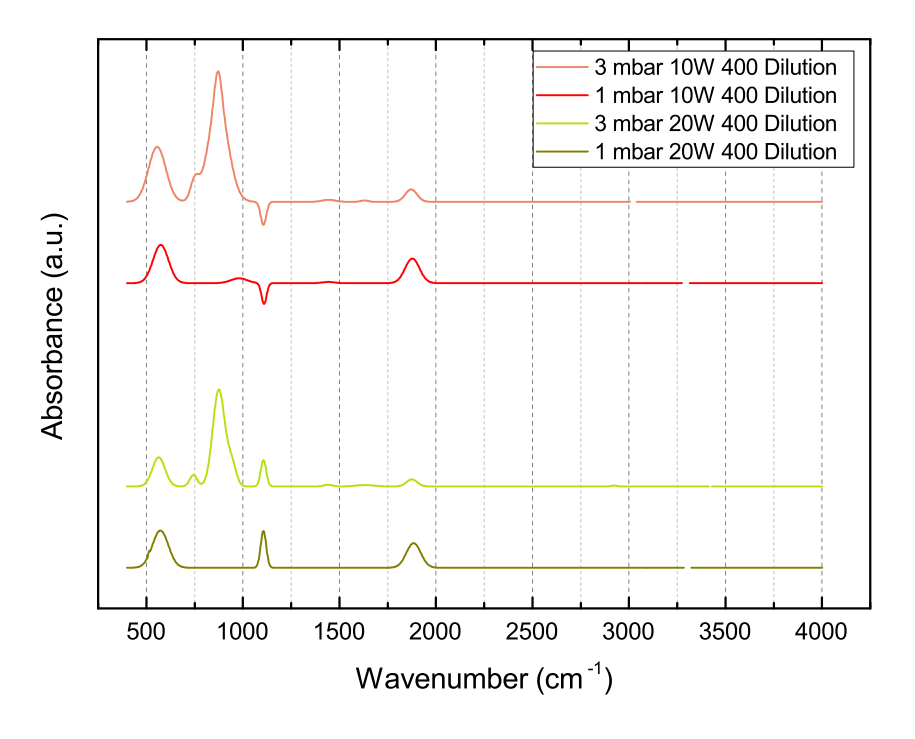


Figure A.3: Fitted FTIR Spectrum for films with varying pressure-power

Figure A.4 depicts the E_{03} optical bandgap as a function of varying Pressure-Power.

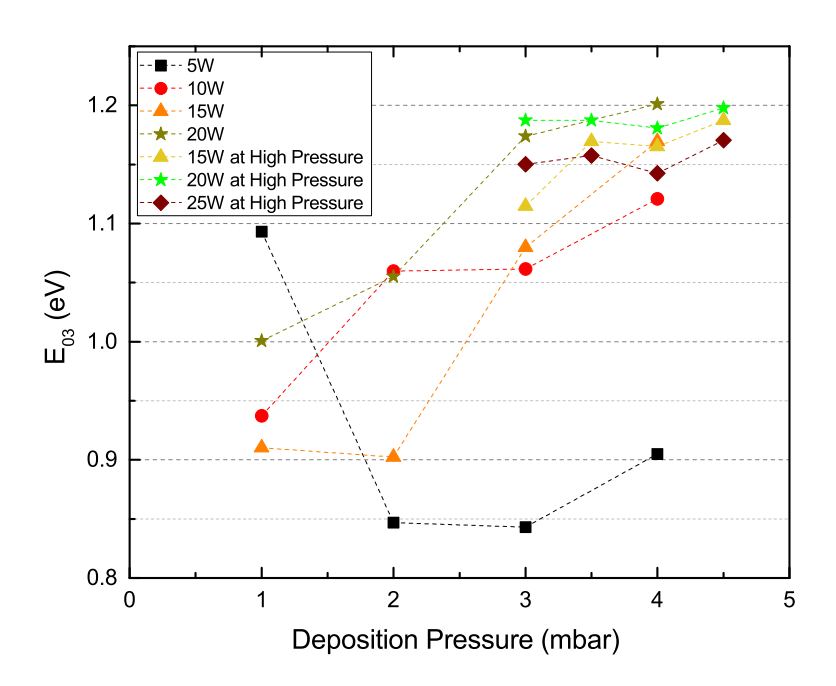


Figure A.4: E_{03} optical bandgap vs Pressure-Power

Figure A.5 depicts the Deposition rate as a function of varying Pressure-Power.

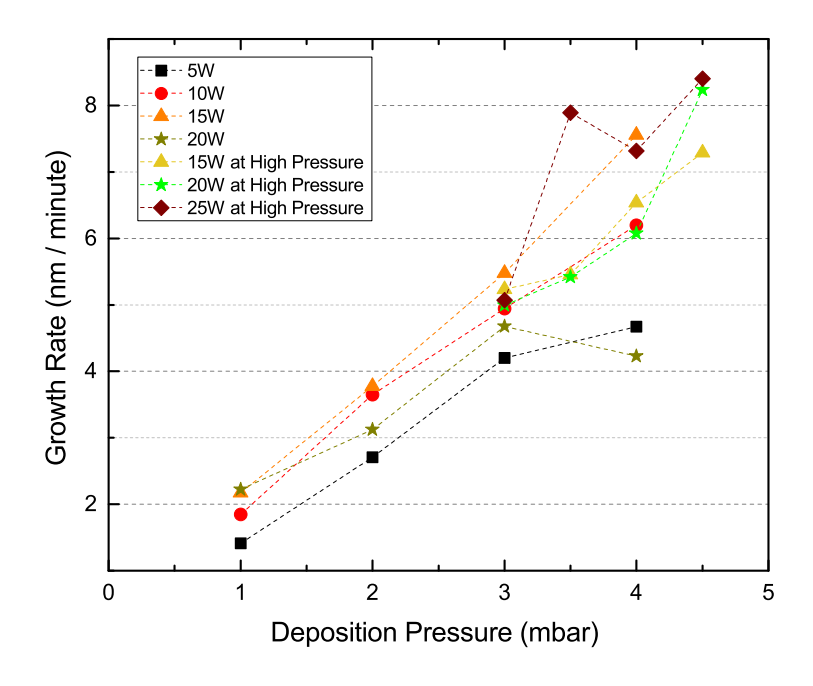


Figure A.5: Deposition rate vs Pressure-Power

A.3. Effect of varying Deposition Temperature

Figure A.6 depicts the fitted FTIR Spectrum for films as a function of varying deposition temperature.

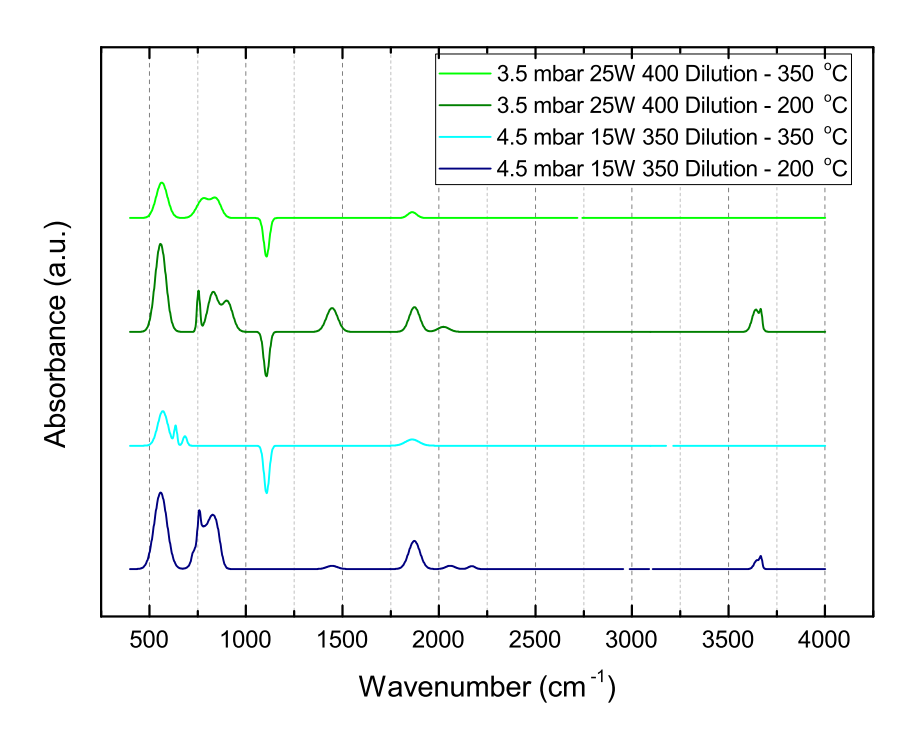


Figure A.6: Fitted FTIR Spectrum for film with varying Deposition Temperature

Figure A.7 depicts the E_{03} optical bandgap as a function of varying deposition temperature.

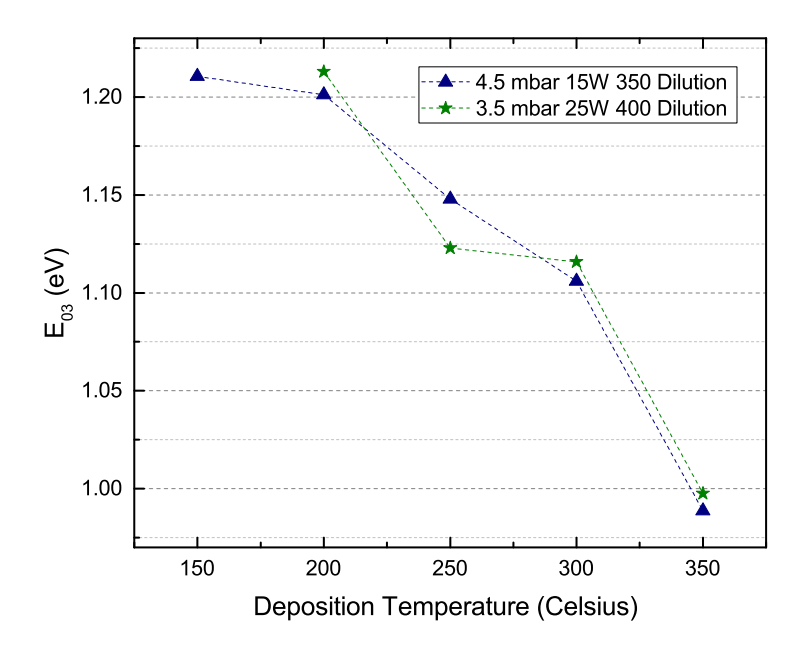


Figure A.7: E_{03} optical bandgap vs Deposition Temperature

Figure A.8 depicts the Deposition rate as a function of varying deposition temperature.

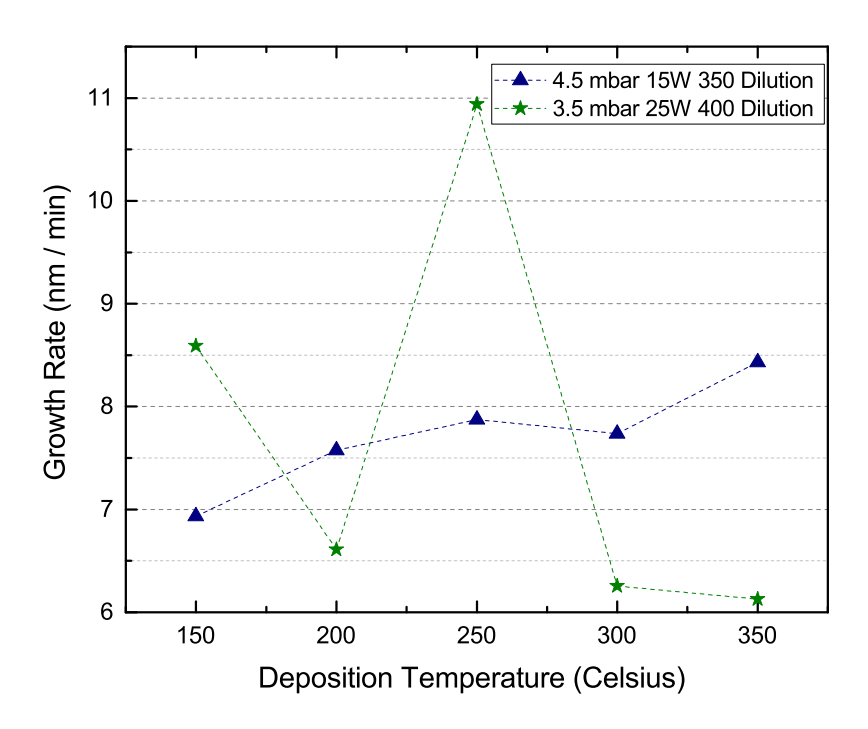


Figure A.8: Deposition rate vs Deposition Temperature